UNIVERSITY OF SOUTHAMPTON
FACULTY OF ENGINEERING, SCIENCE AND MATHEMATICS
SCHOOL OF PHYSICS AND ASTRONOMY

The relationship between the X-ray and optical variability in Seyfert galaxies

Elmé Breedt Lategan

Submitted for the degree of Doctor of Philosophy

August 2009

UNIVERSITY OF SOUTHAMPTON

ABSTRACT

FACULTY OF ENGINEERING, SCIENCE AND MATHEMATICS
SCHOOL OF PHYSICS AND ASTRONOMY
DOCTOR OF PHILOSOPHY

The relationship between the X-ray and optical variability in Seyfert galaxies
by Elmé Breedt Lategan

Seyfert galaxies have been known to vary since shortly after their discovery, but the origin of the optical variability and its relationship to the X-rays, have not been well established. Presented here is a comprehensive comparison between the long term X-ray and optical emission in a sample of seven Seyfert galaxies, to determine the relationship between the X-ray and optical variations. It is shown that the observed optical variability is the sum of several independent mechanisms: the short time-scale variability is dominated by X-ray reprocessing, but variations intrinsic to the disc, such as propagating accretion rate fluctuations, add considerable variability power on long time-scales.

Cross-correlation analysis reveal a statistically significant correlation between the X-ray and optical emission of all the galaxies under investigation, with the optical variations following the X-rays by 1–2 days. This time-scale is consistent with the expected light travel time from the central X-ray source to the optically emitting region of the accretion disc. Although this is a strong indicator of X-ray reprocessing by the disc, it is also clear that reprocessing cannot account for all the optical variations observed. At least one source displays clear long time-scale (years) variations in the optical with no apparent counterpart in the X-rays, and in others the long term optical amplitude exceed that of the X-rays. It is shown that these long time-scale optical variations must originate from an independent variability mechanism, possibly variations in the accretion rate or the geometry of the system. There is also evidence that there may be a significant contribution to the optical emission from as far out as the dust torus.

Finally it is shown that there may be a dependence of the strength of the X-ray/optical correlation on the disc temperature and black hole mass.

Contents

List of Figures

List of Tables

DECLARATION

I declare that this thesis, entitled *The relationship between the X-ray and optical variability in Seyfert galaxies*, is my own, and the work presented herein is the result of my own original research.

I confirm that:

> this work was done wholly between October 2005 and August 2009 while I was in candidature for a research degree at the University of Southampton;
>
> no part of this thesis has previously been submitted for a degree or any other qualification at this University or any other institution;
>
> where I have consulted the published work of others, this is always clearly attributed;
>
> where I have quoted from the work of others, the source is always given. With the exception of such quotations, this thesis is entirely my own work;
>
> I have acknowledged all main sources of help; and
>
> where the thesis is based on work done by myself jointly with others, I have made clear exactly what was done by others and what I have contributed myself.

Chapter 3 of this thesis has been published as:

> Breedt, E.; Arévalo, P.; M^{c}Hardy, I. M.; Uttley, P.; Sergeev, S. G.; Minezaki, T.; Yoshii, Y.; Gaskell, C. M.; Cackett, E. M.; Horne, K. and Koshida, S., 2009, *MNRAS*, 394, 427

and Chapter 4 has been accepted for publication in *MNRAS*:

> Breedt, E.; M^{c}Hardy, I,M.; Arévalo, P.; Uttley, P.; Sergeev, S. G.; Minezaki, T.; Yoshii, Y.; Sakata, Y.; Lira, P.; Chesnok, N. G., 2009, *MNRAS*

Additionally, a paper based upon the work in Chapter 5, is in preparation.

The published papers have been reformatted to comply with the University's thesis requirements, specifically the last point in the list above, and edited to improve clarity and continuity of this document as a whole.

This thesis contains approximately 45 000 words.

Elmé Breedt Lategan
28 August 2009

Acknowledgements

I am deeply indebted to the following people, without whose support this study, and reaching the point of its completion, would never have been possible.

Firstly to my supervisor, Prof. Ian M^{c}Hardy, who introduced me to the engaging topic of AGN variability and provided advice and guidance throughout this study. Thank you for patiently answering my many questions and sharing your knowledge so enthusiastically.

Sincere thanks to Dr. Patricia Arévalo, with whom I had neverending discussions on the work in this thesis and who was willing to answer my questions even at odd hours across time zones. Thanks for your continued encouragement and many suggestions which made this work a success.

Also to Dr. Phil Uttley for many insightful comments and suggestions, especially on the statistics of red noise data, and for introducing me to *RXTE* data analysis. Thanks also for giving me the opportunity to present this work at the COSPAR meeting in Montréal, in July 2008.

My deepest gratitude to Prof. Ian M^{c}Hardy, Prof. Malcolm Coe and Mary White of the School of Physics and Astronomy for support and understanding that exceeded every level of expectation and allowed me to complete the final year of this study.

I received financial support from the University of Southampton and the South African National Research Foundation, through a SALT-Stobie scholarship. Without this, I would never have been able to come to Southampton and work on this project. I am extremely grateful for this opportunity.

I would like to thank the staff of the Liverpool Telescope and the Rossi X-ray Timing Explorer for their support of our long term monitoring programs. I am very grateful to Dr. Sergey Sergeev of the Crimean Astrophysical Observatory and Prof. Takeo Minezaki, of the MAGNUM group at the University of Tokyo, for making some of their monitoring data available to us for use in this project. Thanks also to Yu Sakata and Shintaro Koshida for the reduction of the MAGNUM data, to Dr. Matt Darnley (Liverpool John Moores University) for useful email discussions surrounding the ISIS image subtraction package and Dr. Alex Markowitz (University of California, San Diego) for providing the X-ray PSD parameters of NGC 7469 ahead of publication.

To numerous officemates over the years at Southampton for discussions astronomical and non-astronomical in nature, specifically Drs. Vanessa (McBride) Godfrey, Andrea Dieball, Daniel Summons and Robert Dunn — a great big thank you to you all. Special thanks must also go to Simon Harris, who understands computers in a way no-one else does, and who was always willing to help me out of my latest Linux fix with a smile.

To my dearest family, thank you for you support and encouragement to follow this dream, even when it meant moving to a different country and not seeing each other nearly as often as we would really like to.

Xenophin - thank you seems to small a word for everything you've been through with me over the past few years. You're the support I can always count on. Thanks for caring about what I do and for the endless supply of hugs and encouraging words that got me through these last few months. I am truly privileged to share life with *you*.

o o O o o

Now all glory to God, who is able, through His mighty power at work within us, to accomplish infinitely more than we might ask or think.

— Eph. 3:20, NLT

For Xenophin

1 Introduction

Active Galactic Nuclei (AGN, or Active Galaxies) are among the most luminous objects in the universe, at any wavelength of observation. While the light observed from ‘normal’ galaxies is the combined emission from their constituent stars, active galaxies additionally produce an extraordinary amount of energy at their cores. The energy is radiated in a definitively broad spectrum from radio to γ-rays and the emission is known to be highly variable. The short time-scale of variability of the high energy emission constrains the size of the emission region to only about the size of the solar system, yet it is so powerful that the nucleus can outshine its host galaxy. In this study, I will focus on a particular subtype of AGN, the Seyfert galaxies. Seyfert nuclei account for about 10% of all nearby galaxies (Ho et al., 1997) and are found predominantly in spiral galaxies.

I start this chapter by introducing the properties and characteristics of AGN important to this study. I also briefly discuss their vast and rather complex classification scheme and the current paradigm for their geometry and structure, known as *the unified model*. The work in this thesis is centred on the relationship between the X-ray and optical emission we observe from these systems, so I will describe where this emission is generated and what we can infer about the physically separated emission regions from the relationship between their observed variations. Previous studies of this topic produced a confusing array of results. I will summarise their main findings and the development of this field of research in the third section of this chapter, and then conclude with an outline of the objectives of this study and a summary of the chapters to follow.

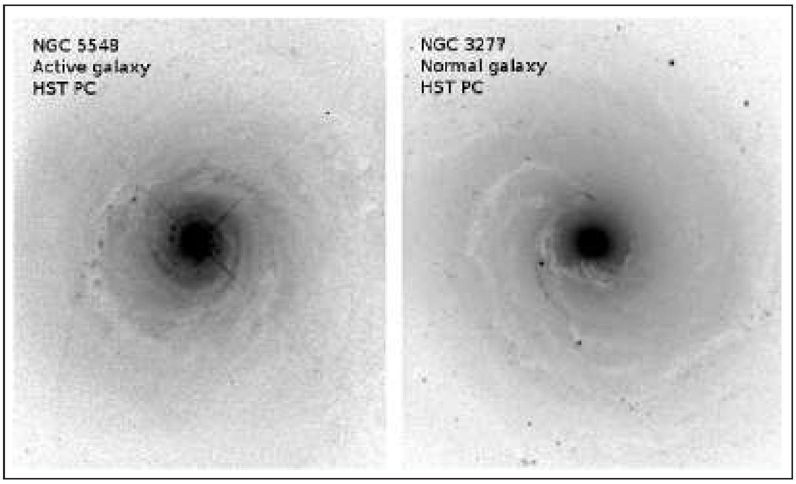

Figure 1.1: Optical images from the Hubble Space Telescope's Planetary Camera, showing the active galaxy NGC 5548 on the left and a similar, but non-active galaxy, NGC 3277, on the right. The nucleus of the active galaxy is much brighter, saturating the detector and leaving bright diffraction spikes in the image. The scale of the images are $25'' \times 30''$. Image credit: Bill Keel, University of Alabama (colour inverted for printing purposes).

1.1 Active Galaxies

Active Galactic Nuclei are extremely luminous, compact galaxy cores, found in ~20–40% of galaxies[1] (Ho et al., 1997; Miller et al., 2003). An example image of an active galaxy, NGC 5548, versus a non-active galaxy of similar type and distance, NGC 3277[2], is shown in Figure 1.1. The active nucleus is much brighter than the non-active nucleus — it saturated the detector, bleeding charge into neighbouring pixels above and below the nucleus, and produced prominent diffraction spikes (caused by the secondary mirror's support structure in the telescope). No such features are seen in the image of NGC 3277.

The classification of AGN is based upon their observational characteristics, and because of the historical development of the subject, the classification scheme is vast and rather complicated. Seyfert galaxies were first recognised as a distinct class in 1943 by Carl Seyfert, who was studying the optical spectra of six galaxies noted for their bright central cores and strong emission lines (Seyfert, 1943). The spectra of 'normal' galaxies generally show the deep absorption lines seen in stellar spectra, and are generally devoid of emission lines. The spectra of the galaxies in

---

[1] Ho et al estimate calculated from 486 galaxies at redshift $z \sim 0$, Miller et al estimate from 4921 galaxies between $0.05 \leq z \leq 0.095$

[2] Note that this is NGC 3277, not the active galaxy NGC 3227, which will be discussed later.

Seyfert's study however, showed high excitation emission lines which were heavily Doppler broadened (widths of $1000 - 10\,000$ km s^{-1}).

Surveys following the work of Seyfert discovered many more such galaxies, and it soon became clear that there were differences even among the Seyfert spectra. They were classified as either Type 1 or Type 2, depending, respectively, on whether their optical spectra contained both broad and narrow permitted and forbidden emission lines, or if the permitted and forbidden emission lines were of similar narrow width ($\sim$1000 km s^{-1}). The Seyfert classification scheme has since been extended to identify intermediate types (1.2, 1.5, 1.8 and 1.9) based on their detailed spectroscopic properties.

An alternative classification is based on their radio emission. About 15% of active galaxies are classed as radio-loud (Urry and Padovani, 1995, and references therein), the rest show a marked reduction in luminosity at radio wavelengths and are classified as radio-quiet. The radio emission is generally attributed to synchrotron emission from a powerful jet of relativistic electrons originating from near the central engine. The jets can extend several tens or hundreds of kpc away from the central galaxy, often symmetrically, blowing large *radio lobes* into the surrounding intergalactic medium. Radio-loud objects were further classified into FR I (lower luminosity, core-dominated) or FR II (high luminosity, lobe-dominated) type sources by Fanaroff and Riley (1974). Seyfert galaxies generally have weak radio emission and the jet is thought to be weak or absent.

Quasars were first identified in the late 1950s as a result of large radio surveys. Many of the bright radio sources detected in these surveys were identified with galaxies, but others appeared to be related to sources which resembled individual stars in optical images. Their spectra however showed very broad emission lines at unknown wavelengths. Maarten Schmidt recognised the lines as a highly redshifted Balmer series in 1963. Their inferred redshift placed these objects at cosmological distances (Schmidt, 1963). This made these unknown *radio stars* or later, *quasi-stellar radio sources*, the most distant, most luminous objects known at the time. Radio-quiet versions were later discovered and the name changed to *quasi-stellar objects*, or QSOs. Osterbrock and Parker (1965) first noted the similarity between QSOs and Seyfert galaxies, and today they are generally recognised as the same type of object, forming a continuous range in luminosity (in the sense that a low luminosity quasar is indistinguishable from a high luminosity Seyfert 1 galaxy).

Blazars form another class of AGN, characterised by rapid, large amplitude optical variability and radio-loud spectra. Their characteristics are interpreted as due to relativistic beaming when viewed down the jet. Further categories of AGN may include LINERs (Low Ionization Nuclear Emission Region galaxies), whose spectra display strong lines of weakly ionized or neutral atoms such as O and OI, but weak lines of highly ionized atoms such as [OIII] and NeV which are normally found in the spectra of AGN (Heckman, 1980). Narrow-line Seyfert 1 galaxies (NLS1) also appear to form a distinct class. Although similar to classical Seyfert 1s, their broad Balmer emission lines are much narrower ($\sim$2000 $\mathrm{km\,s^{-1}}$) than normally found in Seyfert 1s. They also appear to be more rapidly variable than other Seyfert 1 galaxies.

For a detailed account of the historical development of the subject, and more detail on each of the different classes of AGN, the reader is referred to the texts by Robson (1996) and Peterson (1997).

The current paradigm of AGN holds that this wide variety of observationally determined classes of AGN is due to a selection effect and that all or most of these classes can be incorporated into a single, unified model (Section 1.1.2). Furthermore, it is now widely believed that all AGN are powered by the same mechanism: accretion of material onto a supermassive black hole at the centre of the active galaxy.

1.1.1 The central engine

One of the key arguments for the existence of a very compact object at the centre of AGN is the observed rapid variability of the X-ray emission. Figure 1.2 shows the X-ray light curve of the NLS1 galaxy NGC 4051. The galaxy displays variability on time-scales of a few hours to several years. The insert to the figure shows the significant flux variations which can occur over a time-scale as short as one day. A simple argument sets an upper limit on the size of the emission region: variations originating from a region with size scale R, are smoothed out by the difference in light travel time to the observer from the nearest and the furthest sides of the emission region, by an amount $\Delta t = R/c$. Inverting the argument, this means that if we observe variability on time-scales of Δt, the size of the emission region must be of order $R \sim c\Delta t$. For the fast variations observed in AGN, this implies that the X-ray emission must be coming from a region only a few light-hours across. Furthermore, the fact that the active nuclei are not resolved by Hubble Space Telescope (*HST*) images, implies, for nearby galaxies at least, that the nucleus is less than $\sim$1 pc in size.

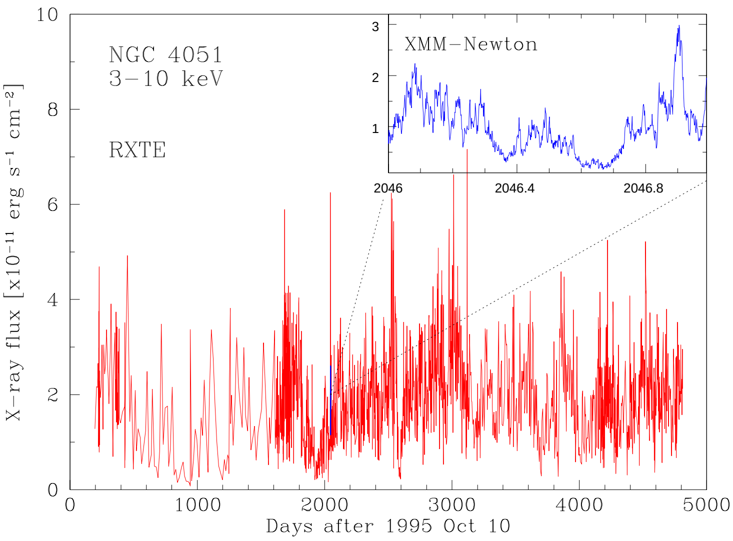

Figure 1.2: X-ray light curve of NGC 4051, showing variability on a wide range of time-scales. The rapid variability on time-scales of less than a day shown in the insert is one of the key arguments for the existence of a supermassive black hole at the centre of the galaxy (see text).

AGN have typical luminosities of 10^{44}–10^{47} erg s^{-1}. To produce such a tremendous amount of energy in such a small volume requires a very efficient method of energy conversion. This energy generating mechanism is what is commonly referred to as the *central engine*.

Optical emission

It is now widely accepted that the only process which can generate energy with a high enough efficiency is accretion onto a compact object. The intense radiation pressure generated by a source with such high luminosity must be counterbalanced by an opposing gravitational force of similar or greater magnitude, otherwise the source would be blown apart. The maximum luminosity of a spherically accreting source of mass M is known as the *Eddington luminosity*,

$$\begin{aligned} L_{\rm Edd} &= \frac{4\pi G c m_p}{\sigma_T} M \\ &= 1.26 \times 10^{38} (M/M_\odot) \text{ erg s}^{-1} \end{aligned} \tag{1.1}$$

where m_p is the mass of a proton and σ_T is the Thomson cross-section. The assumption is made that the main interaction between the radiation and matter occurs via Thomson scattering. So for typical AGN luminosities, equation 1.1 implies that a mass of $10^6 M_\odot - 10^9 M_\odot$ is required to balance the radiation pressure. Note that this 'maximum' luminosity may be violated if it does not meet the assumptions of steady accretion, or, especially, spherical symmetry. It is nevertheless useful as an estimate of the maximum luminosity, and estimates of the mass based upon it are broadly consistent with those inferred from the widths of the broad Balmer lines. The line broadening is interpreted as due to the Keplerian motion of the BLR clouds in the gravitational field of the central mass (see e.g. Peterson and Wandel, 2000, and references therein).

The flow of gas onto the black hole is thought to occur via an accretion disc, as this is the most energy-efficient way for the gas to release its angular momentum and flow towards the compact object. Although some details concerning the observations of inferred accretion discs are not yet fully understood, accretion theory is a well-studied subject. As it such an efficient process it is thought to occur widely throughout the universe, on many different size- and time-scales. The reader is referred to the excellent text by Frank, King and Raine (2000) for a review of the subject.

Ordinary molecular viscosity is too small by several orders of magnitude to facilitate the outward transfer of angular momentum in the disc. The nature of the viscosity operating in accretion discs is not well understood, but magnetic fields in the disc can provide an 'effective viscosity' through a magnetohydrodynamic disc instability, known as the magneto-rotational instability (Balbus and Hawley, 1991). The resulting 'magnetohydrodynamic turbulence' is widely accepted as the mechanism by which angular momentum is transported outwards, allowing matter to flow inwards towards the black hole. The gravitational potential energy released as a result of this inflow is radiated as observable emission[3]. Magnetohydrodynamic turbulence is mathematically a highly complex process, generally modelled in an accretion disc using numerical methods. Early attempts at an analytical solution of accretion disc structure (Shakura and Sunyaev, 1973), parametrised the (then unknown) viscosity in the form $\zeta = \alpha_{\rm disc} c_s H$, analogous to eddies in ordinary hydrodynamic turbulence. Here ζ is the disc viscosity, c_s the sound speed in the disc, given by the square root of the ratio between the pressure and density in the disc, H is a vertical scale height and $\alpha_{\rm disc}$ a constant $\lesssim 1$. With this parametrization the disc structure equations may be solved analytically (see e.g. Shakura and Sunyaev, 1973; Frank et al., 2002) and the solution is commonly referred to as the "Shakura

---

[3] If the flow is radiatively inefficient, such as in an ADAF (Narayan and Yi, 1995), part of this energy is advected inwards and the observed luminosity will be lower

& Sunyaev α-disc". Although this method does not further our understanding of the physics at work (it simply incorporates all uncertainties regarding the viscosity into a single parameter) it is still widely in use as a first approach to estimate accretion disc parameters.

Most relevant to this study, is that the temperature of such a geometrically thin, steady accretion disc, heated by viscous dissipation, is expected to follow a radial dependence

$$T(r) = \left[\frac{3GM\dot{M}}{8\pi\sigma}\frac{1}{r^3}\left(1-\sqrt{\frac{r_{\rm in}}{r}}\right)\right]^{\frac{1}{4}} \tag{1.2}$$

where M is the mass of the accreting compact object, $\dot{M}$ the disc accretion rate, r the radial distance from the black hole, and $r_{\rm in}$ is the inner radius of the disc. Writing this equation in terms of the gravitational radius $R_g = GM/c^2$ and Eddington accretion rate $\dot{M}_{\rm Edd} = L_{\rm Edd}/\eta c^2$, and writing $R = r/R_g$, we obtain

$$T(R) = 3.8\times 10^6 \left(\frac{\dot{M}}{\dot{M}_{\rm Edd}}\right)^{\frac{1}{4}} \left(\frac{M}{10^6 M_\odot}\right)^{-\frac{1}{4}} \left(\frac{R}{R_g}\right)^{-\frac{3}{4}} \text{ K.} \tag{1.3}$$

for large radii, $r \gg r_{\rm in}$. The efficiency η of the accretion process may be expressed as the mass inflow rate $\dot{M}$ required to produce a luminosity $L_{\rm acc} = \eta\dot{M}c^2$. The efficiency depends on the spin of the black hole, as this determines how deep into the potential well of the black hole the gas can sink before reaching the last stable orbit, and hence how much gravitational potential energy is released. The efficiency increases from $\eta \sim 6\%$ for a Schwartzchild (non-spinning) black hole to $\eta \sim 42\%$ for a maximally rotating (Kerr) black hole. For comparison, nuclear fusion, which powers stellar emission, is only $\sim 0.7\%$ efficient (e.g. Frank et al., 2002). For typical AGN masses equation 1.3 evaluates to $T \sim 10^5 - 10^6$ K, placing the thermal emission from the disc in the UV/optical emitting part of the spectrum.

Although accretion discs cannot be resolved, the *big blue bump* is commonly interpreted as thermal radiation from an optically thick accretion disc surrounding the black hole. The big blue bump is the dominant feature in the energy spectra of AGN at UV to EUV energies, and is generally thought to be of thermal origin, although there is still some uncertainty whether it is optically thick (blackbody) or optically thin (free-free) emission. A thorough review of accretion discs in AGN may be found in Koratkar and Blaes (1999).

In the simplest approximation, the disc may be assumed optically thick and radiating locally in blackbody form. The emitted spectrum F_ν can then be approximated by integrating the Planck spectrum throughout the disc with the derived radial temperature profile (Eqn. 1.2). This yields

$$F_\nu = \frac{4\pi h \cos i\, \nu^3}{c^2 D^2} \int_{R_{\rm in}}^{R_{\rm out}} \frac{R\, dR}{e^{h\nu/kT(R)} - 1} \tag{1.4}$$

for a system a distance D from the observer and at an inclination i (Frank et al., 2002). Notice that this equation is independent of viscosity. For low frequencies $\nu \ll kT(R_{\rm out})/h$, equation 1.4 gives $F_\nu \propto \nu^{-2}$ and for high frequencies $\nu \gg kT(R_{\rm in})/h$, it becomes $F_\nu \propto \nu^3 e^{-h\nu/kT}$. These results stem from the Rayleigh-Jeans and Wien approximations of the Planck spectrum, respectively. For intermediate frequencies it can be shown that $F_\nu \propto \nu^{1/3}$, which is sometimes referred to as the 'characteristic disc spectrum'. Observed spectra of accretion discs are generally found to be much redder (e.g. $\nu^{-0.44}$, Vanden Berk et al., 2001) than predicted by the characteristic spectrum, probably because of the sensitive dependence of the shape of the spectrum on the disc temperature profile (Gaskell, 2008), and perhaps indicating that it is too simplistic a model to describe the emissivity properties of real accretion discs. However, Kishimoto et al. (2008) have recently observed a very good fit to the predicted $\nu^{1/3}$ spectrum in *polarised* infrared emission from several quasars. The near-infrared emission is usually dominated by the torus (see Section 1.1.2), but the polarised component is interpreted to be infrared emission originating from the outer regions of the accretion disc, scattered into our line of sight by the equatorial scatterer also thought to exist in Seyfert 1 galaxies (e.g. Smith et al., 2002). Their result seems to indicate that at least in the outer parts of the disc, the local blackbody assumption is approximately correct.

X-ray emission

The high energy emission probes the very innermost regions of an active galaxy, so it is of great importance to our understanding of the working of these systems. It is often a major contributor to the bolometric luminosity of an AGN, yet the origin of this X-ray emission is not very well understood. The currently favoured model involves an optically thin corona above the inner disc (Sunyaev and Titarchuk, 1980) which inverse Compton scatters UV/optical photons into X-ray energies. The UV/optical seed photons for this process is supplied by the inner accretion disc. The corona may be heated by magnetic reconnection events in the disc (di Matteo, 1998), similar to what is thought to occur in the solar corona.

The observed power law spectra in AGN can successfully be reproduced by

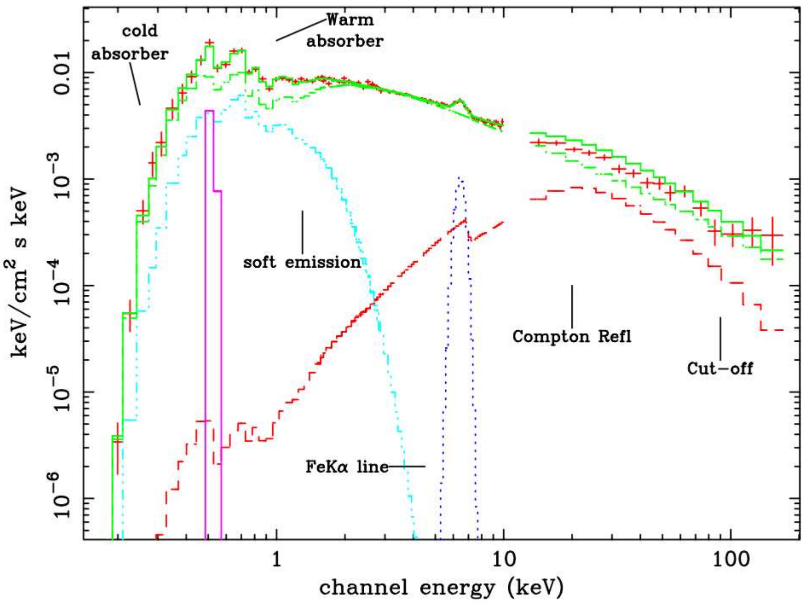

Figure 1.3: Broad-band X-ray spectrum of NGC 3783, showing the typical components contributing to a Seyfert 1 X-ray spectrum. *Figure from:* De Rosa et al. (2002).

Comptonization models like these (Haardt and Maraschi, 1991), but the power law is also modified by several other components (see Figure 1.3). There may be a cut-off at high energies due to electron-positron pair production ($\gamma + \gamma \rightarrow \mathrm{e}^- + \mathrm{e}^+$) in the compact corona, although the exact shape and energy of the cut-off is not well established. On the low energy end (especially below ~ 0.5 keV), the spectrum is absorbed by cold gas in the vicinity of the nucleus, commonly referred to as the *cold absorber*. At energies $\lesssim$2 keV, there are further absorption features in the spectrum, usually attributed to absorption by heavy elements such as Fe, Mg, Si and S. The absorption is variable and appears to vary with the incident continuum flux (Halpern, 1984). Hence it is known as a *warm absorber*.

Further support for the existence of an accretion disc comes from observations of the Compton reflection hump ($\sim 10 - 50$ keV) and Fe Kα fluorescence line seen in the spectrum at 6.4 keV (George and Fabian, 1991). This line is thought to originate from the reflection of X-rays by relatively cold material (such as the accretion disc) within a few gravitational radii of the black hole. The heavily broadened and redshifted profile expected from a line originating this close to the black hole agrees very well with observations (Tanaka et al., 1995). Many source also display a narrow component of the Fe line, which suggests that the X-rays are also reflected by cold material much further from the black hole (Nandra, 2001).

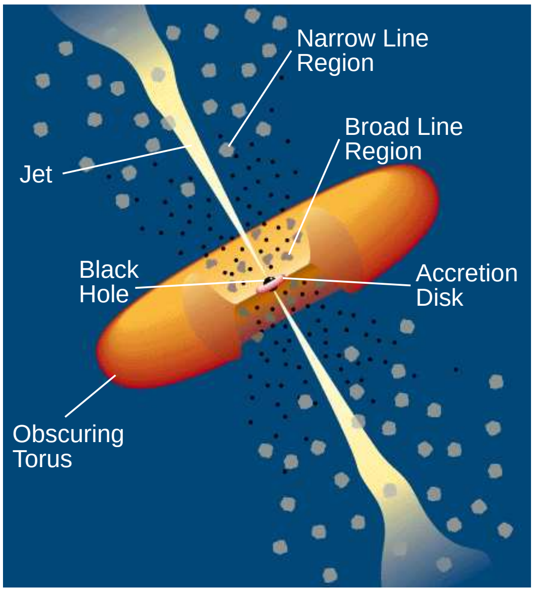

Figure 1.4: Schematic diagram of the AGN unification model, as described by Urry and Padovani (1995). The jet component is generally very weak or absent from Seyfert galaxies. When viewed at a high inclination angle (where edge-on is implied by $i = 90°$and face-on by $i = 0°$), the torus obscures the disc and BLR and the system is classified as a Seyfert 2. A Seyfert 1 galaxy is observed when viewing the system at a lower inclination angle ($i \lesssim 50°$), so that the disc and BLR is visible behind the torus. Image from NASA HEASARC.

1.1.2 The unified model

A key step towards a global understanding of active galaxies was the discovery of polarised broad line emission from the Seyfert 2 galaxy NGC 1068 (Antonucci and Miller, 1985). The spectrum of its unpolarised light displays typical Seyfert 2 characteristics, the broad emission lines being absent. The polarised flux, however, reveals a broad line spectrum, typical of Seyfert 1 nuclei. They proposed that the BLR and continuum source in this galaxy was hidden from our view by a thick disc (now mostly referred to as a dust torus, although warped disc models cannot be excluded). Electrons at the poles of the torus scatter the BLR emission into our line of sight, hence it can be seen in polarised light. This provided the first evidence that Type 1 and Type 2 Seyferts may intrinsically be the same type of object.

The current paradigm is that all classes of AGN are the same type of object; the observed differences being the result of a range of intrinsic luminosities and the different characteristics presented by a system with axial (rather than spherical) symmetry, when viewed from different angles. The main components of the unified model are a supermassive black hole, an accretion disc emitting at UV/optical wavelengths, optically thick clouds in Keplerian orbits around the black hole, known as the *broad line region* (BLR), the low density, low velocity clouds much further away known as the *narrow line region* (NLR) and finally a dusty torus which restricts our view of the continuum and BLR when viewed from high inclination angles. A schematic diagram illustrating the relative geometry of these components is shown in Figure 1.4.

The torus is a key component of the unification model, since it provides the obscuration of the inner components, and hence the observed difference between Type 1 and Type 2 Seyfert galaxies. It also accounts for intermediate Seyfert types, where only part of the BLR is in view. The dust absorbs radiation from the high energy source at the centre of the system and re-radiates this energy thermally. The X-ray spectra of Seyfert 2 galaxies show significant absorption below energies of 2–3 keV (e.g. Moran et al., 2001). The absorption is consistent with viewing the central source through a high column density of cold material, as may be expected if the central source is obscured by the molecular torus. From an X-ray point of view it is not clear whether *all* Seyfert 2 galaxies are absorbed Seyfert 1s or whether there is an intrinsic difference between their emission mechanisms. There is some evidence that the reflection component may be stronger in Type 2 systems than in Type 1 systems (Moran et al., 2001).

The dust probably consists mostly of graphite and silicate particles, so it is believed to sublimate at temperatures above 1500 – 2000 K (Draine and Lee, 1984). The torus must therefore be at a similar temperature or cooler, meaning that it radiates primarily at NIR – FIR wavelengths. The same principle can be used to estimate the inner radius of the torus: dust will start forming at the minimum radius at which it can exist without being sublimated by the radiation of the central source, i.e. where the continuum flux is low enough so that the dust is not heated to its sublimation temperature. This distance is known as the *sublimation radius*.

Radio-loud objects are thought to host a powerful radio jet as well, probably launched from the inner parts of the disc, although the exact process of jet formation and acceleration is not well understood. The characteristic violent variability displayed by blazars is thought to be a result of viewing the system close to the axis of this jet, so that the emission is enhanced by relativistic beaming.

It is worth mentioning that although most of the observed characteristics of AGN can be accounted for within the framework of the unified model, there are some unresolved issues. Notably, the basic model does not offer a reason why some objects are radio-quiet and others are radio-loud. It is possible that another fundamental parameter, such as the black hole spin (Wilson and Colbert, 1995), is necessary in order to explain the properties of all AGN. Similarly, NLS1 galaxies also seem to require an additional parameter to explain their relatively narrow broad lines and very rapid variability. The narrower lines probably point to a lower mass central black hole (and consequently lower Keplerian velocities of the BLR clouds), but since their luminosities are comparable to other Seyfert 1s, the black hole must be accreting at a high rate in these systems. It therefore seems that differing disc accretion rates may have a marked influence on the observed characteristics of AGN.

The unified model nevertheless has the attractive feature that it explains the majority of AGN phenomena with minimal parameters. The basic geometry of this model is assumed throughout this work.

1.2 X-ray and optical variability

As mentioned before, the rapid variability observed from AGN constrain the X-ray emitting region to the innermost regions of the system, close to the black hole. The exact geometry of the emission region or proposed corona is however highly uncertain. Variations in the available seed photons to be upscattered will be directly translated into variations of the emitted X-rays. Since more scatterings are required to produce higher energy photons, there will be a delay of the variations in a higher energy band with respect to those at lower energies. The length of the delay depends on the size and optical depth of the Comptonizing region and the separation between the energy bands under investigation.

The UV/optical emission in Seyfert galaxies is believed to originate in an accretion disc around the black hole, at least part of which is optically thick and geometrically thin (e.g. Shakura and Sunyaev, 1973; Koratkar and Blaes, 1999). AGN have been known to exhibit optical variability since shortly after their discovery (e.g. Smith and Hoffleit, 1963), but the origin of the optical variations, as well as the connection between the disc and the corona, is still unclear.

On account of the near-simultaneity of the observed X-ray and UV variations (Section 1.3), it was suggested (Krolik et al., 1991; Collin-Souffrin, 1991) that the UV and optical variations may be due to reprocessing of the variable X-ray emission by the optically thick accretion disc. The X-ray source illuminates the disc from above, enhancing the intrinsic thermal emission of the disc. Reprocessing occurs on the hydrogen recombination time-scale, which, given the high density of gas in the inner part of the central engine, may be safely approximated as instantaneous (Peterson, 2006). Any measurable delay should thus be due to light travel-time effects. As a result, the fast variations of the X-ray emission will be imprinted onto the optical light curve, albeit smoothed by the spatial extent of the disc and delayed by the light travel time between the source and the disc.

A natural consequence of the $R^{-3/4}$ dependence of the disc temperature (Eqn. 1.3) is that there will be a delay between variations in different wavebands, owing to the fact that they are emitted from different characteristic radii. The delay τ is given by the difference in light travel time to the regions of different temperature, so that $\tau = R/c$ and hence $T \propto R^{-3/4} \propto \tau^{-3/4}$. The peak of the emission of wavelength λ is given by Wien's law as $T \propto \lambda^{-1}$, resulting in a wavelength-dependent delay $\tau \propto \lambda^{4/3}$. Such delays have been observed in several sources (e.g. Wanders et al., 1997; Collier et al., 1998; Oknyanskij et al., 2003; Sergeev et al., 2005; Cackett et al., 2007) lending further support to the accretion disc model of the central engine.

Also important to consider, is variability intrinsic to the disc, such as instabilities propagating radially inward through the disc, affecting the mass accretion rate and local emission (e.g. Lyubarskii, 1997; Arévalo and Uttley, 2006). In this case, optical variations are expected to precede similar variations in the X-rays. The time-scales involved are much longer, as variations will propagate on the viscous time-scale, which is ∼months–years at the optical emitting region in AGN.

The long term (∼months–years) optical variability has been explained by composite models including accretion rate fluctuations propagating through the disc (Arévalo and Uttley, 2006; Arévalo et al., 2008) and changes in the geometry of the system (Breedt et al., 2009, Chapter 3 of this thesis). Reprocessed emission from the broad line region may also contribute to the optical variations (Korista and Goad, 2001; Arévalo et al., 2009). Gaskell (2007) suggested that there might be a contribution to the optical emission from reprocessing material much further out, such as the dust torus.

By undertaking simultaneous multi-wavelength monitoring and studying the relationship between the emission at different wavelengths, we can determine the dominant process underlying the optical variations and gain some physical insight into the connection between the emission regions. The analysis and comparison of the variations in different wavebands rely on a well-known statistical technique known as *cross-correlation*. I discuss the basic theory of cross-correlation functions as well as its specific application to this study in detail in Appendix A. The technique has been successfully applied in AGN as part of reverberation mapping studies to determine the size of the broad line region and the mass of the central black hole (e.g. Kaspi et al., 2000; Peterson et al., 2004; Kollatschny, 2003; Denney et al., 2006; Bentz et al., 2007).

Besides simply measuring the optical–X-ray lag, coordinated X-ray and optical monitoring observations enable us to put other useful constraints on the X-ray and optical emission processes and on the geometry of the emitting regions. For example, the greater fractional variability of the X-rays on short ($\sim$day) time-scales indicates that, in a Compton scattering scenario for the X-ray production, at least part of the X-ray variability is not produced by variable up-scattered seed photons, but by variations in the scattering corona itself. The relative amplitude of optical and X-ray variability is also important because if the optical variations, which represent variations in the bolometrically dominant blue bump, exceed those in the X-rays, it is hard to explain the optical variations as purely due to reprocessing, e.g. as in NGC 5548 (Uttley et al., 2003) and MR2251-178 (Arévalo et al., 2008). In these AGN the large amplitude optical variations occur on time-scales of years and may represent accretion rate fluctuations propagating through the emission region.

AGN also display spectral variability, i.e. changes in the ratio of hard to soft X-rays emitted. Generally it is found that the spectrum steepens (becomes softer) as the source gets brighter (e.g. Lamer et al., 2000; Papadakis et al., 2002; Sobolewska and Papadakis, 2009). Variability of this type is consistent with thermal Comptonization models: an increase in the soft photon flux leads to a decrease in the corona temperature, and hence an increase in the soft X-ray flux. Two models for spectral variations exist: *i*) a 'two-component' model consisting of a soft component of constant spectral slope but variable flux and a hard constant component (M^{c}Hardy et al., 1998), and *ii*) a 'spectral pivoting' model where the spectral slope pivots around some high ($\sim$ 60 keV) energy (Zdziarski et al., 2003). Some sources, e.g. MCG-6-30-15 display variations consistent with a two-component model, but others, such as NGC 4051, show evidence of spectral pivoting (Taylor et al., 2003).

In this work I will investigate the relationship between the X-ray and optical emission by correlating the 3–10 keV X-rays with the optical flux. Hence the 3–10 keV flux is used as a proxy of the total variable X-ray emission as seen by the accretion disc. In order to correct for this approximation in energy terms, the 3–10 keV luminosity is multiplied by a constant factor to convert the flux to the average total X-ray luminosity, as determined from the broad band X-ray spectrum (Yang et al., 2007). It is therefore possible that some of the X-ray flux variations seen in the 3–10 keV band are due to spectral variability, without an associated change in luminosity (e.g. as is observed in NGC 5548; Petrucci et al. 2000). The disc of course responds to changes in the total luminosity, so the optical response will not necessarily be as dramatic as seen in the X-rays, or there may be X-ray variations without corresponding changes in the optical emission. However, these spectral changes will only strengthen our conclusions, since the additional variability which may be present in the X-ray band will reduce the strength of our correlations. It is however an energy-dependent problem, as the reprocessed fraction (i.e. the disc albedo) depends on the energy of the input spectrum. A more detailed investigation into the effect of spectral changes on the variability of the reprocessed emission will be deferred to a future study.

1.3 Previous results

The potential science return of multi-wavelength monitoring of AGN is indisputable. Variability studies provide a way of probing the unresolved nucleus in more detail than any other method and have the potential of revealing the direct relationship between physically separated parts of the system. However, such studies are complicated by the difficulties of obtaining and scheduling the large amounts of coinciding observation time on multiple facilities that is required to search for correlated variability.

Many of the early studies of X-ray and optical variability formed part of a large campaign to monitor AGN over a wide range of wavelengths. The main aim of the consortium of about 100 astronomers, known as the AGN Watch, was to obtain high quality continuum and emission line variability data of a sample of AGN, to study their characteristics over multiple wavelengths. A summary of the program and their main results are presented by O'Brien and Leighly (1998) and Peterson (1999). Data from this program are publicly available[4].

Overall, these studies (along with others prior and subsequent to the AGN Watch campaign) yielded varied and confusing results regarding the relationship between the X-ray and UV/optical variability. Some sources showed well correlated variations, at least one appears to have no correlation at all and others yielded conflict-

---

[4] At http://www.astronomy.ohio-state.edu/∼agnwatch/

ing results from the same source. In the following section I will summarise some of the main results and then introduce the rationale for the present study.

1.3.1 A confusing picture

The first study searching for X-ray/optical variability correlations in Seyfert galaxies, was that of Done et al. (1990), who monitored the NLS1 galaxy NGC 4051 over two nights using a ground based optical telescope along with monitoring by the *Ginga* X-ray satellite. Surprisingly, they found the optical flux to vary less than 1% during this time, while the X-rays showed a factor of two change in flux. The result demonstrated that the X-rays and optical emission could not be part of the same same emission process (e.g. both originating from synchrotron emitting electrons), but it could not constrain the relationship between different emission regions any further.

Probing slightly longer time-scales, Clavel et al. (1992) monitored NGC 5548 in X-ray and UV as part of the AGN Watch campaign. They report a ≤ 6 day lag in the X-ray to optical variations, but an additional earlier observation dramatically reduced the strength of the correlation. They explained their results in terms of a two-component model, in which one part of the UV/optical emission is due to reprocessing of X-rays and another due to internally generated thermal emission from the viscous disc itself. Edelson et al. (1996) reached a similar conclusion for NGC 4151, reporting a strong X-ray/UV correlation consistent with zero lag (≤ 0.15 day).

With the launch of the *Rossi X-ray Timing Explorer* satellite (*RXTE*) in 1995, greatly improved sampling of X-ray light curves became possible, as well as the ability to continuously monitor X-ray sources over medium- and long time-scales.

UV and optical light curves from *HST* observations of NGC 7469, presented by Collier et al. (1999), showed lags consistent with the $\tau \propto \lambda^{4/3}$ prediction of reprocessing models. On the contrary, simultaneous *RXTE* and *IUE* observations of the same source revealed a complicated relationship (Nandra et al., 1998): the peaks of the X-ray variations led the UV variations by four days, but the minima in the light curves appeared to be near-simultaneous. Subsequent observations have shown that the UV flux was closely correlated with the X-ray spectral index, but only weakly with the X-ray flux (Nandra et al., 2000). This result points to a Comptonization origin, but the details of the interaction is not clear (see also Petrucci et al., 2004; Uttley, 2006).

NGC 3516 was monitored extensively by *RXTE* to search for long time-scale variability correlations. Based on one and a half years of X-ray and ground-based optical observations, Maoz et al. (2000) reported correlated variability with a 100 day lag in the X-ray to optical variations. No significant correlation was found at zero lag and they concluded that both the optical and X-rays reflect an instability in the accretion flow, propagating through the accretion disc. However, with the addition of three more years' monitoring data, they were unable to confirm the 100 day lag (Maoz et al., 2002). No other significant lag time-scale found in the data, nor a spectral index correlation as was reported in NGC 7469. On shorter time-scales, intensive three day monitoring of NGC 3516 by Edelson et al. (2000), showed strongly correlated hard (*RXTE*, *ASCA*) and soft (*ASCA*) X-ray light curves, but with no apparent relation to the optical *HST* continuum flux. No simple connection between the variability in X-rays and optical has been found in this source so far.

Support for a Comptonization origin of the variability comes from Uttley et al. (2000), who presented simultaneous EUV and X-ray light curves of NGC 4051 showing a strong correlation over the $\sim$10 day monitoring period. A small lag ($<$ 1 ks) of the X-rays behind the EUV was detected and, using Comptonization models, they constrained the size of the emitting region to $\leq 20R_g$ in this source. The UV emission in NGC 4051 lags the X-rays by 0.2 days, however (Mason et al., 2002; Smith and Vaughan, 2007), and Peterson et al. (2000) report a correlation between the X-ray and optical continuum fluxes on the time-scale of weeks to months. An intensive 3-month monitoring program by Shemmer et al. (2003) finds a good correlation between the X-ray and optical emission at zero lag, but also notes that at least some part of the optical variations lead the X-rays by about two days. All of these observations are probing different time-scales in the system, suggesting that different processes may drive the long and short time-scale variability. I return to this possibility in the following chapters.

Following a search for microvariability in NLS1 galaxies, Klimek et al. (2004) conclude that NLS1s as a class are not more variable in the optical than other Seyfert 1 galaxies. They found conclusive evidence of variability on time-scales less than a day only in NGC 4051, and only on one of the five nights it was monitored for.

Probably the first convincing case of correlated X-ray and optical variability in Seyfert galaxies was found by Uttley et al. (2003) in NGC 5548. The long term, large amplitude optical flux variations were closely correlated with the X-ray light curve over a time-scale of 6 years, but the sampling of the light curves was not sufficient to measure the delay between the bands to better than 0 ± 15 days. They also found that the amplitude of optical variations was larger than that of the X-rays. Viscous dissipation is expected to dominate the temperature profile and hence the emission of the disc, with the reprocessing of X-rays just adding a relatively small contribution to the flux. Hence if the amplitude of the optical variations is larger than the X-ray amplitude, reprocessing cannot be the main driver of the variability. Recently, however, Suganuma et al. (2006) reported a clear 1.6 day optical lag to the X-ray variations in NGC 5548 and an optical amplitude much smaller than the X-ray amplitude, suggesting that, unlike on the longer time-scales, reprocessing may be the main source of the optical variability on time-scales of days. Intensive monitoring by Gaskell (2006), however, fails to show this short time-scale correlation.

1.3.2 A possible mass dependence?

As we are seeking to understand the interaction between the optical and X-ray emitting regions, it is instructive to consider their relative location in the system (Uttley et al., 2003; Uttley, 2006). As discussed before, the X-ray emitting region is expected to be centrally concentrated in all AGN, within a few R_g from the black hole. Different parts of the optical spectrum arise from predominantly different parts of the accretion disc, however, as a consequence of the radial dependence of the disc temperature. Equation 1.3 shows that, at a given number of gravitational radii, a system with a very massive black hole and/or lower accretion rate, will have a cooler disc than a system with a lower mass black hole and/or higher accretion rate.

The location of the optically emitting part of the disc may be estimated by assuming local black body emissivity and integrating the derived temperature profile (Eqn. 1.2) throughout the disc. For example, assuming a standard accretion disc with an accretion rate of 10% of the Eddington value, 90% of the optical flux originates from within $240R_g$ of a $M = 10^8 M_\odot$ black hole. In a system with $M = 10^6 M_\odot$, however, $1100R_g$ is required to contain 90% of the optical emission. The characteristic disc time-scales at the optically emitting region, which scales with the gravitational radius R_g, are therefore very different in the two systems. This implies that in the $10^8 M_\odot$ system, the X-ray and optical emitting regions are "better connected", i.e. their *intrinsic* variations occur on similar time-scales, so that a strong correlation is observed between the medium- to long term variations ($\sim$months–years). On the contrary, in the $10^6 M_\odot$ system, the variations in the X-ray and optical bands may appear to be more independent as a result of the very different viscous time-scales at the X-ray and optical emitting regions. Hence the correlation on long time-scales is expected to be weaker in these systems.

The strength of the reprocessed component of the emission is determined by the solid angle the disc subtends to the X-ray source at the optically emitting region. Reprocessing may therefore dominate the *correlated* variability in the low mass systems, while in the massive systems we may expect a combination of reprocessing and longer term variations to produce the correlation.

1.4 Summary of this thesis

The main aim of this study is to do a comprehensive comparison between the X-ray and optical variability of a sample of Seyfert galaxies, specifically to determine the origin of the optical variations, and the effect of the black hole mass on the strength of the correlation between them. To this end, I present in this thesis an analysis of the longest yet concurrent X-ray and optical light curves of a sample of seven Seyfert galaxies, spanning a range in mass and accretion rate.

It is clear from the array of results produced by previous studies that more than one process may contribute to the optical variability, and that different processes may dominate the variability on different time-scales. The viscous time-scale at the optical emitting region in AGN is of the order of years or tens of years, so long term light curves are required if we were to include and understand the effects of fluctuations propagating on these time-scales.

Furthermore, AGN light curves display *red noise* variability, i.e. adjacent points in the light curves are correlated with each other, so that longer time-scale variations have a larger amplitude. This may cause peaks (or troughs) in two red noise light curves to line up even if the light curves are not really correlated. A few strong peaks in the light curves which match up by chance could therefore lead to a spurious result. The standard statistical tests of correlation strength assume completely uncorrelated data points, so these techniques cannot be used to determine whether the correlation is real or not. I will therefore assess the statistical significance of the correlations found using Monte Carlo simulations.

The remainder of this thesis is organised as follows:

Chapter 2 discusses the acquisition and reduction of the data I used in this thesis. I also discuss in detail the photometry methods I used to measure the galaxy fluxes, as well as the intercalibration of data sets I obtained from collaborators.

In Chapter 3 I show that the optical light curve of Mrk 79 displays clear long time-scale variability, which is not present in the X-ray light curve. I present a detailed analysis of the origin of the optical variability and show that it may be accounted for by a combination of reprocessing and a change of the geometry of the system or a variation of the mass accretion rate over time-scales of years.

Chapter 4 presents a detailed analysis of the lowest mass, lowest luminosity galaxy in our sample, NGC 4051. It also displays the fastest variations of all the galaxies in the sample, with an optical lag behind the X-rays consistent with reprocessing by an accretion disc. I show, however, that reprocessing cannot account for all the optical variations in this source and that there is some part of the optical flux variations which lag behind the X-rays by ∼40 days. I investigate the possibility of this being due to reprocessing and/or reflection by the dust torus.

In Chapter 5 I compare the variability properties and cross-correlation results of the monitoring sample as a whole. The optical emission is found to follow the X-rays with a short delay in all seven Seyfert galaxies under investigation, consistent with what is expected if the short time-scale optical variations are due to reprocessing of X-rays. I also show that there is evidence for a correlation between the strength of the X-ray/optical correlation and the black hole mass, as well as with the inferred accretion disc temperature.

Chapter 6 summarises the findings of this study and discusses possible directions for future, related research.

2 Observations and data reduction

All the X-ray light curves used in this study were constructed from data collected with the Rossi X-ray Timing Explorer satellite. Most of the optical data are from the Liverpool Telescope, with an additional small observing program on the Faulkes Telescope North. As part of a collaboration between our group and other observers, we have also obtained V band light curves from the Crimean Astrophysical Observatory and the MAGNUM group at the University of Tokyo. In this chapter I will describe the data collection and reduction procedures I used to construct the X-ray and optical light curves of the monitoring sample, as well as the combination of our optical light curves with those from collaborators.

2.1 X-ray observations

2.1.1 The Rossi X-ray Timing Explorer

The Rossi X-ray Timing Explorer Satellite (*RXTE*) was launched on 1995 December 30 as a mission designed to carry out high timing resolution observations of X-ray sources. It is operated by NASA's Goddard Space Flight Center.

It was launched into a 90 minute low earth orbit and is capable of rapidly pointing to a desired target, allowing multiple observations of the same source, at regular intervals. It is this characteristic which has proved most useful for the observations required to measure the X-ray power spectral densities (PSD) of AGN, as it allows us to probe the variability over a wide range of Fourier frequencies.

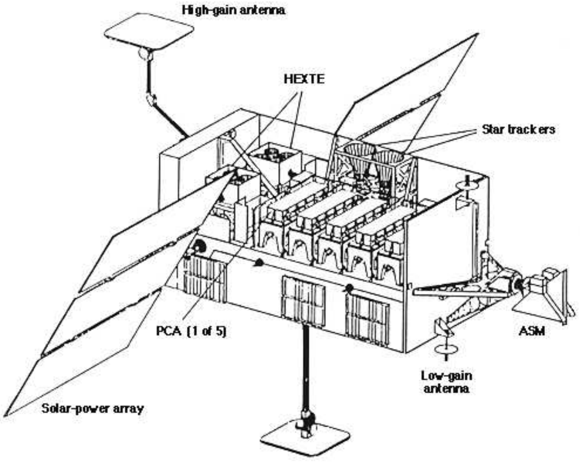

Figure 2.1: Schematic of the *RXTE* spacecraft, showing the location of the PCA. (*figure from* HEASARC)

The satellite is equipped with three science instruments: the All-Sky Monitor (ASM), the High Energy Timing EXperiment (HEXTE), and the Proportional Counter Array (PCA). For the work discussed in this thesis, only data from the PCA was used, so I will focus this discussion on that instrument only. The PCA consists of five Proportional Counter Units (PCUs), labeled 0 – 4. It is sensitive to photons in the energy range 2–60 keV. Each PCU contains three layers of Xenon gas as detection layers, and a top layer of propane. The bottom layers are more sensitive to harder photons, but for faint sources like ours, the counts detected these layers are mostly due to the background. As we are interested here in the details of the variability, rather than a wide energy range, we extracted data from the top layer only, to maximize the signal-to-noise of our measurements.

The PCA is a non-imaging instrument, so it cannot directly measure the background contaminating the source counts. Instead the background is calculated from a model which includes the effect of the particle environment around the spacecraft, induced radioactivity, the cosmic X-ray background and other sources that may add counts to the PCA measurement (Jahoda et al., 2006). After more than 12 years of RXTE operation, the background is well understood. The model was regularly updated during this time and in it latest form it provides an accurate description of the non-source counts added to the measurement.

The satellite was designed for a goal lifetime of five years (a minimum of two years required), but after more than 12 years it is still performing well. A further extension of the mission has recently been granted[1], extending its remarkably

---

[1] *RXTE* news website, http://heasarc.gsfc.nasa.gov/docs/xte/xhp_new.html#c14-announ

productive lifetime until 2010 September.

2.1.2 X-ray data reduction

All our observations were made with the PCA, in the form of approximately 1 ks snapshots. I used standard techniques to extract the source spectrum and model background spectrum for each observation, using the package FTOOLS v.6.4. All the available data were re-reduced, so that the latest background models may be applied throughout the light curve. PCU0 lost its propane layer following a micrometeorite striking the spacecraft in 2000 May. The same happened to PCU1 in 2006 December, dramatically increasing the background in these PCUs. Although this is now included in the background models, I do not extract data from these PCUs. Additionally, PCUs 1, 3, and 4 were regularly switched off during our observations, so I only use data from PCU2 to construct the X-ray light curves. I applied standard good time criteria, rejecting data obtained within 10 minutes of passing through the South Atlantic Anomaly (SAA), data for which the electron contamination was greater than 0.1, data gathered less than 10° above the limb of the Earth or data with pointing offset greater than 0.02° from the source. To obtain the flux measurements, I fit a power law model to the spectra using XSPEC v.11 and integrated the flux over the range 3–10 keV.

It is known that the unfolded spectrum produced by XSPEC is not model-independent, i.e. the shape of spectral features in the unfolded spectrum depends on the model used to fit the data (see, e.g. the XSPEC user manual[2]). This is particularly true at energies below 3 keV, where the detector effective area is low. For this reason, I used the integrated 3–10 keV flux rather than the usual 2–10 keV. Nowak (2005) suggests folding the spectrum through a power law of slope zero (i.e. a constant) rather than assuming a particular shape of the model. This technique weights the spectrum by the detector response only, so that the reported flux is a close representation of the actual photon counts detected. It therefore allows one to remove the effect of the energy-dependent effective area of the detector, while leaving the instrumental blurring of spectral features unchanged. The error on the flux may then be calculated simply by adding the error of the counts in each energy bin of the unfolded spectrum, in quadrature.

When fitting spectral lines or comparing different data sets (e.g. at different energies) it is obviously better to use a model-independent estimate of the flux.

---

[2] Available online from HEASARC,
http://heasarc.gsfc.nasa.gov/lheasoft/xanadu/xspec/manual/manual.html

However, for our long term monitoring data, I decided that it was better to use the model-integrated flux, as it allowed me to make a more consistent measurement over the whole of the monitoring period, in the following way. When integrating the model, one can account for the full energy range integrated over, including some photon leakage which may have occured, giving a true representation of the 3–10 keV flux. When simply summing the counts in the unfolded spectrum, the flux does not correspond to the full 3–10 keV energy range, but rather the edge of the first channel greater than 3 keV to the edge of the last channel less than 10 keV. Combined with the fact that there are slight changes in the response matrix between observations, the channel ‘edges’ do not always correspond to the same energies, so artificial variability will be added to the light curves.

Finally, the error on the final 3–10 keV flux was calculated as the same fractional error obtained from integrating the unfolded spectrum directly.

2.2 Optical observations

2.2.1 The Liverpool and Faulkes Telescopes

We (PI: I. M$^{\mathrm{C}}$Hardy) started an optical monitoring program of five Seyfert galaxies, in parallel with the *RXTE* observations, on the Liverpool Telescope (LT) in 2004 December. The sample was selected from the sources which had already been part of the *RXTE* X-ray monitoring program, and was specifically selected to span a range in mass and accretion rate. So far, the program has yielded 132 useful observations in the Bessell-V band for Mrk 79, 36 for NGC 3227, 141 for NGC 4051, 172 for NGC 4593 and 37 for NGC 5548. Additionally, we have a similar number of observations in the Sloan Digital Sky Survey (SDSS)-u band for Mkn 79, NGC 4051 and NGC 4593. Observations in the V band are still ongoing. Monitoring of a sixth target, Mrk 110, started in 2008 February and has so far yielded 112 V band observations.

The u and V band images were taken directly after each other, with a 60 s exposure time for the u filter and a 30 s exposure for the V filter. The sampling period was initially similar to that of the the X-ray observations, i.e. 2–4 days. In 2007 March, this was increased to daily monitoring in V and every two days in u for Mrk 79 and NGC 4051, and in 2008 March, the u band observations were dropped altogether in favour of daily V band sampling of all targets and an increase in the exposure time (45 s). Typical images of our monitoring targets are shown in Figure 2.2.

The Liverpool Telescope is a 2 metre fully robotic telescope at the Observatorio del Roque de Los Muchachos of the Instituto de Astrofisica de Canarias, La Palma, Spain (Steele et al., 2004). The telescope is operated by Liverpool John Moores University with financial support from the UK Science and Technology Facilities Council. For the observations discussed here, we used the optical CCD camera mounted on the telescope, RATCam, which hosts a 2048×2048 pixel back-illuminated detector. Our images are generally binned 2×2, resulting in a 1024×1024 pixel image of the $4.6' \times 4.6'$ field of view and a scale of $0.278''$ per binned pixel.

Basic data processing of RATCam images is done in a data reduction pipeline before it is passed to users. One of the main reasons for this is to ensure that the best flat field image is used to flat field the data. Flats for the different binning modes are taken at evening and morning twilight and stored as a reference library for the pipeline. Usually the twilight time is not enough to cycle through all possible filter and binning combinations, so the most recently updated master flat field image is selected from the reference library to flat field the data. It takes typically 2–3 nights to cycle through all the combinations, so the master flat, which is calculated from the median of the appropriate flat field images, is updated every $\sim$3 days.

The bias frames do not show any significant repeatable structure, so the bias correction is based on the underscan region only. A slow ramp in the column direction of the chip is removed with a smooth linear function. The data are then overscan-trimmed to give the 1024×1024 binned image. No bad pixel mask is applied as part of the pipeline processing, so a few hot pixels and one bad column on the chip were removed by linearly interpolating between adjacent pixels.

At the start of this program, the cooling pipes to RATCam and the near-infrared camera mounted on the telescope, SupIRCam, were routed through the telescope axis rotator. The pipes suffered problems with flexibility and restricted the angles at which the telescope could observe. This, together with the fact that the physical centres of the RATCam CCD and SupIRCam arrays are slightly displaced from the optical axis of the telescope, meant that the comparison stars were often lost off the edges of our images. This was particularly problematic for the observations of NGC 5548 and NGC 3227, where the comparison stars are quite close to the edge of the image. The field of view does not contain any other useful comparison stars, so this led to considerable data loss for these sources. In 2007 April, the cooling

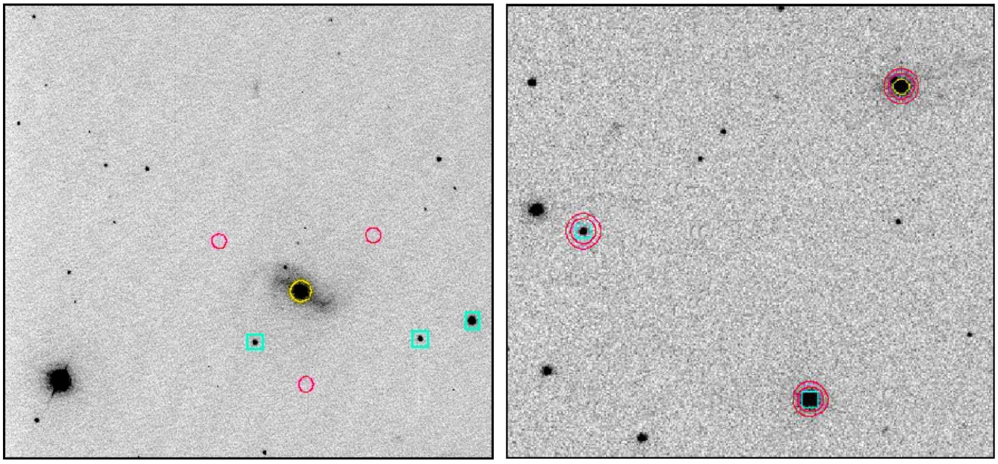

(a) Mrk 79 (b) Mrk 110

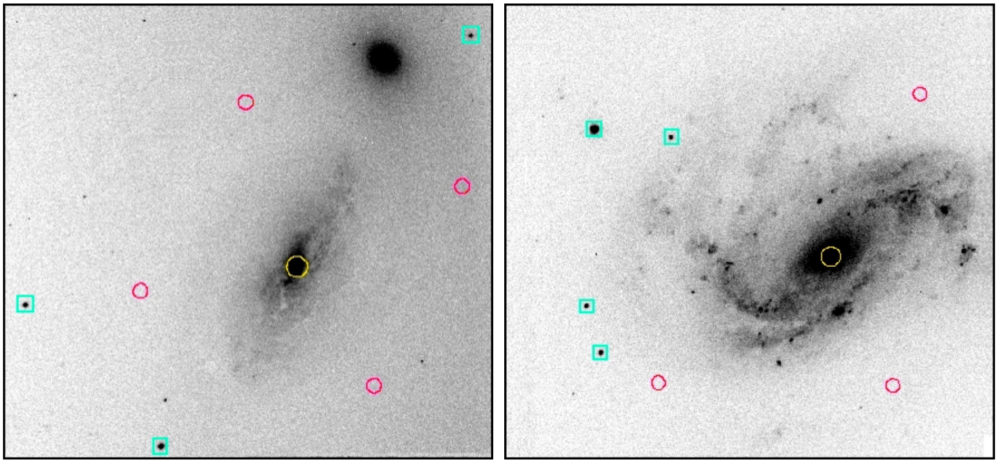

(c) NGC 3227 (d) NGC 4051

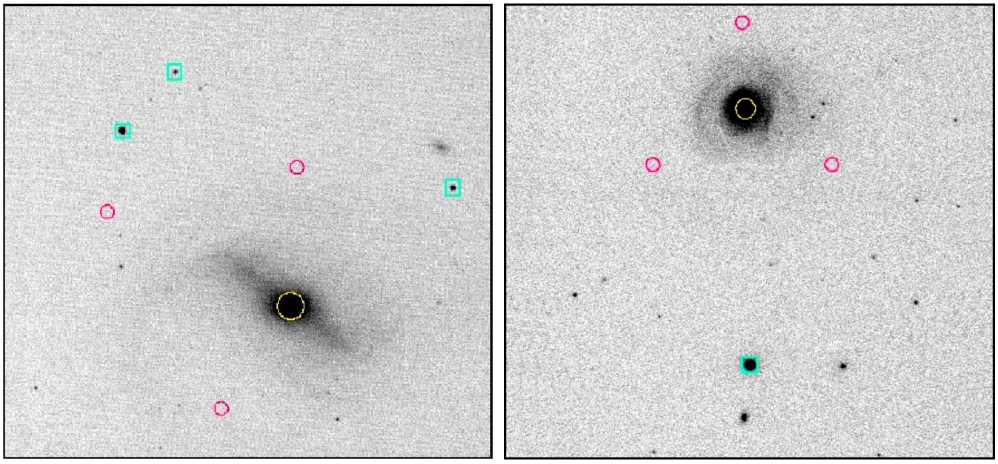

(e) NGC 4593 (f) NGC 5548

Figure 2.2: V band images of the Seyfert galaxies monitored with the Liverpool Telescope. Each image represents the $4.6' \times 4.6'$ field of view of the LT. North is up and East is to the left. The photometric aperture used for each galaxy is shown as a yellow circle centred on the nucleus ($12''$ diameter for Mrk 79, NGC 3227, 4051 and 5548, $18''$ for NGC 4593 and $8''\!.3$ for Mrk 110). The red circles indicate the positions where the sky background was measured. The comparison stars are marked with blue squares.

system was replaced, a correction for the chip offset was made and a "cardinal pointing" system was introduced. Images are now rotated to one of the "cardinal" sky angles (0, 90, 180 or 270 degrees), maximizing the overlap between repeated images of the same field. This has greatly improved the quality of our light curves. The current rms pointing of the LT is $6''$.

We also carried out a short multicolour monitoring program of Mrk 79, NGC 4051 and NGC 4593 in the SDSS-u, Bessell-B, Bessell-V, Bessell-R and SDSS-i filter bands on the Faulkes Telescope North (FT) between 2007 February and May. The telescope is situated at the Las Cumbres Observatory, Haleakala, Maui, Hawaii, and is identical in specification and design to the Liverpool Telescope. The data from the optical camera, HawkCam, were reduced and analysed in exactly the same way as for the LT RATCam.

The fully robotic, unattended operation of these telescopes makes them ideal for the kind of observations required for this study. We needed regular, continuous monitoring over time-scales of several years to probe the wide range of variability time-scales displayed by AGN, which would be very intensive on a user-operated telescope.

2.2.2 Photometry

2.2.2.1 Aperture vs. PSF photometry

When light from a point source, such as a star, passes through the atmosphere and through the telescope's optics, it is spread out into a broad profile, known as a "point spread function" (PSF). All the stars in the image are point sources to the telescope and their light passes through essentially the same part of the atmosphere, so the shape of the light profile will be essentially the same for all the stars in the field of view. The PSF can generally be well described by an analytic function. The Moffat function (Moffat, 1969) is commonly used, as its broad wings describe the effect of atmospheric seeing better than a simple Gaussian or Lorentzian shape. It has the form

$$I(r) = \frac{I_c}{[1 + (r/r_d)^2]^{\beta}}, \tag{2.1}$$

where I is the intensity in counts, I_c is the peak intensity value and r the radius measured from the peak. r_d and β are the parameters varied for the fit, and determine the full width at half maximum (FWHM) and the wings of the profile. For the special case $\beta = 1$ the function becomes a Lorentzian. The best-fit parameters describing the PSF can be determined from the radial profiles of the brightest stars in the field of view and then scaled to the appropriate brightness of the other stars. Integrating the scaled function gives the total flux in the stellar profile. This is particularly useful in crowded fields, where the wings of adjacent or unresolved stars can blend into each other.

Even though the galaxy nucleus is unresolved, the stellar PSF is generally not a good description of the nuclear brightness profile, due to the underlying host galaxy flux. This is especially true when the host galaxy has a bright bulge. Figure 2.3a shows the brightness surface profile of NGC 4593 as an illustration. The nuclear emission is clearly visible as a sharp peak, and the bright bulge of the galaxy appears as broad wings or a “pedestal” in the brightness profile. A radially averaged two-dimensional profile of the same galaxy is plotted in part *b* of the figure, with the derived PSF fitted to one of the comparison stars shown as an insert. The Moffat function describes the shape of the stellar profile very well, but it cannot account for the host galaxy flux in the broad wings of the galaxy profile. As will be discussed in the next section, variable seeing conditions and the absence of bright stars from which the PSF may be accurately determined, will allow variable amounts of the host galaxy flux to be included in the measurement, leading to a systematic error in the AGN flux measurement.

In our sample, this effect is most clearly seen in NGC 4593 and NGC 5548. The other galaxies appear to have brighter nuclei relative to their bulges and do not show such bright, broad wings in the surface profile. However, in only one case (NGC 3227) did the derived PSF provide an acceptable fit to the nucleus; for all the other galaxies there was a significant amount of excess flux in the wings of the profile that could not be included by the PSF. For this reason, I decided to perform aperture photometry on all the targets.

2.2.2.2 Aperture size

For stellar photometry it is generally advised (e.g. Howell, 2006) to use a small aperture to reduce the amount of background noise included in the measurement. A typical aperture radius suggested is about the FWHM of the stars in the image. A large aperture including more of the background sky, leads to an increase in the noise and hence a reduction of the signal-to-noise of the measurement.

For AGN photometry however, such a small aperture should *not* be used, as it can lead to spurious variability in the light curve due to varying image quality.

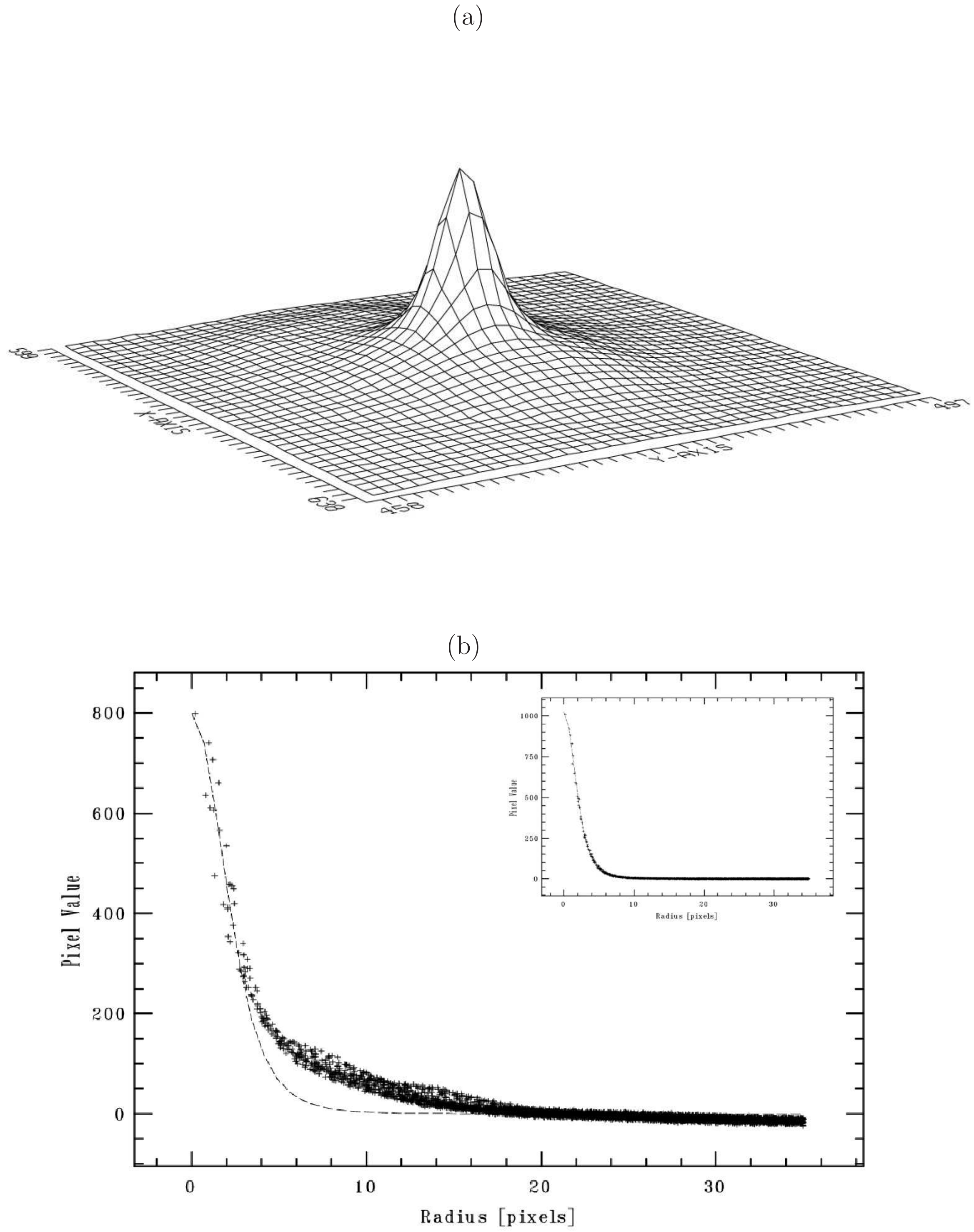

Figure 2.3: (a) Surface brightness profile of NGC 4593. The bright pedestal of the galaxy bulge is clearly visible. (b) The stellar PSF (dashed line) fitted to the average radial brightness profile of the NGC 4593 nucleus. The PSF fitted to a star in the field of view is shown as an insert, for comparison.

Even though the nucleus is much brighter than the host galaxy and the peak of the emission clearly visible, there is a significant amount flux from the host galaxy included in the aperture. Under poor seeing conditions, the light is spread out and the PSF becomes broader, but the extended light profile of the host galaxy is affected less than the peaked profile of the bright nucleus and the comparison stars. Hence relatively more light is lost from the comparison star aperture than from the galaxy aperture, so that the AGN flux measurement is systematically higher than that of the comparison stars. The problem clearly gets worse the poorer the seeing, or smaller the aperture, is. The method of using an aperture size varying with the FWHM, suffers the same problem, as varying amounts of host galaxy flux is included in the aperture.

The optimum aperture size is therefore a compromise between an increase in the random noise for a large aperture, and the image quality dependent systematic error which may arise as a result of using a small aperture. It therefore also depends on the object observed and on the typical conditions at the observing site.

2.2.2.3 Rejection criteria

As a compromise, I defined a set of rejection criteria, based on the image quality of the data set as a whole and then defined an appropriate aperture for the remaining images. To increase the time coverage of our observations, we asked for our targets to be observed even at bright moon conditions and into high airmass. As may be expected, at the most extreme of these conditions, the data became unreliable and had to be discarded.

I rejected all images which satisfied one or more of the following criteria:

- Images on which the nucleus (and sometimes a comparison star) were saturated (fits header keyword L1SAT = TRUE)
- Images taken under seeing conditions of worse than $3''$ (keyword SEEING > 10.7 pixels)
- Images taken at full moon (keyword MOONFRAC > 0.99)
- Images taken at very high airmass (keyword AIRMASS > 2.3)
- Images with an anomalously high background (keyword BACKGRD > 800); the typical background is $\sim$200–300 counts

The AGN was the brightest object in all our frames, except for a few of the NGC 4051 images, which included a bright star to the southwest of the galaxy. This star was not used as a comparison star, so images on which it was saturated, but not the nucleus of NGC 4051, were not discarded, unless it met one of the other rejection criteria.

The typical seeing of our Liverpool Telescope images is $1.4''$–$1.8''$. Only once in every ∼20 observations, on average, is the seeing worse than $3''$, so this value was set as the rejection limit. I used a $6''$ radius ($12''$ diameter) aperture for the photometry of the remaining images. The exception is NGC 4593, which has a much broader radial flux profile than the other targets, due to the bright bulge. For this AGN it was necessary to increase the aperture to $18''$ diameter to include the bulge and avoid a systematic error in poor seeing conditions.

In total, after applying all of these rejection criteria, I had discarded roughly 15% of the data we received from the LT pipeline.

2.2.2.4 Flux calibration and errors

I used the IRAF[3] package DAOPHOT to sum the flux inside the $12''$ ($18''$ in the case of NGC 4593) diameter aperture, centred on the nucleus.

In order to exclude galaxy flux from the background measurement, I did not use an annulus as is normally done in stellar photometry. A small amount of galaxy flux in the background annulus would not affect the variability, as long as it is constant, but it will affect the flux calibration relative to the comparison stars. Also, as the pointing with the LT was initially not very stable, the field of view common to all images was rather small, which would require taking such an annulus quite close to the nucleus to avoid it going off the edge of the chip. It would therefore include a substantial amount of galaxy flux in the background measurement. Instead, I averaged the background measured in 3–4 “blank sky” positions around each galaxy. (See Figure 2.2.) By aligning all images to a common reference image before measuring the background I could ensure that the same sky positions were measured in each image.

Each flux measurement was calibrated relative to up to four comparison stars in the field and then the fluxes calculated using the comparison star magnitudes of Doroshenko et al. (2005a,b) and Mihov and Slavcheva-Mihova (2008). The flux

---

[3] IRAF is distributed by the National Optical Astronomy Observatories, which are operated by the Association of Universities for Research in Astronomy, Inc., under cooperative agreement with the National Science Foundation.

error was calculated using the standard prescription (e.g. Howell, 2006), based on photon statistics and the readout noise of the detector. It is given by

$$\text{err} = \sqrt{\frac{\text{flux}}{\text{gain}} + A\sigma^2 + \frac{A^2\sigma^2}{n}}, \tag{2.2}$$

where 'flux' is the background-subtracted counts, 'gain' the gain of the readout electronics of the telescope, A the area enclosed by the aperture, σ the standard deviation of the background counts and n the number of pixels in the background sky measurement. The error is calculated for each star and then propagated to give the error on the galaxy flux.

Finally, I plotted the measured fluxes against the seeing to ensure that there is no correlation between the two quantities. A correlation between the seeing and the measured fluxes would imply that the variability may be artificially introduced by the variation in image quality from frame to frame. No such correlation was found.

2.2.2.5 Photometry of Mrk 110

Mrk 110 appears pointlike in our images; the host galaxy is not visible (see Figure 2.2). However, there is a foreground star at R.A. 09h 25m 13.2s, Dec. $+52°17'14''$ (2000.0), which blends into the galaxy profile on most of our images. I modeled the PSF from suitable stars in the field and subtracted this star from each image, before performing aperture photometry directly on the subtracted images. As the host galaxy is not visible, I could also use a smaller aperture than for the other targets in the sample. $8.3''$ diameter was found to be suitable, and the background was calculated in an annulus of inner and outer diameter $13.5''$ and $18.9''$, respectively.

2.2.3 Optical data from other telescopes

For some of the targets we also obtained data from collaborators, notably Sergey Sergeev, from the Crimean Astrophysical Observatory (CrAO), and Takeo Minezaki, from the MAGNUM group (Multicolor Active Galactic Nuclei Monitoring project, Yoshii et al., 2003) at the University of Tokyo. Where I have used their light curves in combination with the LT/FT data described in the previous sections, this will be stated clearly.

The filter set of the camera mounted on the Crimean Observatory Telescope,

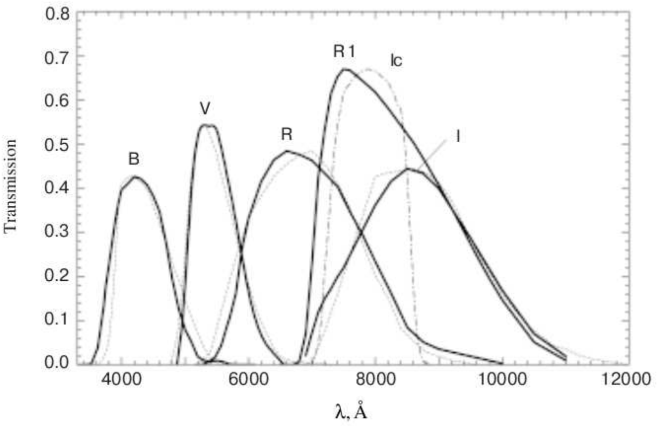

Figure 2.4: Comparison between the transmission curves of the non-standard filter set on the CrAO telescope and the standard Johnson filters. (*Figure from* Doroshenko et al. 2005a)

consists of non-standard filters, but their B, V, R and I filters are close to the Johnson/Bessell filters and their $R1$ filter is similar to the Cousins I filter (see Doroshenko et al., 2005a). Figure 2.4 shows the difference between their filter transmission curves and the standard Johnson passbands.

Also, the data taken at different observatories may have slight differences in the calibration and also in the aperture that was used to construct the light curves, adding different amounts of host galaxy starlight to the nuclear flux measurement. In order to take account of these differences when combining two light curves, I extracted pairs of observations which were taken within one day of each other, from overlapping light curves and performed a least-squares fit of the equation

$$F_1 = aF_2 + b \tag{2.3}$$

to the flux pairs. F_1 and F_2 are the flux measurements from the two datasets and a and b the parameters of the fit. I weighted the points by the inverse of the time difference between F_1 and F_2, so that measurements made closer together in time have a greater influence on the fit. The best-fit parameters from each pair of overlapping light curves were then used to scale that dataset to the chosen reference data set.

2.2.4 Difference Imaging

Difference imaging is a powerful method developed for detecting variable stars in a crowded field. I believe the method holds great potential for AGN optical variability studies, but unfortunately our dataset was not well suited to be analysed this way. I will briefly discuss the reasons for this, along with a short introduction to the method, as a reference.

The difference imaging technique aims to match the seeing between two images to allow them to be optimally subtracted, leaving only the variable part of the flux in the image. The specific implementation of the technique I used, was developed by Alard and Lupton (1998) and extended by Alard (2000).

Their method, called ISIS, relies on least squares fitting to calculate a convolution kernel $\mathrm{Ker}(x, y)$ (i.e. a PSF model) between a high-quality reference image $\mathrm{Ref}(x, y)$ and another image in the sequence $\mathrm{Im}(x, y)$, such that

$$\mathrm{Im}(x, y) = \mathrm{Ker}(x, y) \otimes \mathrm{Ref}(x, y) + \mathrm{Bgd}(x, y) \tag{2.4}$$

where the symbol $\otimes$ represents the convolution product. The term $\mathrm{Bgd}(x, y)$ allows for differential background subtraction between the different images in the sequence. It is essential that the reference image used to construct the PSF model is of very high quality, i.e. good seeing, low background and high signal-to-noise. In practice, it is often better to use a stacked image to achieve good signal-to-noise, even though this reduces the effective seeing.

In their solution of this problem Alard and Lupton (1998) decompose the PSF model into three Gaussian basis functions, each modified by an associated polynomial. This type of function was selected for its properties of having a finite sum and decreasing fast after a certain distance (the 'edge' of the star on the image). The decomposition allows them to model even a PSF with very complicated shape simply, which has obvious advantages in terms of computing time.

The calculation of the PSF model relies on the fact that most of the stars in the image are non-variable, hence the difference between corresponding pixels on co-aligned images are mostly due to variations in the seeing. Each image in the series is then subtracted from the reference image, convolved with the PSF model, to produce a series of difference images. All the flux which is constant in the series of images is therefore subtracted, leaving only the variable part of the flux on the difference image and allows high precision relative photometry to be done directly on the difference images.

Clearly, this will be very useful for AGN photometry, where the variable nuclear flux is substantially contaminated by the constant host galaxy flux.

However, obtaining a good model PSF relies heavily upon being able to obtain a good sampling of the image seeing (i.e. the stellar PSF), and ISIS does this by sampling every pixel in the image. Hence in crowded fields, for which the method was developed, every star provides information about the PSF, and the method performs at its best. This assumption limits somewhat the efficiency of the method in uncrowded fields such as ours, but a solution should still be possible, provided that there are a few bright stars in the image from which the PSF can be determined.

Before images can be subtracted from each other, they have to be aligned to a common coordinate grid. These tasks within the ISIS package can only deal with very small relative shifts and are optimised for a crowded field. For large shifts and rotations, as we had with the LT images, it is much better to use the IRAF tasks XYXYMATCH, GEOMAP and GEOTRAN, or similar. Clearly, the sharp changes and edge effects introduced by the rotation have to be removed in order to calculate the model. Unfortunately, the shifts and rotations in the LT images (especially the earlier half of the data) are so large that cutting all images to the area common to all images, left only a ∼quarter of the original field of view, with no or only a few faint stars to calculate the PSF from. An example image is shown in Figure 2.5. The unavailability of suitable PSF stars resulted in a poor PSF model and hence poorly subtracted difference images, giving unreliable photometry results.

For this reason, I had to use the more conventional aperture photometry methods described in the previous section, to construct the optical light curves used in this study. These measurements include a significant contribution of host galaxy flux in the aperture, so this had to be accounted for separately. I did this by fitting standard galaxy light profile models to the images to estimate the host galaxy flux included in the aperture. The technique and results will be discussed in more detail in Chapters 4 and 5.

Nevertheless, difference imaging has been successfully applied in the search for classical novae in nearby galaxies (Darnley et al., 2007) and well as gravitational lensing observations (Woźniak et al., 2000) in similar uncrowded fields. For larger fields of view, or a sequence of images with a larger area common to all frames, this is potentially a very powerful technique, as it effectively eliminates the host galaxy contamination and reveals the true nuclear variability amplitude.

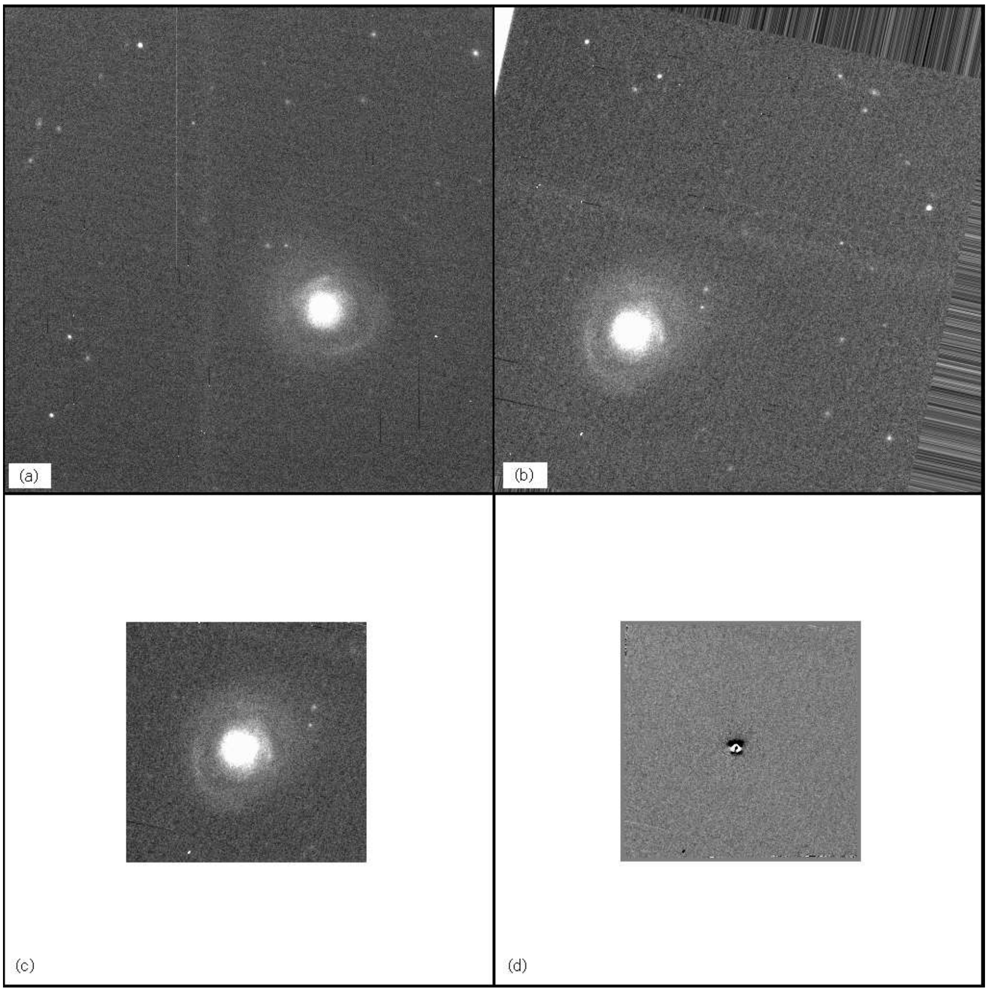

Figure 2.5: Example images illustrating the difference imaging process described in the text. (a) A flat-fielded, bias subtracted image of NGC 5548 as obtained from the Liverpool Telescope data pipeline. (b) Bad column removed, rotated and aligned to the reference image. (c) In order to do the difference imaging, the edge effects introduced by the rotation must be taken out, and all images must be cut to the same size. Large differences in the orientation of images taken over a long time, reduce the usable part of the image significantly. (d) The result of subtracting the reference image, convolved with the kernel, from the image in panel c. Note that the host galaxy flux, as well as the two faint stars close to the galaxy, visible in all the other panels, are subtracted to within the residual noise of the difference image.

3 A high mass example: Mrk 79

The work in this chapter was published as:
Breedt, E.; Arévalo, P.; M^{c}Hardy, I. M.; Uttley, P.; Sergeev, S. G.; Minezaki, T.; Yoshii, Y.; Gaskell, C. M.; Cackett, E. M.; Horne, K. and Koshida, S., 2009, *MNRAS*, 394, 427

3.1 Introduction

As a first step in investigating the connection between the X-ray and optical variations in Seyfert galaxies, I present in this chapter a detailed analysis of the X-ray and optical light curves of Markarian 79 (UGC 3973, MCG+08–14–033). It is a well-known X-ray source and its optical variability is well established (Peterson et al., 1998a; Webb and Malkan, 2000).

Mrk 79 is a nearby ($z = 0.022$) Seyfert 1.2 galaxy with a black hole mass of $(5.24 \pm 1.44) \times 10^{7} M_{\odot}$ (Peterson et al., 2004) and an average fractional accretion rate $\dot{m} = \dot{M}/\dot{M}_{\rm Edd}$ of $\sim 6\%$ (Kaspi et al., 2000).

On short to medium time-scales (days to a few tens of days) the 2–10 keV X-ray and optical u and V band fluxes are found to be significantly correlated, with a delay between the bands consistent with zero days. Most of these variations may be well reproduced by a model where the short-term optical variations originate from reprocessing of X-rays by an optically thick accretion disc. The optical light curves, however, also display long time-scale variations over thousands of days, which are not present in the X-ray light curve. These optical variations must originate from an independent variability mechanism and I show that they can be produced by variations in the (geometrically) thin disc accretion rate as well as by varying reprocessed fractions through changes in the location of the X-ray corona.

3.2 Data

3.2.1 X-ray observations

As described in Chapter 2, we used the Proportional Counter Array (PCA) on board *RXTE* to obtain a long term X-ray light curve of Mrk 79. From 2003 March 23 to 2008 January 30, we observed the galaxy at approximately two day intervals. During a period of intensive monitoring, 2005 November 17 to 2006 January 19, four observations per day were made. The X-ray light curve was constructed (by P. Uttley) by fitting a power law model to each of the observed spectra, and integrating the flux in the range 2–10 keV. It shown in Figure 3.1, smoothed with a 4 point (approximately 8 day) running average to show the variations on time-scales of days more clearly. However, the unsmoothed light curve was used in all calculations.

3.2.2 Optical observations

Since 2002, Mrk 79 has been monitored independently by several ground-based observatories. I combined the data from six different telescopes here to construct an optical light curve spanning more than 5 years. A summary of these observations may be found in Table 3.1 and each is discussed briefly below.

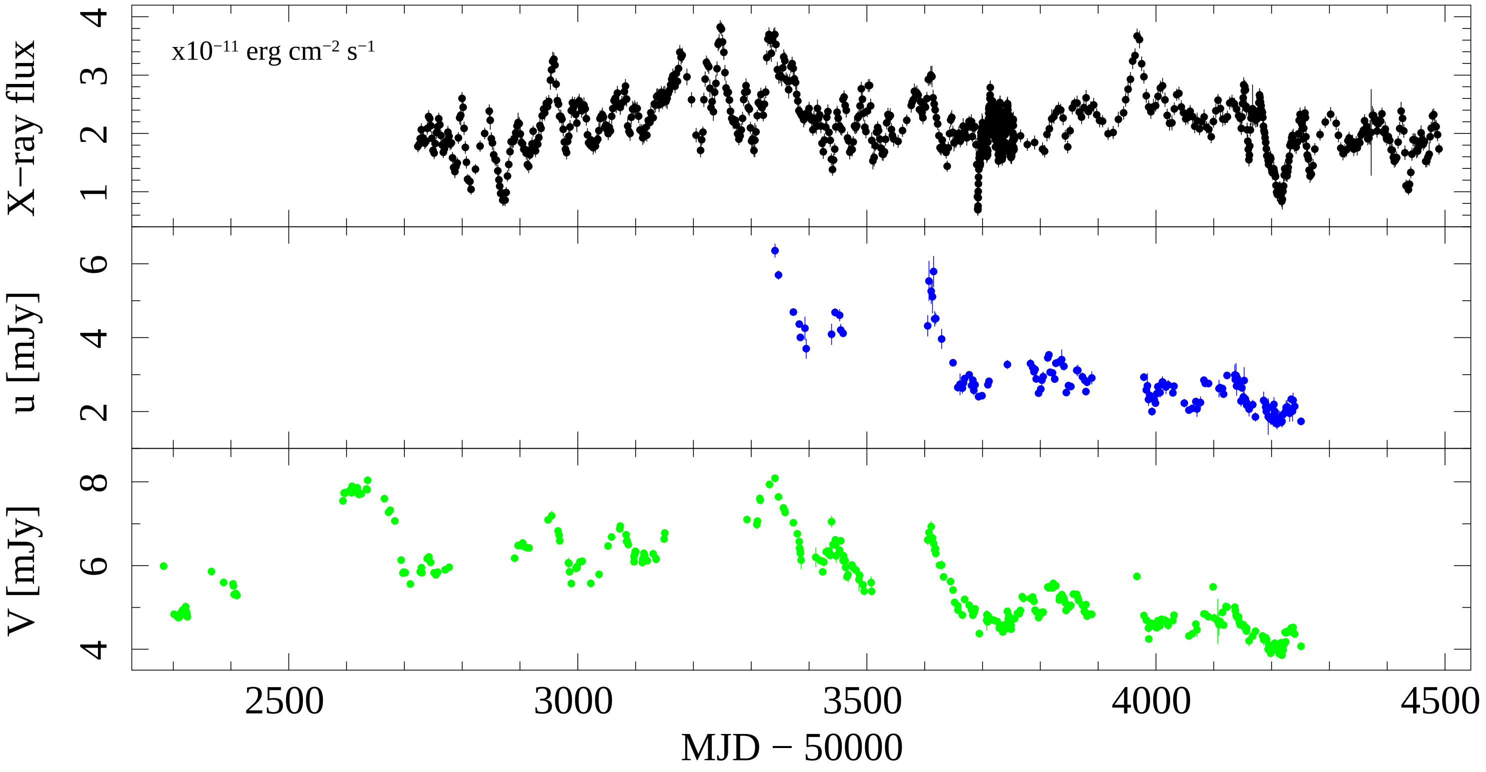

Figure 3.1: $2-10$ keV X-ray (top panel), u (middle panel) and V band (bottom panel) light curves of Mrk 79. The X-ray light curve is smoothed with a 4 point (∼8 day) boxcar, to highlight the variations on time-scales similar to that of the optical light curves. The X-ray light curve is in units of 10^{-11} erg s^{-1} cm^{-2}, the optical light curves are in mJy. The u band flux is scaled to a comparison star in the field but no colour correction has been applied. V flux calculated as described in the text. No host galaxy contribution has been subtracted.

Table 3.1: Summary of the V band observations of Mrk 79

Observation dates (MJD)	Instrument and Telescope	Aperture diameter	No. of V band observations
52283.5 – 53987.6	AP7p camera, 0.7-m Crimean Observatory Telescope	15″	142
52890.6 – 53876.3	Multicolor Imaging Photometer, MAGNUM Telescope	8″.3	47
53100.6 – 54198.8	0.4-m telescope, Lincoln, Nebraska	16″	79
53341.0 – 54250.9	RATCam, Liverpool Telescope	12″	132
54063.4 – 54129.3	0.6-m telescope, Mt. Maidanak Observatory	16″	22
54136.3 – 54237.3	HawkCam, Faulkes Telescope North	12″	39

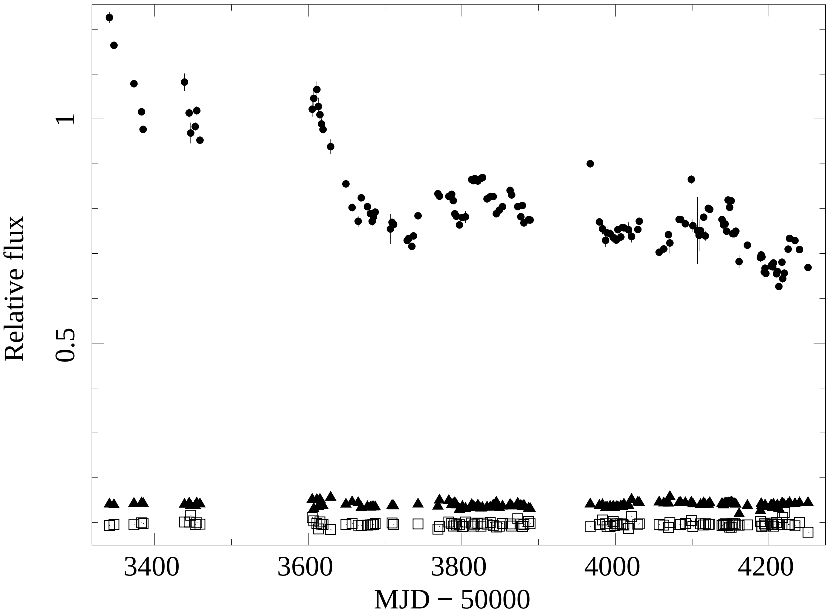

Figure 3.2: V band light curve of Mrk 79 as obtained with the Liverpool Telescope. The ratio of the comparison star to two check stars in the field is also shown, showing that the decrease in brightness of Mrk 79 is real and not due to a variable comparison star.

Liverpool Telescope

Mrk 79 is part of our ongoing optical monitoring programme on the Liverpool Telescope (LT). Observations in the SDSS-u and Bessell-V filter bands started on 2004 December 2 with a four day sampling period. This was increased in March 2007 to daily monitoring in V and every two days in u. The latest measurement in the light curve included here was taken on 2007 May 30.

As described in Chapter 2, I used a 12″ aperture, centred on the nucleus of the galaxy, to do the photometry and construct the light curves. The V band light curve from the LT is shown in Figure 3.2. Mrk 79 showed a steady decline in brightness over the period of monitoring. The light curve is plotted relative to two comparison stars, to show that this decrease in brightness is real and not due to a variable comparison star: the variation of the comparison stars around their respective means is less than 1%, while Mrk 79 varies by 14%.

Faulkes Telescope

We also carried out a short multicolour monitoring program in u,B,V,R and i on the Faulkes Telescope North (Haleakala, Maui, Hawaii) from 2007 February 5 to May 17. The telescope and camera are identical in specification and design to the

Liverpool Telescope and data were reduced and analysed in the same way. The sampling is roughly every two days, with some gaps due to poor weather conditions. 33 useful epochs in u, 35 in B, 39 in V, 36 in R and 27 in i were obtained. The light curves are shown in Figure 3.3.

Crimean Observatory Telescope

We supplement these light curves with V band data from the AGN monitoring program on the 0.7-m telescope of the Crimean Astrophysical Observatory, described in Sergeev et al. (2005). The $B, V, R, R1, I$ filter set on the AP7p camera mounted on this telescope are nonstandard filters, though the V filter, from which I include data here, matches the standard Bessell-V filter closely (see Figure 2.4). The light curve was constructed (by S. Sergeev) from aperture photometry through a $15''$ diameter aperture centred on the galaxy nucleus, relative to a comparison star in the field. It covers the period 2002 January 9 – 2006 September 9 and has a sampling rate of roughly every two days. Data after MJD 53058 (2004 January 18) from this program were previously unpublished.

MAGNUM Telescope

We also include unpublished data from the MAGNUM (Multicolor Active Galactic Nuclei Monitoring) project (Yoshii et al., 2003). The 2 metre telescope is situated at the University of Hawaii's Haleakala Observatory, on the island of Maui, Hawaii, and monitors a large sample of AGN in optical and infrared wavebands. The V band light curve included here are the observations made during the period 2003 September 8 – 2006 May 2. These observations were reduced by S. Koshida, using a $8\overset{''}{.}3$ diameter aperture to measure the nuclear flux, relative to a nearby star. Comparison stars were calibrated against photometric standard stars and colour corrections applied to the fluxes. Full details of the data acquisition and reduction are described in Suganuma et al. (2006).

0.6-m telescope, Mt. Maidanak

Mrk 79 was also observed with the 0.6-m telescope at the Mt. Maidanak Observatory, Uzbekistan from 2006 November 24 to 2007 January 29. Aperture photometry was performed on these data using a $16''$ diameter aperture and a background annulus between $24 - 40''$. The measurements were calibrated using the Doroshenko et al. (2005a) comparison star magnitudes.

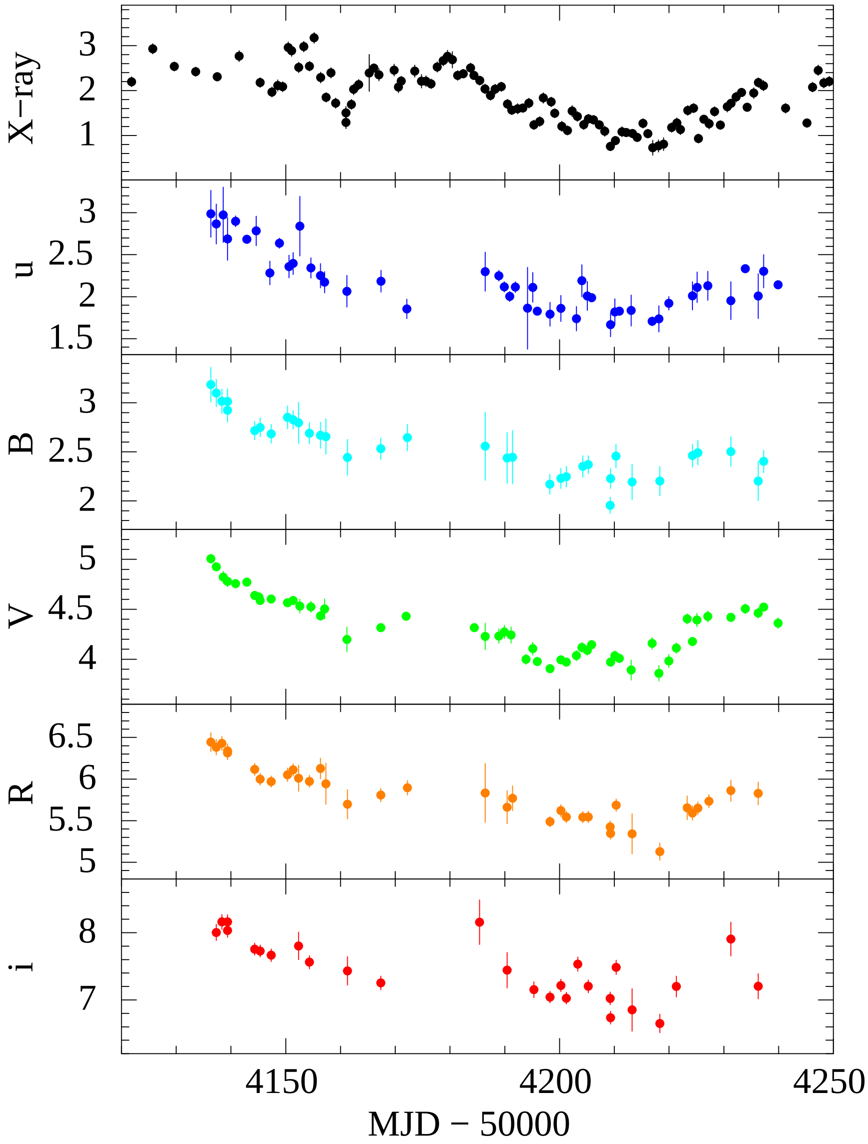

Figure 3.3: *uBVRi* light curves of Mrk 79 as obtained with the Faulkes Telescope, shown with the corresponding section of the X-ray light curve. The X-ray light curve is in units of 10^{-11} erg s^{-1} cm^{-2}, the optical light curves are in mJy.

0.4-m telescope, Lincoln, Nebraska

Finally, I include V band CCD observations obtained with the 0.4-m telescope of the University of Nebraska, contributed by M. Gaskell. Details of these observations and reduction procedures are as given in Klimek et al. (2004). The photometric aperture, sky annulus, and comparison stars were as for the Mt. Maidanak observations.

3.2.2.1 Relative calibration

In order to account for the differences in the calibration and photometry aperture with which the individual light curves were constructed, I selected the MAGNUM flux calibrated light curve as the reference dataset and scaled all the other light curves to match it. I extracted pairs of measurements from overlapping light curves, taken within one day of each other, from overlapping light curves, and performed a least-squares fit of the equation $F_1 = aF_2 + b$ to the flux pairs, where F_1 and F_2 are the flux measurements from the two datasets and a and b the parameters of the fit. The best-fit parameters from each pair of overlapping light curves were then used to scale that dataset to the $8''.3$ diameter aperture MAGNUM light curve.

The total combined V band light curve spans 1967 days (approximately 5 years and 5 months) and contains 461 epochs. It is shown in Figure 3.1 along with the X-ray and u band light curves. Throughout the rest of this chapter and in Chapter 5, I will use this combined light curve to refer to the V band light curve of Mrk 79.

3.2.3 Variability properties and host galaxy flux

The flux measured within the aperture contains the nuclear flux as well as starlight from the part of the host galaxy falling inside the aperture. This host galaxy flux is a constant contribution to the total measured flux, so although it does not affect the results of the cross-correlation analysis (Section 3.3), it dilutes the variability of the nucleus. I estimate the host galaxy contribution as follows. I obtained an archival *HST* image of Mrk 79 from the online MAST archive, taken on 2006 November 8 (MJD 54048) with the Advanced Camera for Surveys through the F550M filter. This is a medium width continuum V band filter, centred on 5580Å with a FWHM of approximately 540Å. I compared the flux measured through an $8''.3$ aperture (to match the total V band light curve) with the flux measured through a $0''.25$ aperture centered on the nucleus. I measured a 43.5% nuclear contribution to the total optical emission in the $8''.3$ aperture. I linearly interpolated the V band light curve to estimate the flux at the time of the *HST* observation and took 56.5% of this value to be the host galaxy contribution. This equated to a 2.54 mJy correction, which was subtracted from the whole V band light curve for the purposes of the variability calculations below. No colour correction factor has been applied to transform this flux to the flux through the broader Bessell-V filter. However, assuming the spectrum to be flat over the width of the filter, the correction to the flux ratio as calculated here, will be very small.[1]

In order to compare the amount of intrinsic variability in each light curve I calculated the error-corrected flux variance, as a fraction of the mean flux. This quantity is known as the fractional variability,

$$F_{\rm var} = \frac{\sqrt{\sigma^2 - \varepsilon^2}}{\langle f \rangle} \, , \tag{3.1}$$

where the flux variance has the standard definition

$$\sigma^2 = \frac{1}{N} \sum_{i=1}^{N} (f_i - \langle f \rangle)^2 \tag{3.2}$$

and ε^2 is the sum of the squared measurement errors

$$\varepsilon^2 = \frac{1}{N} \sum_{i=1}^{N} \varepsilon_i^2 . \tag{3.3}$$

The sampling statistics and variability properties of each light curve are summarised in Table 3.2.

The X-ray and total optical light curves are both highly variable. The unsmoothed X-ray light curve contains much more variability power at high frequencies than the optical light curve, but due to the large amplitude of the long term optical variations, there is more variability power in the optical light curve when corrected for host galaxy flux. In the much shorter Faulkes Telescope colour light curves, the fractional variability is seen to decrease with wavelength. If the variability is intrinsic to the accretion disc, this behaviour is expected, as the longer wavelength emission originates from further out in the disc, where the natural time-scales are longer. This is also expected from reprocessing models: the disc response function broadens for longer wavelengths, smoothing out the variability

---

[1] A subsequent estimate, using V band data from the LT, yielded 2.60 mJy (see Section 5.2.2).

Table 3.2: Sampling and variability characteristics of the Mrk 79 light curves

Light curve	Total length (d)	N	$\Delta t_{\rm median}$ (d)	$F_{\rm var}$(%)	$f_{\rm max}/f_{\rm min}$
X-ray	1775	975	1.89	27.33	10.50
u (total)	910	143	2.47	31.07	3.81
V (total)	1967	461	1.63	35.92[a]	5.04[a]
Multicolour monitoring:					
u	103	47	1.75	14.32	1.79
B	101	35	2.00	9.68	1.63
V	103	51	1.73	6.53	1.30
R	100	36	2.00	5.04	1.26
i	99	27	2.93	5.44	1.23

[a] Host galaxy flux subtracted.

at longer wavelengths (see, e.g. Cackett et al., 2007). Note, however, that no correction for host galaxy flux has been made to these light curves, so the variability amplitude is reduced by this constant offset. Thus the fractional variability quoted in Table 3.2 should be viewed as a lower limit.

3.3 Cross-correlation analysis

3.3.1 X-ray – optical correlation

In order to confirm and quantify the apparent correlation between the X-ray and optical emission, I use the Discrete Correlation Function (DCF) method of Edelson and Krolik (1988).

I cross-correlate the unsmoothed, unbinned X-ray light curve with the observed u and V band light curves and then bin the resulting discrete correlation function in uniform lag bins. Here, and throughout this thesis, a positive value on the lag axis indicates a lag of the longer wavelength emission behind the shorter wavelength (i.e. a lag of the optical variations behind the X-rays, in this case).

To account for the ∼100-day long solar conjunction gaps in the optical light curves, I divide the light curves into segments defined by these observation gaps, and calculate the DCF for each segment separately. As the strength of the correlation may be different on different time-scales, I resample the X-ray light curve to a uniform observational frequency by selecting only one point every two days from the intensively sampled period starting just before MJD 53700. This ensures that this segment does not dominate the combined correlation function. The final correlation function is then the combination of the individual DCFs, weighted by the number of points in each lag bin. The DCFs calculated this way, using a bin size of 4 days, are shown in Figure 3.4.

The effect of calculating the DCF in segments like this is to implicitly remove the low frequency power (i.e. long term trends) in the light curve, leading to an improved estimate of the short-term lag. The most common way of removing this low frequency power is to subtract a low-order polynomial function from the light curve prior to calculating the CCF (Welsh, 1999). I prefer the method of segmentation of the light curve, however, as it also eliminates the large observation gaps from the DCF calculation. Note, however, that removing a linear trend or a higher order polynomial from the light curve also results in a correlation peak of greater than 99% significance, as discussed below.

The correlation function peaks at $\mathrm{DCF}_{\mathrm{max}} = 0.496$ for the X-ray/V band correlation and at $\mathrm{DCF}_{\mathrm{max}} = 0.654$ between the X-rays and u band, with no lag between the optical bands and the X-rays. The DCF peak occurs at 0^{+4}_{-4} days for V and 0^{+4}_{-4} days for the u band. (Note that, because the DCF was used, these errors will always be a multiple of the bin size.) The peak of the correlation function is thought to provide the most reliable estimate of the lag (Welsh, 1999), however, when using the DCF, time resolution on time-scales shorter than the bin size is lost, so the peak position is affected by the chosen DCF binning factor. I therefore deem the measurement of the centroid lag more reliable and stable in this case. The centroid is calculated as the weighted average of all DCF points greater than 80% of $\mathrm{DCF}_{\mathrm{max}}$. For the X-ray/$V$-band correlation, the centroid lag occurs at $0.00^{+1.91}_{-4.00}$ days and for the X-ray/u-band at $-1.95^{+1.95}_{-3.89}$ days. The errors quoted are the 1 σ errors calculated using the Flux Randomisation/Random Subset Selection (FR/RSS) method of Peterson et al. (1998b) and the centroids are the median centroids from 1000 such selections.

As a separate check, I also used the z-transformed discrete correlation function (zDCF) of Alexander (1997) and the interpolation cross-correlation function (ICCF; Gaskell and Sparke, 1986; White and Peterson, 1994) to calculate the same correlation. The correlation functions resemble those calculated using the DCF closely and the lag results are consistent between the three methods. (The correlation calculated using the ICCF is shown in Section 5.4.) The short lags obtained

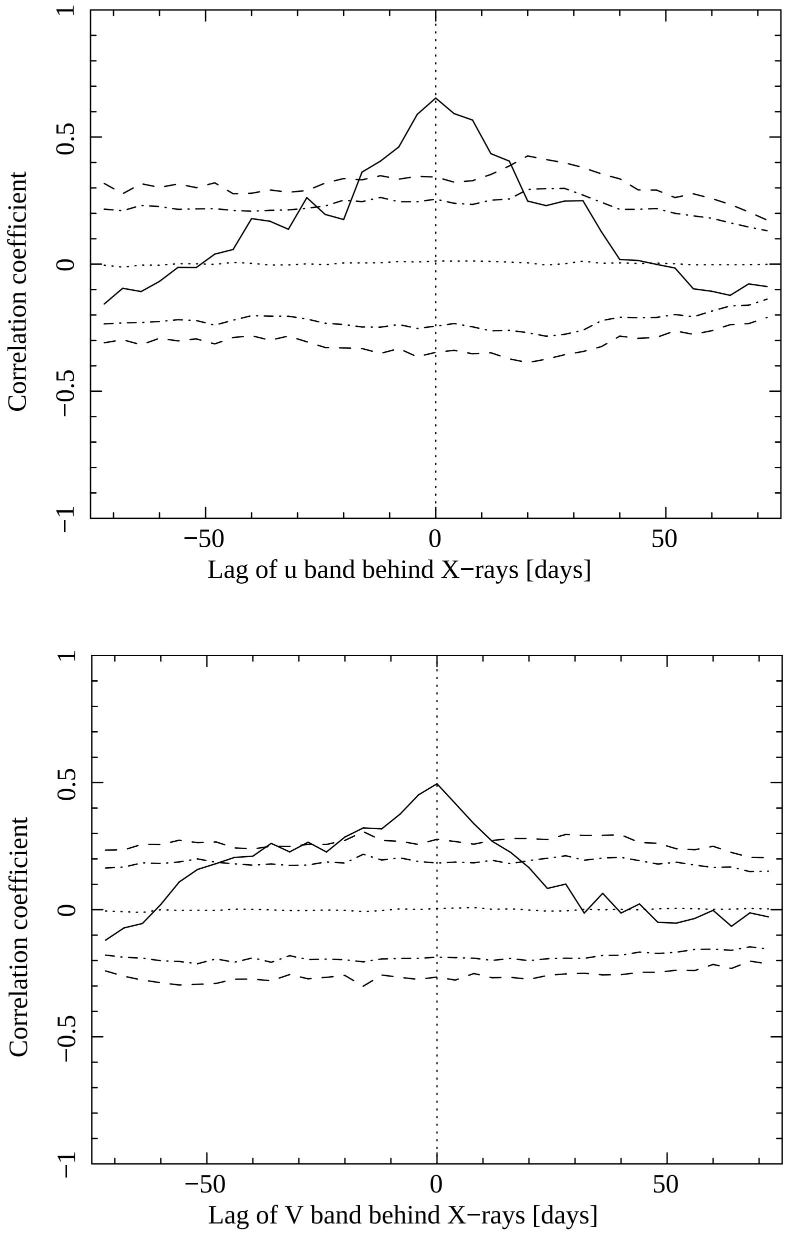

Figure 3.4: DCFs between the X-ray and u band (top) and X-ray and V band (bottom), binned in 4 day lag bins. The horizontal dotted, dash-dot and dashed lines are the median, 95% and 99% confidence levels, based on 1000 simulations. The vertical dotted line indicates the zero lag position.

from both the peak and the centroid measurements suggest that the reprocessor must be located near the X-ray source in this object, and not, for example, as far out as the dust torus.

To test the significance of the DCF peaks found, I used the method of Timmer and Koenig (1995) to simulate X-ray light curves based on an underlying model power spectrum. I used the single-bend power law parameters, as measured by Summons (2008), appropriate for the power spectrum of Mrk 79. To account for long term trends in the data, the simulated light curves were generated 10 times longer than the real light curve, and then sampled in the same way as the observed X-ray light curve. Observational noise was added at the level measured in the observed light curve. These uncorrelated, simulated X-ray light curves were then each cross-correlated with the real, observed optical light curve, to estimate the probability of obtaining equal or higher correlation peaks by chance, due to the red noise nature of the light curves. The mean, 95% and 99% extremes of 1000 such simulations are plotted in dotted, dot-dashed and dashed lines, respectively, in Figure 3.4. Both the u and the V band peaks reach higher than 99% of the simulations, showing that the correlations are statistically significant at greater than 99% level.

3.3.2 Lags between optical bands

I also present, in Figure 3.5, the zDCF between the X,u,B,R and i bands, calculated relative to the V band, for the data from the Faulkes Telescope. The u and V band light curves were supplemented with data from the Liverpool Telescope covering the same period. I chose the V band as reference light curve as it is the best sampled. The X-ray and V band autocorrelation functions (ACF) are also shown. Again a positive value on the lag axis represent a lag of the variations in the longer wavelength band behind those of the shorter wavelength. The interpolation cross-correlation function (ICCF; Gaskell and Sparke, 1986; White and Peterson, 1994) is used as a consistency check. It is plotted as a solid line in Figure 3.5 and is in close agreement with the zDCF results.

If the optical variations are due to reprocessing of X-rays by the accretion disc, standard accretion theory for a thin viscous disc allows us to calculate the lags expected between optical bands. In a standard accretion disc model (e.g. Frank et al., 2002), the disc can be approximated by annuli at different temperatures, each emitting a blackbody spectrum. The radial temperature profile of the disc

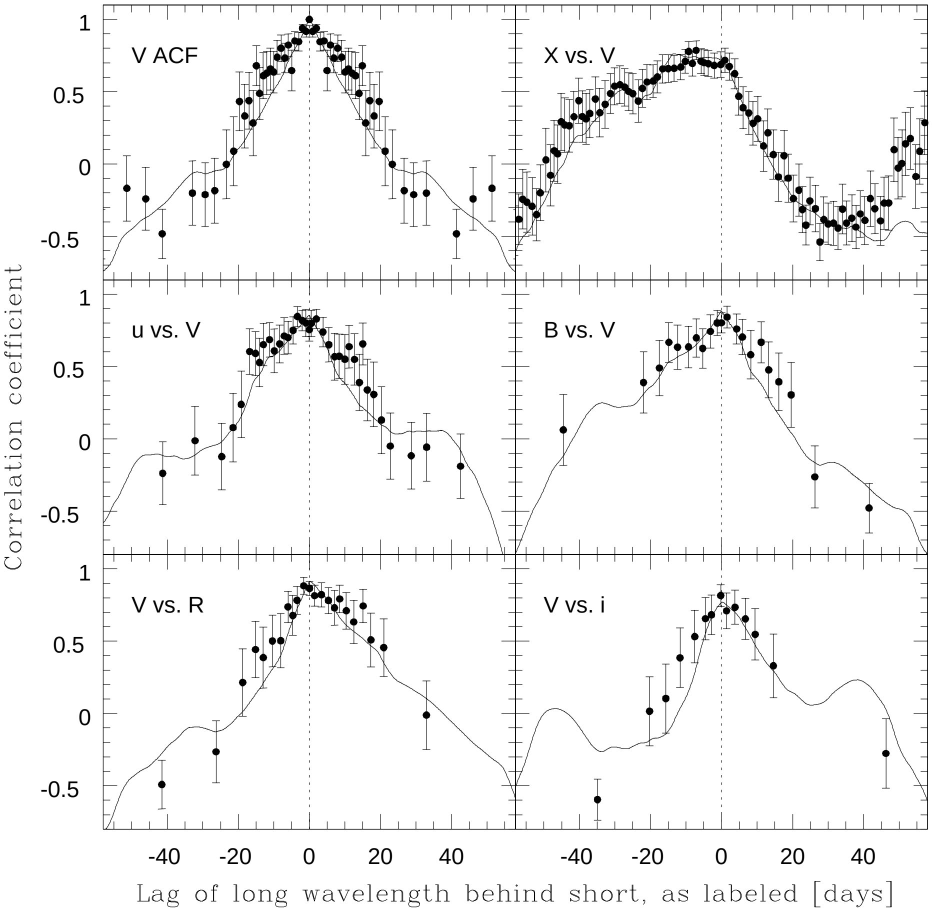

Figure 3.5: Cross-correlation functions relative to the *V* band, calculated from the 3 months of Faulkes monitoring. Points with error bars are calculated from the zDCF and the solid line from the ICCF. A positive value on the lag axis indicate a lag of the long wavelength emission behind the short wavelength. The vertical dotted lines show the position of zero lag.

may then be described by

$$T(r) = 3.8 \times 10^6 \left(\frac{\dot{M}}{\dot{M}_E}\right)^{\frac{1}{4}} \left(\frac{M}{10^6 M_\odot}\right)^{-\frac{1}{4}} \left(\frac{r}{R_g}\right)^{-\frac{3}{4}} \text{ K} \qquad (3.4)$$

where $R_g = GM/c^2$ is the gravitational radius of the black hole. Using Planck's Law to calculate the peak emission, one can use (3.4) to calculate the radius most of this emission is coming from. In the reprocessing model, delays should exist between different wavebands, due to light travel time differences between the illuminating source (assumed to be the X-rays) and the region of the disc emitting at the given wavelength (Collier et al., 1998). Hence variations observed at longer wavelengths should follow those at shorter wavelengths with a delay $\tau = r/c$, where r is the distance between the locations of peak emission for the relevant wavelengths. Using the reverberation mapping mass (Peterson et al., 2004) and accretion rate (Woo and Urry, 2002) of Mrk 79, and assuming the X-ray source to be a point source at height $h_X = 6R_g$ above the accretion disc and on its axis of symmetry, we expect a V lag of 1.68 days behind the X-rays and lags between the optical bands of u vs. $V = 0.74$, B vs. $V = 0.43$, V vs. $R = 0.64$ and V vs. $i = 0.85$ days.

Both figures 3.3 and 3.5 show that the variations in the optical bands are well correlated. The centroids of the correlation function, calculated at 80% of the peak, were found to be u vs. $V = -0.59^{+2.16}_{-1.92}$, B vs. $V = -0.58^{+2.03}_{-2.29}$, V vs. $R = 2.50^{+1.25}_{-1.61}$ and V vs. $i = 1.23^{+1.68}_{-1.49}$ days. All except the R band are consistent with the expected lags for reprocessing to within the 1-σ FRRSS errors. The discrepancy in the R band result is likely due to the strong, broad Hα emission line contained within the R filter passband. The Hα line emission originates in the broad line region, which is further from the X-ray source than the region of the disc emitting primarily at this wavelength. Hence Hα varies with a longer lag than the disc R band emission and increases the average lag measured in this band.

From this short segment of the data, the V band emission appears to lead the X-rays by ∼5 days (i.e. X vs. $V = -5.25^{+2.55}_{-7.66}$ days), which is not consistent with the reprocessing picture. I point out, however, that the error bars are overlapping with the X vs. V correlation measurement found in section 3.3.1. Since the sampling of these short light curves are not significantly better than the total V band light curve (see Table 3.2), I deem the previous result of an optical lag of $0.00^{+1.91}_{-4.00}$ days behind the X-rays more robust and reliable, as it was derived from light curves almost 20 times as long. In short sections of the light curve the long term variations (which are present in the optical light curve but not the X-rays) can influence the lag measured, especially if there are not many peaks or troughs in that segment to constrain the lag tightly. In the longer light curves, these small shifts average out and a more reliable estimate of the true lag is obtained.

3.4 Modelling reprocessing

A possible mechanism for the production of optical fluctuations is thermal reprocessing of variable X-rays shining on optically thick material, possibly the accretion disc. I constructed reprocessed optical light curves, using the observed X-ray light curve as input, to compare to the observed optical light curve. We assume that the X-rays are emitted by a compact source above the accretion disc and on its axis of symmetry while the optical flux arises thermally from an optically thick accretion disc. This geometry of the X-ray source may be viewed as a first order description of the centre of an X-ray corona above the inner part of the accretion disc. More realistic geometries, such as a spherical corona of radius h_X, will have a small effect on the flux calculated at the inner parts of the disc, but from further out in the disc, where most of the emission we are interested in is coming from, the corona will increasingly resemble a point source. This simplistic description is thus sufficient for our purposes here. I followed the prescription detailed by Kazanas and Nayakshin (2001) to account for light travel time effects on the reprocessed light curve, as well as geometrical considerations on the amount of flux received per unit area for different locations in the disc and X-ray source heights. The impinging X-ray flux was added to the locally dissipated flux expected for a thin disc, to calculate the black body temperature as a function of time and radius, in order to produce flux light curves in different optical bands.

The model parameters are the height of the X-ray source h_X, thin disc accretion rate $\dot{m}$, inclination angle to the observer i and inner truncation radius of the thin disc $R_{\rm in}$. The mass of the black hole determines the size of the gravitational radius and therefore the conversion of light crossing time to days. The mass was fixed at the reverberation-mapped value of $5.24 \times 10^7 M_\odot$ (Peterson et al., 2004). $R_{\rm in}$ and h_X varied between 6 and 50 R_g, where R_g is the gravitational radius $R_g = GM/c^2$. The inclination i was varied between 0 and 90° and $\dot{m}$ between 0.001 and 0.9 times the Eddington-limit accretion rate. A distance of 94.4 Mpc was used to convert between luminosities and observed fluxes. No correction for reddening or dust extinction has been made. The calculated reprocessed light curves were resampled to match the observation epochs of the corresponding optical light curves. I subtracted the 2.54 mJy galaxy contribution (section 3.2.3) to the V band flux before fitting the reprocessed light curve to the data and subsequently added the galaxy flux to the reprocessed light curve for plotting purposes.

For a standard thin disc (e.g. Shakura and Sunyaev, 1973) around a black hole of mass $5.24 \times 10^7 M_\odot$, and with an average accretion rate of $\sim 5\%$ of the Eddington limit, 50% (100%) of the V band emission is expected to arise from within 70 $(600) R_g$. As the light crossing time for one R_g is $R_g/c \approx 250$s, an edge-on disc would smooth the reprocessed V light curve on time-scales of $\sim 2 \times 70 R_g/c = 0.4$ days. Note that the inclination angle to the observer is only used to calculate the correct light travel times from different locations in the disc to the observer. As the light crossing time of the optically emitting region is shorter than the usual 2-day sampling rate of the X-rays, the smoothing of the fluctuations produced by differential light crossing time is small and the reprocessed light curve does not depend sensitively on i.

Figure 3.6 shows the best-fitting reprocessed V light curve together with the observed V band data. The corresponding parameters are $h_X = 21.5$ $i = 24°$, $\dot{m} = 0.06$ and $R_{\rm in} = 37.6 R_g$. The mean predicted optical flux is very similar to the observed flux, the ratio of mean fluxes for the light curves shown is 0.993. The normalised transfer functions for the V and u bands, using these best-fit parameters, were calculated by P. Arévalo and are shown in Figure 3.7. It assumes an X-ray flare of observed flux 4×10^{-11} erg s^{-1} cm^{-2}, illuminating the disc for 0.01 days. The first peak in the transfer functions corresponds approximately to the time lag of light reprocessed at the inner edge of the thin disc on the side nearest to the observer, and the secondary peak to the light reflected at $R_{\rm in}$ on the far side. The two peaks merge together for smaller inner truncation radii. Varying disc parameters has a small effect on the shape of the transfer functions and we note that in all cases their median lag is less than two days, i.e. smaller than the X-ray sampling. Therefore, the main effect of changing model parameters on the shape of the resulting optical light curve is to change the relative amount of intrinsic to reprocessed optical flux.

As can be seen from Figure 3.6, the reprocessed light curve reproduces the medium term fluctuations on the order of a hundred days moderately well, showing that it is energetically feasible to produce these optical fluctuations through reprocessing. The long term trend in the optical, however, is not present in the

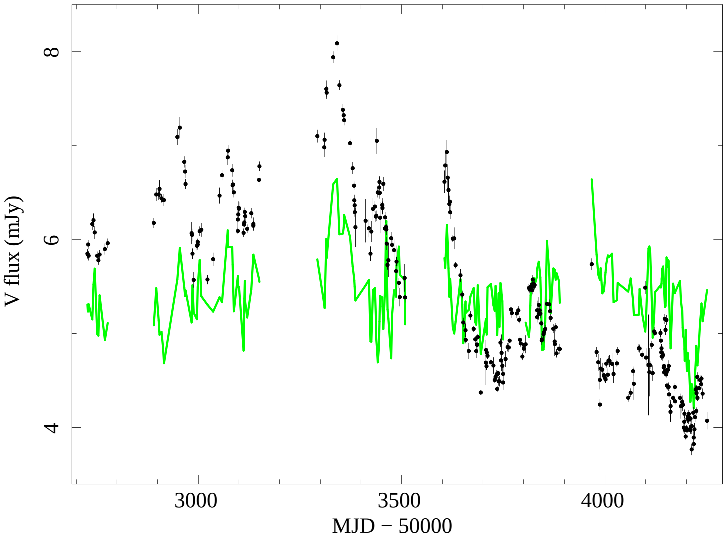

Figure 3.6: The fluctuations in the observed V band flux (black markers with error bars) cannot be reproduced by reprocessing of observed X-rays in a simple scenario where the geometry and disc accretion rate remain constant. The solid line shows an X-ray to V band reprocessed light curve with disc parameters that best fit the observed V band light curve.

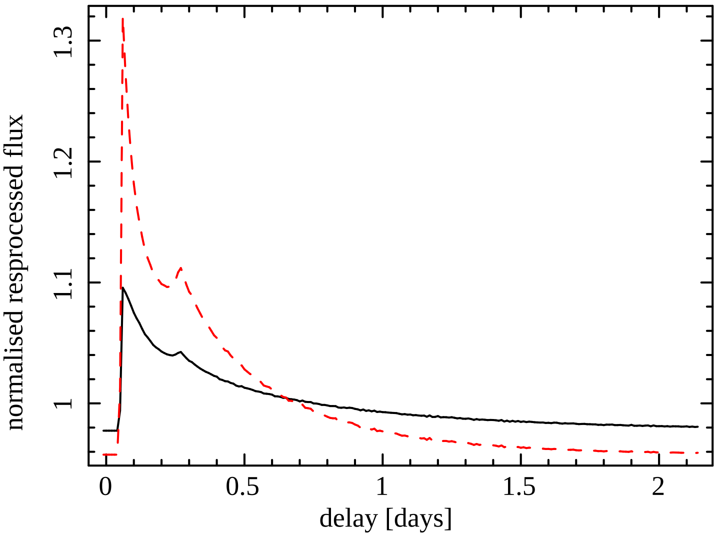

Figure 3.7: Disc reprocessing transfer functions for the V band (solid line) and u band (dashed line) calculated using the best-fit parameters of Figure 3.6. The first peak corresponds to the time lag of light reprocessed at the inner edge of the thin disc on the side nearest to the observer, and the second peak to the lag of the light reprocessed at the inner disc on the far side.

X-ray band and is not reproduced by the reprocessed light curve. This trend in the optical suggests that either the geometry changes, affecting the amount of reprocessed X-rays, or that the thin disc intrinsic luminosity changes over time-scales of years. To test these possibilities, we fitted each segment separately, allowing only one parameter at the time ($R_{\rm in}$, $\dot{m}$ or h_X) to vary between the segments. This setup reproduces roughly the behaviour of a change in disc/corona geometry or accretion rate on time-scales of years, while all other parameters remain the same. These scenarios, where the long term trends are produced by varying one model parameter, will produce different u band long-term variations. We therefore include the u band light curve in the fit (this was implemented by P. Arévalo) in an attempt to reproduce simultaneously both optical bands with the same set of model parameters over the three year segments where all three light curves overlap.

We start by allowing only the disc accretion rate to vary from one light curve segment to the next, while keeping the other two parameters constant between the segments. The best-fitting values of the accretion rate were 11% of the Eddington limit for the first segment shown in Figure 3.8, 4.8% for the second segment and 0.1% for the last segment, while keeping $R_{\rm in} = 6R_g$ and $h_X = 6R_g$. The resulting reprocessed u and V light curves are shown in the top panel of Figure 3.8. The large range in $\dot{m}$ is a consequence of the small truncation radius used, and represents the case where almost all of the optical emission in the lowest flux orbit comes from reprocessing. Other solutions, where $\dot{m}$ does not vanish, are possible, but require a larger $R_{\rm in}$ and result in a greater contribution from the intrinsic disc emission. The middle panel on this figure shows the result of fitting the different segments with a variable $R_{\rm in}$, keeping the accretion rate and source height fixed. In this case, the accretion rate was $\dot{m}$=7.7% and the source height $h_X = 7.8R_g$. The best-fitting truncation radii were $R_{\rm in} = 6R_g$ (minimum value allowed) for the first segment, $R_{\rm in} = 19.6R_g$ for the second and $R_{\rm in} = 41R_g$ for the third. Finally, the bottom panel in Figure 3.8 shows the result of a varying source height h_X. The best-fitting values are $R_{\rm in} = 6R_g$, $\dot{m} = 0.01$ and $h_X = 21.3R_g$ for the first segment, $h_X = 11.8R_g$ for the second and $h_X = 6R_g$ for the third. Evidently, varying any of these model parameters can reproduce broadly the long term trends in the V and u flux. The details of the reprocessed light curves, however, vary. In particular, varying the stable disc accretion rate adds different amounts of constant flux to the segments, while the amount of reprocessed flux remains approximately the same. Therefore, the short term fluctuations, arising from reprocessing, are the same size at high and low average flux levels. The opposite is true when varying geometry

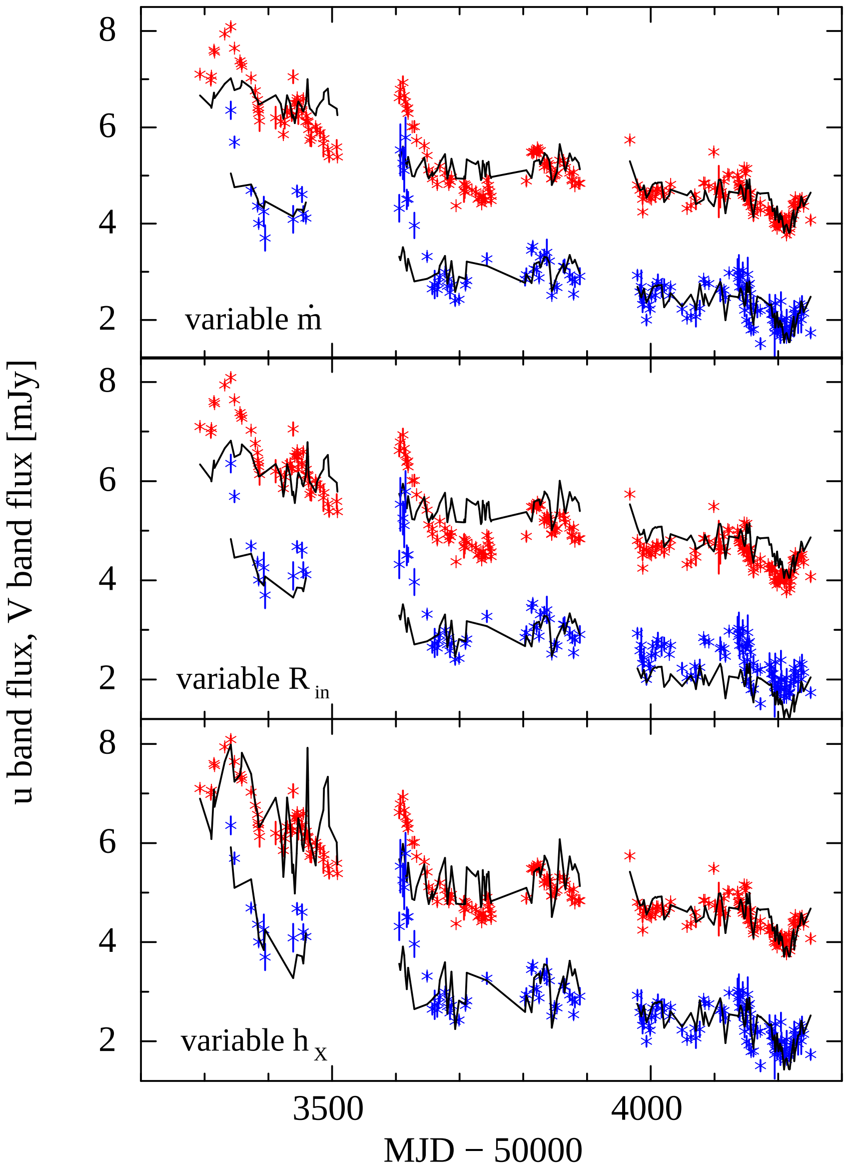

Figure 3.8: *u* (blue) and *V* (red) band light curves and predicted reprocessed X-ray flux (solid lines) obtained by changing only one parameter in the model between the different segments.

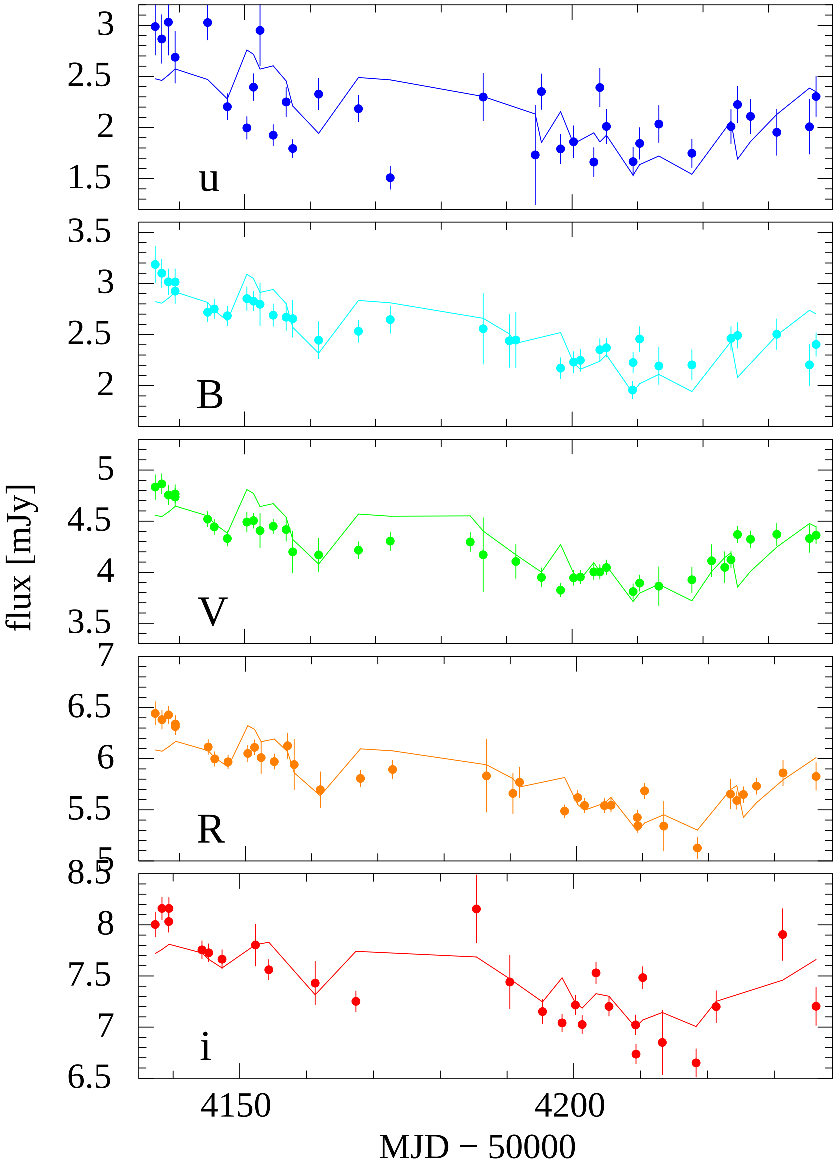

Figure 3.9: Reprocessed light curves for the multicolour intensive sampling data. The model parameters were fixed to the best-fitting parameters to the V band and the galaxy contribution in the other bands was allowed to vary as a free parameter.

parameters (source height or truncation radius). In these cases the size of the short term fluctuations scale with the mean flux. The average u and V flux levels are best reproduced by changing the accretion rate between the segments while the worst fit is obtained by varying $R_{\rm in}$. Changing this parameter has a much stronger effect on the u band than the V band, so the change in u flux is too large while the corresponding change in V is not large enough. The best overall fit, to the shape and the average flux levels is obtained by varying h_X, though the quality of the fits does not allow us to strictly rule out any of the scenarios.

To confirm that this process can produce the short-term fluctuations in the different optical bands as well, I also fitted the multicolour light curves obtained with the Faulkes Telescope with the reprocessing model. The model parameters were fixed to the values obtained from fitting the third segment of the u and V light curves with either variable h_X or variable $\dot{m}$, as explained above, i.e. $R_{\rm in} = 6R_g$, $\dot{m}$ =1% and $h_X = 6R_g$. As high resolution images exist only for the V band, we cannot estimate the galaxy contribution to the flux in the other optical bands, so we left the galaxy flux as a free parameter. The resulting galaxy fluxes are $u = 0.27$, $B = 0.67$, $V = 2.54$, $R = 4.08$ and $i = 5.83$ mJy. The reprocessed light curves for each band are shown by the solid lines in Figure 3.9.

3.5 Conclusions

We have presented the long-term optical (u and V band) and X-ray light curves of Mrk 79, obtained by combining data from several monitoring programs of this source. The u band light curve is the result of 2.5 years of monitoring with the Liverpool Telescope (LT) and the V band light curve was constructed from the combined data from six ground based telescopes, including the LT. The X-ray observations, which were made every ~ 2 days, are from our continuing monitoring program with the *RXTE* satellite. We further included the results from a 3 month multiwavelength program on the Faulkes Telescope in u, B, V, R and i.

We summarise our findings as follows:

i. The light curves are variable on time-scales as short as days (X-rays) and as long as thousands of days (optical), with highly correlated variability on time-scales of tens of days or months.

ii. Long time-scale (~years) variations are clearly seen in the optical light curve, but are not present in the X-ray light curve.

iii. Although there is more variability in the X-rays than in the optical bands on short ($\sim$day) time-scales, the fractional variability of the V band light curve on long time-scales is greater when corrected for host galaxy flux, due to the large amplitude of these long-term optical variations.

iv. The lags measured between the X-rays and long-term optical bands, are consistent with zero days for the data set as a whole. Formally we find that the V band lags behind the X-rays by $0.00^{+1.91}_{-4.00}$ days and the u band lags by $-1.95^{+1.95}_{-3.89}$ days.

v. While some strong events on a time-scale of a few days are consistent with the zero days lag, there are also time periods where the optical and the X-rays match up poorly and events are only seen in one passband.

vi. The variations between the short multicolour light curves are also well correlated. The measured centroid lags, τ, are consistent with the $\tau \propto \lambda^{4/3}$ prediction of X-ray reprocessing by an optically thick accretion disc. However, as the multicolour light curves are quite short, with few prominent peaks and troughs to constrain the lags, the error bars on the lag measurements are large and it is not possible to constrain the reprocessing model particularly tightly. We also cannot exclude the possibility that the measured delays across the optical bands are affected by a contribution from light reprocessed in the dusty torus further out.

vii. Optical variations on time-scales of $\sim$months are well reproduced by a reprocessing model, but longer term variations ($\sim$years) cannot be accounted for in this way.

In order to reproduce the long time-scale optical trends mentioned above, we are forced to include a second mechanism for the production of optical variations. This mechanism could be a variation in the geometry of either the purported accretion disc or the irradiating X-ray source. Changing the height of the X-ray source changes the fraction of the disc illuminated and hence the amount of optical emission produced by reprocessing. The intrinsic disc flux produced by viscous dissipation, is governed by $\dot{m}$ and changes in the inner truncation radius $R_{\rm in}$ affects the amount of optical emission produced. We have considered the effect of changing h_X, $\dot{m}$ and $R_{\rm in}$ individually, in steps between the three sections of the optical light curves (Figure 3.8). We find that when we vary h_X, we are able to reproduce the large and small fluctuations of the observed light curves slightly better than when we vary the disc parameters. It is not possible, however, at this level of modelling, to rule out the other two possibilities. A crude model like this cannot reproduce the observed light curves exactly. In reality the parameters will probably all vary together, rather than one at a time as we have done here, and also gradually, rather than in a step-wise fashion. The description of the X-ray source as a point source above the centre of the disc, although providing a reasonable approximation to an extended hemispherical corona, may also not be correct. However, the requirement for an additional source of optical variation, in addition to X-ray reprocessing, is robust.

Despite the good correlation on short time-scales, there are some short time-scale variations which appear to occur only in one passband. This mismatch needs to be addressed by future studies and may be a consequence of anisotropic X-ray emission (see, e.g. Gaskell, 2006).

Within the standard accretion disc model (Shakura and Sunyaev, 1973), the high black hole mass and low accretion rate of Mrk 79 implies that it has a cool disc. In such a disc, the X-ray and optical emitting regions are closer together, in terms of gravitational radii, than in a system of low black hole mass and/or high accretion rate. Hence both reprocessing and intrinsic variations are expected to contribute to the observed optical variability. Reprocessing benefits from the large solid angle subtended by the disc in the inner regions and intrinsic variations propagate on observable time-scales, because of the shorter viscous time-scale at smaller disc radii. We have previously reported this behaviour in the quasar MR2251-178 (Arévalo et al., 2008). This system has a very massive central black hole ($M \sim 10^9 M_\odot$) and hence a cool disc, with the X-ray and optical emitting regions even closer together than in Mrk 79, in terms of gravitational radii. When accretion rate fluctuations propagate through the disc, the X-ray and optical emitting regions are modulated together, leading to a good correlation on long time-scales. Reprocessing of X-rays imprints small rapid fluctuations onto the optical light curve, resulting in a well correlated behaviour on short time-scales as well. The strong X-ray–optical correlation reported here is in agreement with this picture.

For Mrk 79 we expect that 50% of the V band emission should originate within $70R_g$ of the black hole. Taking a typical value for the viscosity parameter, $\alpha \sim 0.1$, in an optically thick, standard accretion disc (Shakura and Sunyaev, 1973), with thickness $h/R \sim 0.1$, we find that the viscous time-scale at $70R_g$ is $t_{\rm visc} \sim 5$ years. In a geometrically thin disc, this time-scale is even longer. This (approximate) time-scale, on which we would expect accretion rate perturbations to propagate inwards to the X-ray emitting region, is longer than the time over which we have observed the steep decrease in optical flux and hence consistent with the fact that we have not yet seen a decrease in long term average X-ray luminosity. However the connection between the disc and the corona is not well understood and it is not clear how accretion rate variations, which may affect the optical disc emission, will be translated to the X-ray emission. If this interpretation is correct, the X-ray light curve should decline significantly over the next 5 or more years.

In the following chapters I will first look in detail at the X-ray/optical relationship in NGC 4051, a low black hole mass system, and then compare the X-ray and optical variations of a number of other AGN of differing black hole mass and accretion rate, and hence of differing disc structure, in order to determine how disc structure affects both the long and short term optical variability of AGN.

4 A low mass example: NGC 4051

This chapter has been accepted for publication in MNRAS:
Breedt, E.; M^{c}Hardy, I. M.; Arévalo, P.; Uttley, P.; Sergeev, S. G.; Minezaki, T.; Yoshii, Y.; Sakata, Y; Lira, P. and Chesnok, N. G., *MNRAS*, 2009

4.1 Introduction

NGC 4051 is a low-luminosity narrow-line Seyfert 1 galaxy, known for its extreme X-ray variability (e.g. M^{c}Hardy et al., 2004). The relationship between the X-ray and UV/optical variability in this galaxy has been the subject of many papers, reporting varied and conflicting results. Over the course of 3 nights Done et al. (1990) found the X-rays to vary by a factor of 2, but no corresponding variations in the optical or infrared were seen. Klimek et al. (2004) also studied the short time-scale optical variability of this galaxy. They detected microvariability on one of the five nights it was observed. Uttley et al. (2000) found a strong correlation between the X-ray and EUV variations, and measured them to be simultaneous to within 1 ks. Peterson et al. (2000) concluded that the X-ray and optical emission was correlated on time scales of months to weeks, but by applying a 30 day smoothing boxcar to the light curves before calculating the cross-correlation, a measurement of any lag shorter than this could not be obtained. During a period of very low X-ray flux they found that the broad He ii λ4686 line greatly decreased in intensity as well, showing no noticeable variation during this period, but that the optical continuum and Hβ line were only slightly fainter and continued to vary. They interpreted this is as the inner disc turning into an advection-dominated flow, greatly reducing the short wavelength (UV/blue) emission from this part of the disc. A 3-month simultaneous X-ray and optical monitoring program by Shemmer et al. (2003) revealed significant evidence of a correlation close to zero lag. They found the optical emission in this case to *lead* the X-ray emission by 2.4 days, and note that the variability of the optical light curve was much less than that of the X-rays. On shorter time-scales, Mason et al. (2002) find the UV to lag the X-rays, which they interpret as reprocessing by a ring of material at a distance of 0.14 light-days. This result has also been confirmed by Smith and Vaughan (2007), using the same data. Reverberation mapping studies using the Hβ line (Peterson et al., 2000; Kaspi et al., 2000; Peterson et al., 2004) place the broad line region in this AGN at a distance of $\sim$6 light-days from the central ionising source.

It is clear that a combination of processes can contribute to the observed optical variability and that different processes can drive the variability on different time-scales. In this chapter, I combine the observations from 4 different telescopes with some archival data, to revisit the topic of X-ray and optical variability in NGC 4051. The light curves together span more than 12 years, allowing us to study the variability on much longer time-scales than has been done before in this source. The emission is found to be highly variable in all wavebands, and the amplitude of the optical variations is found to be smaller than that of the X-rays, even after correcting for the contaminating host galaxy flux falling inside the photometric aperture. I also calculate the optical power spectrum and show that it is best described by an unbroken power law model with slope $\alpha = 1.4^{+0.6}_{-0.2}$. Comparing the optical to the X-ray PSD, it is clear that the optical emission is less variable than the 2–10 keV X-rays on all time-scales probed. The light curves are significantly correlated at an optical delay of $1.2^{+1.0}_{-0.3}$ days behind the X-rays. This time-scale is consistent with the light travel time to the optical emitting region of the accretion disc, suggesting that the optical variations are driven by X-ray reprocessing. I show, however, that a model whereby the optical variations arise from reprocessing by a flat accretion disc cannot account for *all* the optical variability. There is also a second significant peak in the cross-correlation function, at an optical delay of $39^{+2.7}_{-8.4}$ days. The lag is consistent with the dust sublimation radius in this source, suggesting that there is a measurable amount of optical flux coming from the dust torus. This possibility is considered in detail in Section 4.6.1.

4.2 Data

4.2.1 V band optical observations

The V band optical light curve presented in this chapter is a combined light curve from four telescopes: the Liverpool Telescope (LT) at the Observatorio del Roque de Los Muchachos of the Instituto de Astrofisica de Canarias, La Palma, Spain (Steele et al., 2004), the Faulkes Telescope North (FT) at Haleakala, Maui, Hawaii, the MAGNUM (Multicolor Active Galactic Nuclei Monitoring) telescope (Yoshii et al., 2003) at the University of Hawaii's Haleakala Observatory, Maui, Hawaii, and the 0.7-m telescope of the Crimean Astrophysical Observatory (CrAO) in the Crimea, Ukraine (Sergeev et al., 2005). The data reduction procedures and light curve construction are described in detail in Breedt et al. (2009), so I only give a brief summary below.

NGC 4051 was observed through a Bessell-V band filter from 2004 December 9 to 2008 December 11 with the Liverpool Telescope and from 2007 February 5 to 2007 August 10 with the Faulkes Telescope North. The two telescopes are identical in design. Observations in other filter bands, on both telescopes, started in early 2007 and continued until 2007 August on the FT and 2008 July on the LT. The data reduction and photometry was done using standard techniques in IRAF. I performed aperture photometry on the individual images, using an aperture of $12''$ diameter, centred on the nucleus of the galaxy. The relative fluxes were calibrated with respect to four comparison stars in the field, and the final flux calculated using the comparison star magnitudes of Doroshenko et al. (2005a).

The MAGNUM telescope observed NGC 4051 in the V band from 2001 January 8 to 2007 July 30. Data from the start of this program until MJD 52819 (2003 June 29) have been published by Suganuma et al. (2006). The rest of the light curve has not been published before.

Observations at the CrAO were carried out between 2001 December 27 and 2006 August 18. The data from MJD 53058 (2004 February 23) onward were previously unpublished. The filter set on the Crimean telescope is non-standard, but their B, V, R and I filters are close to the Johnson/Bessell filters and their $R1$ filter is similar to the Cousins I filter (Doroshenko et al., 2005a, see also Chapter 2, Figure 2.4).

The light curves from the different telescopes were made using different aperture sizes, so each is affected by a different amount of host galaxy contamination, resulting in different average flux levels. To account for this, as well as for the slight differences in the filters and any other small systematic differences in the calibration, I used the overlapping parts of the light curves to match them in a least squares fashion. I extracted pairs of measurements, taken within one day of each other, from overlapping light curves, and performed a least-squares fit of the equation $F_1 = aF_2 + b$ to the flux pairs. F_1 and F_2 are the flux measurements from the two datasets and a and b the parameters of the fit. The points were weighted for the fit, by the inverse of the time difference between F_1 and F_2, so that measurements made closer together in time have a greater influence on the fit. The best-fit parameters from each pair of overlapping light curves were then used to scale that dataset to the $15''$ diameter aperture V band light curve from the CrAO telescope.

The V band light curve used in the analysis, is the final combined light curve, corrected for Galactic reddening and host galaxy flux inside the aperture (see Section 4.2.5). It is shown in Figure 4.1, normalised to its mean flux, for direct comparison with the X-ray variations. Full sampling characteristics of this light curve may be found in Table 4.1.

4.2.2 AGN Watch continuum light curve

NGC 4051 was also observed spectroscopically between 1996 January 12 and 1998 July 28 as part of the International AGN Watch program (e.g. Peterson, 1999). Light curves from this program are publicly available[1] and I include in the analysis the 5100Å continuum light curve originally presented by Peterson et al. (2000). I subtracted the host galaxy contribution inside the $5.0''\times7.5''$ spectroscopic aperture, as measured by Bentz et al. (2009), and converted the light curve to mJy units, to compare with our V band light curve. Note that in this light curve the continuum flux is measured from a line-free region around 5100Å of the optical spectra, while the broad band observations will contain the line emission that fall inside the V band bandpass, such as [O III]$\lambda\lambda$4959,5007 and Hβ λ4861. The contribution of the lines to the measured flux will be discussed in Section 4.4.1. The light curve is plotted in Figure 4.1, together with the X-ray and V band light curves.

4.2.3 Multicolour optical observations

In addition to the V band observations described above, the CrAO also observed NGC 4051 in the B, R, $R1$ and I filter bands during the same period. The

---

[1] http://www.astronomy.ohio-state.edu/∼agnwatch/

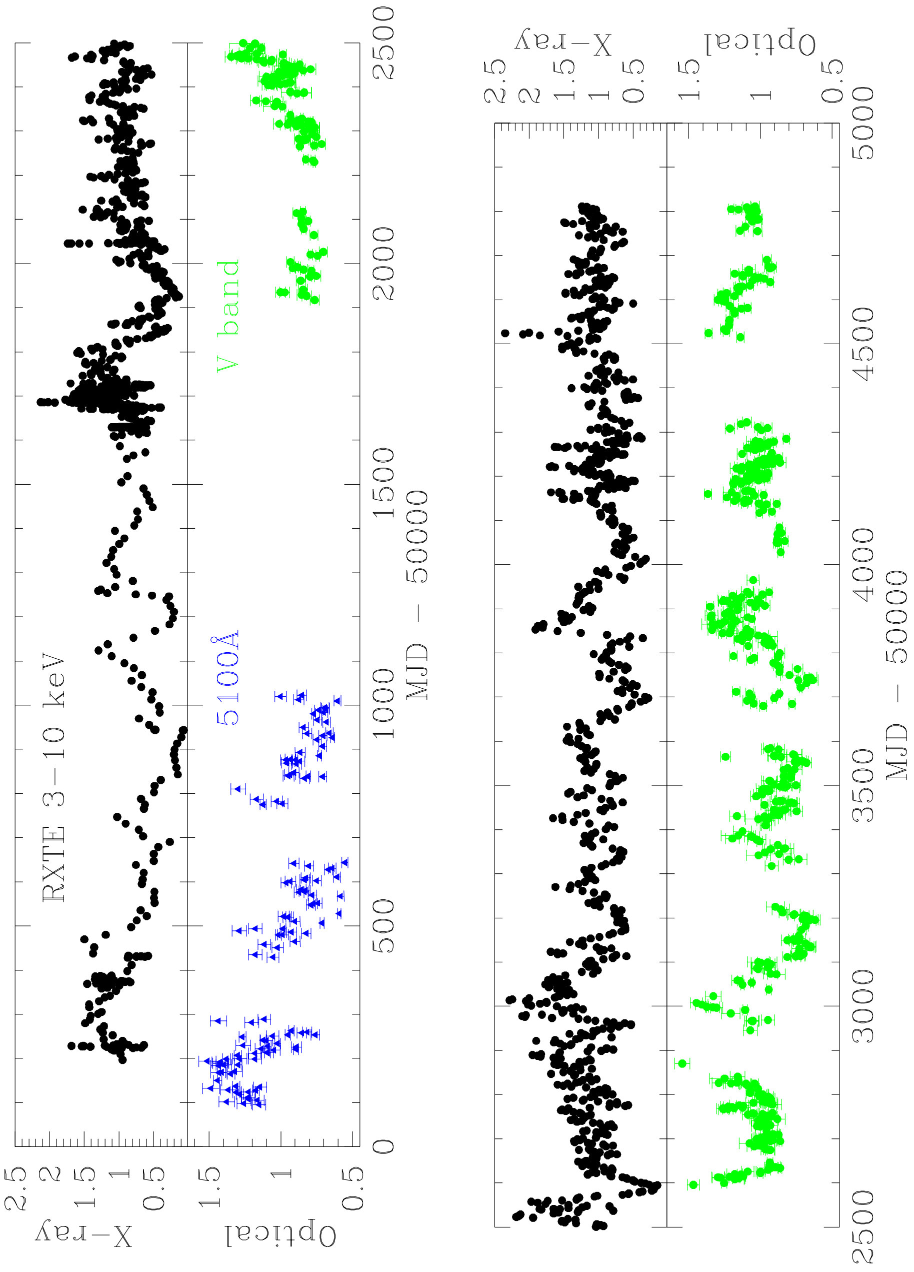

Figure 4.1: 3 – 10 keV X-ray (top panel in each part) and optical (bottom panel in each part) light curves of NGC 4051, corrected for host galaxy flux inside the aperture. Each light curve is normalised to its mean flux for direct comparison of the variability amplitudes. Note that the vertical scales for the optical and X-ray light curves are different – the amplitude of the optical variations is smaller than that of the X-rays. The X-ray light curve is smoothed with a 4 point (∼1 week) running average (for plotting purposes only), to highlight the variations on timescales similar to that of the optical light curve. The first part of the optical light curve, plotted in blue triangles, is the 5100Å continuum light curve from the AGN Watch program. The rest of the light curve, plotted in green dots, is the combined *V* band light curve from 4 different telescopes.

light curves are constructed from aperture photometry through a $15''$ diameter aperture centred on the galaxy nucleus, relative to a comparison star in the field. I used the comparison star fluxes from Cackett et al. (2007) to convert the light curves to flux units in these bands. The data from the start of this program, until MJD 53022 (2004 January 18), have been published by Sergeev et al. (2005) and were also analysed by Cackett et al. (2007). Data after this date were previously unpublished.

These light curves are supplemented with Sloan Digital Sky Survey (SDSS)-u band observations made by the Liverpool Telescope between 2004 December 9 and 2008 July 27. The data from short monitoring programs in B and R on the Liverpool and Faulkes telescopes (2007 February 5 – 2008 July 27) were combined to extend the CrAO light curves. Unfortunately there is no overlap between the LT/FT and the CrAO light curves in these bands, so it was not possible to combine them as described in section 4.2.1. To ensure the best possible match between the light curves, the same comparison stars were used in the flux calibration of the two datasets, and the appropriate aperture corrections were applied to the LT/FT light curves. However, it is possible that small differences in the calibration, or between the filters on the different telescopes, may cause a small offset between the CrAO and LT/FT light curves. The positions in the light curves that are affected by this, are indicated by dotted lines in Figure 4.2. Note however, that due to the "segmentation" technique I use to calculate the correlation functions (Section 4.4), a possible small offset like this does not affect the cross-correlation results. The light curves are shown, together with the corresponding segment of the X-ray light curve, in Figure 4.2.

The flux uncertainty on each point, based upon the differential photometry error and the relative calibration of the light curves, is approximately 3%. The uncertainty in the comparison star fluxes introduce a $1-4\%$ error in average flux of the different bands, but note that this error does not increase the scatter in the light curve, so it does not affect the cross-correlation results below. Sampling statistics for each light curve are shown in Table 4.1.

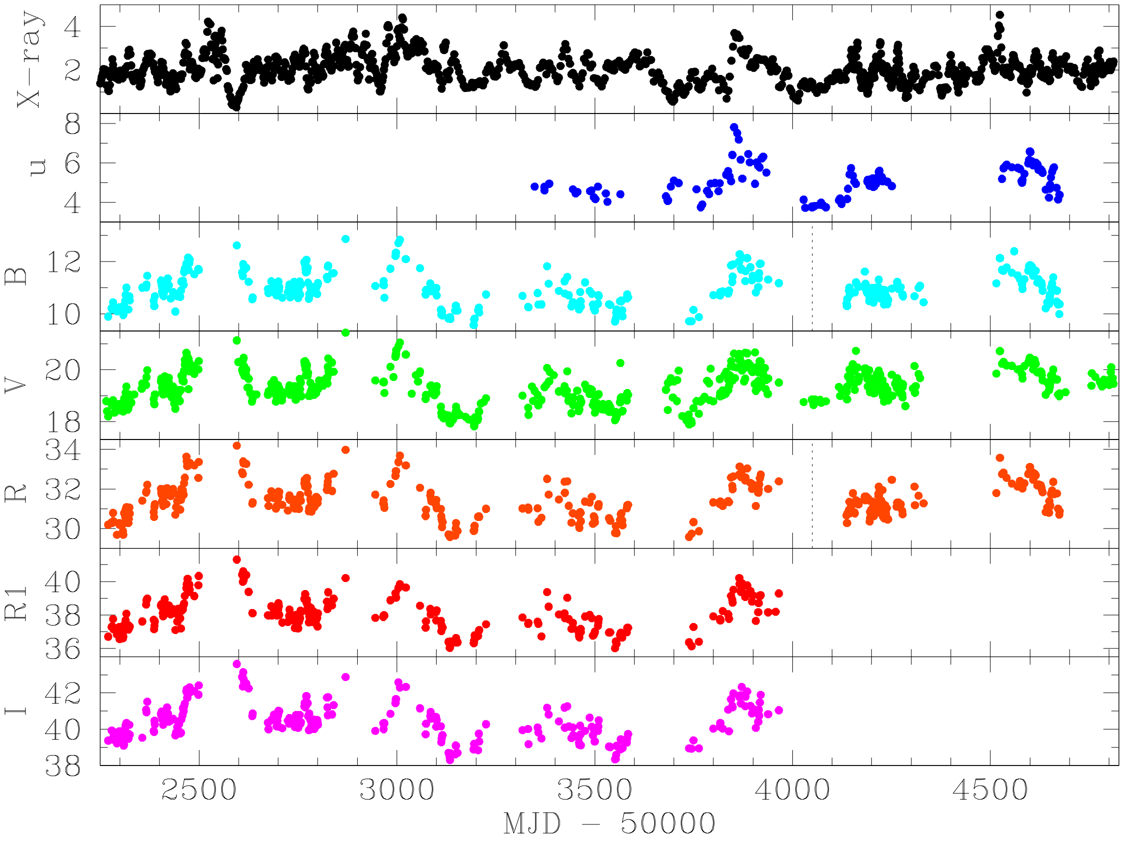

Figure 4.2: X-ray, *u*, *B*, *V*, *R*, *R*1 and *I* band light curves of NGC 4051. The X-ray light curve is in units of 10^{-11} erg s^{-1} cm^{-2} and the optical light curves are in mJy. The fluxes have been corrected for the small amount of Galactic extinction towards the source, but host galaxy flux has not been subtracted. The dotted lines in the *B* and *R* band light curves indicate the positions where there might be a small offset between the light curves on either side of the line, as there was no overlap between the data from the different telescopes. This does not affect our cross-correlation results however (see text).

Table 4.1: Observational characteristics of all light curves

Light curve	Telescope	Observation dates (MJD)	Total length (d)	Number of epochs	Δt_{mean} (d)	$\Delta t_{\mathrm{median}}$ (d)	Mean flux* (mJy)
X-ray	*RXTE*	50196 – 54811	4615	1811	2.55	1.96	$1.93 \pm 0.95^{\ddagger}$
u	LT	53348 – 54675	1327	128	10.4	4.01	5.41 ± 0.93
B	combined	52271 – 54675	2404	386	6.24	1.96	11.5 ± 0.61
5100Å	AGN Watch	50095 – 51023	928	126	7.42	3.15	11.1 ± 0.93
V	combined	51917 – 54811	2894	629	4.61	1.94	20.1 ± 0.64
R	combined	52271 – 54675	2404	384	6.28	1.97	32.3 ± 0.91
$R1^{\dagger}$	CrAO	52271 – 53965	1694	265	6.42	1.98	38.9 ± 1.02
I	CrAO	52271 – 53965	1694	261	6.52	1.98	41.3 ± 1.02

[*] Including host galaxy flux

[‡] In units of 10^{-11} erg s^{-1} cm^{-2}

[†] The $R1$ filter corresponds approximately to the Cousins I filter

4.2.4 X-ray observations

NGC 4051 is part of our long term AGN X-ray monitoring program using *RXTE*, which started on 1996 April 23. Here I include the observations up to 2008 December 11, to overlap with the optical light curve. The observational frequency and variability characteristics of this light curve are summarised in Tables 4.1 and 4.2. The observations are in the form of approximately 1 ks snapshots using the Proportional Counter Array (PCA) on board *RXTE*. The PCA consists of five identical proportional counter units (PCUs) but as some of them were regularly switched off during our observations, I only extracted data from PCU2 to construct the X-ray light curve. For maximum signal-to-noise, I used only the data from the top layer. Using FTOOLS v.6.4, I applied standard extraction techniques and re-reduced all the available data, so that the latest *RXTE* background models may be applied throughout the light curve. Data obtained within 10 minutes of passing through the South Atlantic Anomaly (SAA), data gathered less than 10° above the limb of the Earth or with pointing offset greater than 0.02° from the source, and data for which the electron current was greater than 10%, were rejected. To obtain the flux measurement, I fit a power law model to the spectra using XSPEC and integrate the flux in the range 3–10 keV. The error on the flux measurements were calculated from the counts in each observed spectrum, weighted by the response function.

The normalised 3–10 keV X-ray light curve is shown in Figure 4.1, smoothed with a 4-point ($\sim$1 week) running average. This is done to highlight fluctuations on similar time-scales as those in the optical light curve, but note that, throughout this thesis, the unsmoothed, unbinned light curve was used in the analysis.

4.2.5 Galaxy flux in the aperture

The photometry aperture contains the nuclear emission as well as a constant contribution from stars in the host galaxy. Although this constant offset does not affect the results of the cross-correlation analysis, it reduces the amplitude of the observed variations. Hence, to investigate the variability of the nucleus, this component must be subtracted from the light curve.

In order to estimate the amount of host galaxy flux contained in the $15''$ aperture, I decomposed the images using GALFIT (Peng et al., 2002), by fitting a PSF (point spread function – using stars in the field of the galaxy), a de Vaucouleur profile and an exponential disc to each image. The decomposition of individual images was poor, so I stacked together 12 images taken under good seeing conditions, to improve the signal-to-noise. This resulted in much better, stable fits of the different components. The variable nucleus was taken account of by selecting only images from which approximately the same flux was measured through the aperture. I subtracted the best fit galaxy profile in each band from the images and measured the flux of the residual PSF-like image. The difference between this PSF-like image and the flux measured through a 15″ aperture on the original image, was taken as the galaxy contribution f_g. The measured fluxes, corrected for foreground Galactic extinction, are listed in Table 4.2.

I did not have $R1$ and I band images available to measure the galaxy contribution by decomposition as above, so the galaxy contribution in these bands were estimated by extrapolating from the galaxy contribution measured in the SDSS-i band. The fluxes in Table 4.2 are in good agreement with those found by Salvati et al. (1993) and also agrees well with the galaxy-subtracted V band light curve published by Suganuma et al. (2006). I show in Figure 4.3 the measured galaxy fluxes, converted to F_λ units and corrected for the small amount of foreground Galactic extinction towards the source. It is shown together with a template spectrum of the central regions of a normal spiral galaxy similar to NGC 4051 (Santos et al., 2002; Bica, 1988). The template spectrum was constructed from a group of 30 galaxies, mostly of morphological type Sb, but also including Sa and Sc galaxies. NGC 4051 is classified as an Sbc galaxy. The template is corrected for Galactic extinction and normalised at 5870Å. The measured galaxy fluxes agree well with the template spectrum, indicating that the f_g measurements are good estimates of the host galaxy flux inside the aperture. Flux-flux plots between galaxy-subtracted light curves in different energy bands suggest that the error on f_g is between 10 and 15%.

4.2.6 Fractional variability

In order to compare the amount of intrinsic variability in each wavelength band, I calculate the fractional variability (Eqn. 3.1) of each light curve. For convenience of the reader, the definition is repeated here:

$$F_{\rm var} = \frac{\sqrt{\sigma^2 - \langle \varepsilon^2 \rangle}}{\langle f \rangle} \,. \tag{4.1}$$

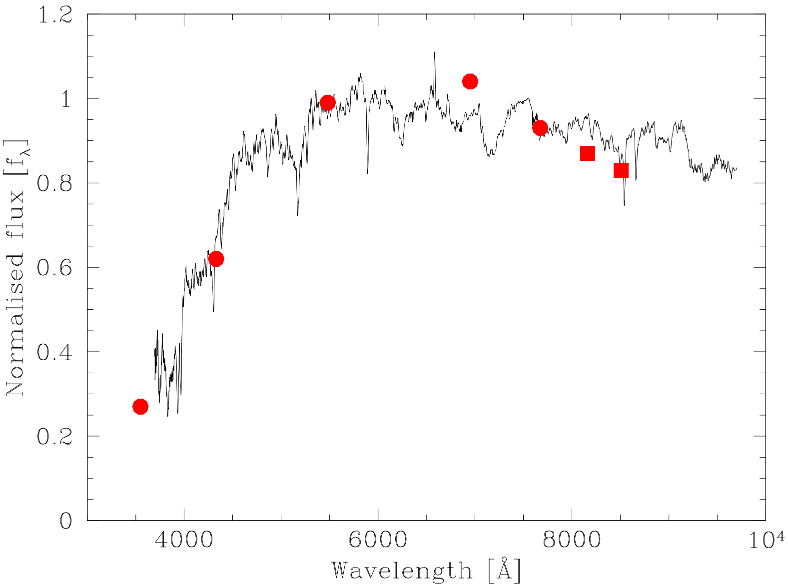

Figure 4.3: Measured galaxy flux inside the aperture (plotted in dots), compared to a template spectrum of the central regions of a normal spiral galaxy similar to NGC 4051. The last two points, plotted in squares, are the flux estimates for the $R1$ and I bands. These points were extrapolated from the SDSS-i flux measurement (last dot), as we did not have images available in these bands.

The error on $F_{\rm var}$ is given by

$$\varepsilon_{(F_{\rm var})} = \sqrt{\left(\sqrt{\frac{1}{2N}}\frac{\langle \varepsilon^2 \rangle}{\langle f \rangle^2 F_{\rm var}}\right)^2 + \left(\sqrt{\frac{\langle \varepsilon^2 \rangle}{N}}\frac{1}{\langle f \rangle}\right)^2 + \left(F_{\rm var}\frac{\Delta\langle f_g \rangle}{\langle f_g \rangle}\right)^2} \,. \tag{4.2}$$

The first two terms of this equation is the formulation as derived by Vaughan et al. (2003), using an analytical fit to the results of their Monte Carlo simulations. The last term under the square root accounts for the uncertainty associated with the galaxy subtraction (P. Arévalo, private communication). f_g is the measured host galaxy flux, and Δf_g its associated uncertainty. The host galaxy flux is assumed to be a constant contribution to each point in the light curve. Hence subtracting this flux only affects the mean of the light curve, it does not increase the point-to-point scatter. The error on the galaxy flux should therefore not be included in the sum of the observational noise errors (Eqn. 3.3). Instead, it is included only in the calculation of the *error* on $F_{\rm var}$ (Eqn. 4.2). Note that as the host galaxy flux is a constant offset to the light curve, neither its subtraction nor the error associated with it affect the cross-correlation results. The fractional variability, as well as the ratio of the maximum to minimum flux in each light curve, is given in Table 4.2.

The variability characteristics of the 5100Å continuum light curve and the galaxy contribution measured by Bentz et al. (2009), is also shown, but note that this light curve was made using a smaller aperture than our light curves and that the galaxy contribution was measured from much higher resolution images than I used here. There may therefore be a difference in the amount of host galaxy flux subtracted, so the fractional variability in this band should not be compared directly with the other light curves. The X-ray and optical light curves are all highly variable. In agreement with the finding of Shemmer et al. (2003) that the optical continuum variations are less than the X-rays on time-scales of months, we find that the same is true on time-scales of years. The optical continuum (all light curves, including the 5100Å light curve) is less variable than the X-rays, even after correcting for host galaxy starlight in the aperture.

In the X-ray reprocessing scenario, the fast variations of the X-ray light curve are smoothed out by the disc, so a smaller fractional variation of the optical light curves is expected. The results in Table 4.2 are broadly consistent with this expectation, showing a decrease in $F_{\rm var}$ towards longer wavelengths. However, due to the uncertainty in the galaxy subtraction, the error on $F_{\rm var}$ is large, and the decreasing trend is not strong. The observation that the variability of the optical bands is less than that of the X-rays is nevertheless robust. I note that the variability of the B band light curve is lower than the other optical bands and does not follow the decreasing trend. The mean flux of the galaxy-subtracted B band light curve is also slightly higher than that of the V band, which is contrary to expectation, assuming the emission in both bands originate in an accretion disc. This suggests that the low fractional variability in the B band may be the result of underestimating the galaxy contribution in this band. Increasing the galaxy contribution by 20%, increases $F_{\rm var}$ to $15.5 \pm 1.3\%$. The larger error may be attributed to the fact that the galaxy spectrum rises steeply in the B band (see Fig. 4.3), and is likely to be very different from the spectrum of the comparison star used in the differential photometry. The lower variability of the optical with respect to the X-ray variations, suggests that reprocessing of X-rays may account for the optical variability in this source. I return to this possibility in Section 4.5.

4.3 The optical power spectrum

Power spectra are a commonly used technique to investigate the aperiodic variability displayed by AGN and X-ray binaries. It describes the variability power present

Table 4.2: Estimated host galaxy flux inside the 15″ aperture and variability characteristics of all light curves, after subtracting the host galaxy contribution.

Light curve	f_g (mJy)	$F_{\rm var}$(%)	$f_{\rm max}/f_{\rm min}$
X-ray	–	48.8 ± 0.8	89.0 ± 26.5
u	1.8	25.6 ± 1.8	3.92 ± 1.36
B	6.3	11.7 ± 1.5	1.92 ± 0.56
V	16.0	15.4 ± 3.1	2.48 ± 1.64
R	27.2	16.9 ± 3.8	2.46 ± 1.65
$R1$	31.5	13.8 ± 3.3	2.02 ± 0.92
I	32.7	11.8 ± 3.0	1.84 ± 0.72
5100Å	7.2*	23.9 ± 1.5	2.73 ± 0.15

*Bentz et al. (2009), in the 5.0″×7.5″ spectroscopic aperture.

in the light curve (mean squared amplitude) as a function of frequency. Generally, the X-ray Power Spectral Density (PSD) of these systems can be described by a power law $P(\nu) \propto \nu^{-\alpha}$ of slope $\alpha \sim 1$ up to a bend or break frequency ν_B, where the power law slope steepens to $\alpha \sim 2$ (e.g. M$^{\rm c}$Hardy et al., 2004; Summons, 2008). The corresponding break time-scale scales approximately linearly with the black hole mass, and the scatter in this relationship is largely accounted for by considering the difference in accretion rate between these systems (M$^{\rm c}$Hardy et al., 2006). The break frequency is thus characteristic of the system and is thought to represent a time-scale associated with the inner edge of the disc.

I use the Monte Carlo technique of Uttley et al. (2002) and Summons (2008) to estimate the parameters of the power spectrum underlying the optical variations. The method subtracts the mean of each of the component light curves and then calculates the discrete Fourier Transform of each part. The method is discussed in detail in Section 5.3. The resulting PSD is binned logarithmically in bins of width 1.5ν, with ν the frequency at the start of the bin.

I do not include the AGN Watch data here, as the slightly different wavelength will affect the normalisation of the power and hence the slope we measure. To extend the frequency range, I also include the V band light curve obtained by Klimek et al. (2004) as part of their microvariability study. I calculate the variability power on each of the five nights it was observed and bin the resulting PSDs together to give the power in the frequency range $6 \times 10^{-5} - 5 \times 10^{-4}$ Hz. The low frequency part of the PSD is calculated from the whole of the V band light curve and the middle range from the most intensively sampled part of the light curve from MJD 54181 to 54252.

I start by fitting an unbroken power law

$$P(\nu) = A\nu^{-\alpha} \tag{4.3}$$

to the power spectrum, allowing the slope α and the normalisation A to vary. The best fit, shown in Figure 4.4, is found to have $\alpha = 1.4^{+0.6}_{-0.2}$, with an acceptance probability[2] of 79.5 per cent. The shape of the X-ray power spectrum is included for comparison, plotted as a dashed line. The X-ray power spectrum has a slope $\alpha_L = 1.1^{+0.1}_{-0.4}$ at low frequencies, bending to a slope of $\alpha_H = 2.5^{+0.0}_{-0.8}$ and a frequency $\nu_B = 5.1^{+4.9}_{-2.6} \times 10^{-4}$ Hz (Summons, 2008, Summons et al., in preparation).

The unbroken optical PSD slope is intermediate in value between the low and high frequency X-ray slopes. If the optical PSD has a similar shape to the X-ray PSD, this suggests that a break is contained within the frequency range spanned by the optical data. Motivated by the shape of the X-ray PSD, I also fit a bending power law, of the form

$$P(\nu) = \frac{A\nu^{-\alpha_L}}{1 + (\nu/\nu_B)^{\alpha_H - \alpha_L}} \tag{4.4}$$

to the optical PSD. For direct comparison with the X-ray PSD, I fixed the low frequency slope to $\alpha_L = 1.1$ and allowed the high frequency slope α_H and bend frequency ν_B to vary. The best fitting parameters are found to be $\alpha_H = 1.5^{+1.0}_{-0.3}$ and bend frequency $\nu_B = 1.4^{+*}_{-*} \times 10^{-8}$ Hz. The errors are the values for which the acceptance probability drops below 10 per cent and the asterisk is used to indicate an unbounded error. The acceptance probability for this fit is slightly better than for the unbroken case, at 90.2 per cent, but the break frequency is unconstrained by the frequency space sampled by the data. Allowing all the parameters to simultaneously vary over a large range (i.e. not fixing the value of the low frequency slope), results in the same best-fit values, within the quoted 90% errorbars.

Figure 4.5 shows a colour density plot of the acceptance probability as a function of the parameter space searched, while fixing $\alpha_L = 1.1$. It shows that for $\alpha_H = 2.5$, as measured from the X-ray spectrum, the best-fit bend frequency is at $\nu_B = 4.4^{+*}_{-4.2} \times 10^{-7}$ Hz. The fit probability for these parameters is only 74.7 per cent, however, so it can be confidently rejected in favour of the unbroken model. It is

---

[2] The acceptance probability is the probability that the periodogram, as calculated from the observed light curve, is a realisation of a given power law model; see Section 5.3.

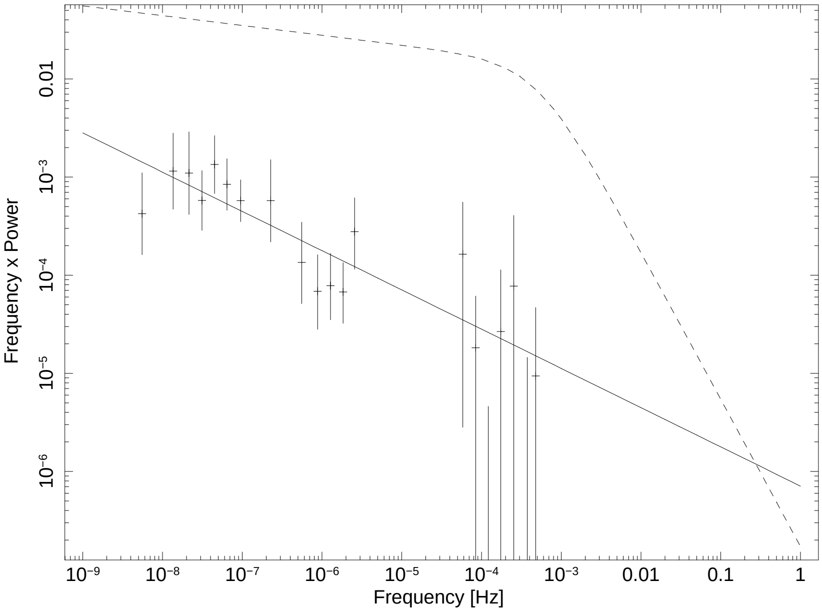

Figure 4.4: Unbroken power law model (solid line) fitted to the unfolded optical PSD (points with error bars). The slope of the best-fit model has $\alpha = 1.4$. The X-ray power spectrum (Summons, 2008) is shown in a dashed line for comparison.

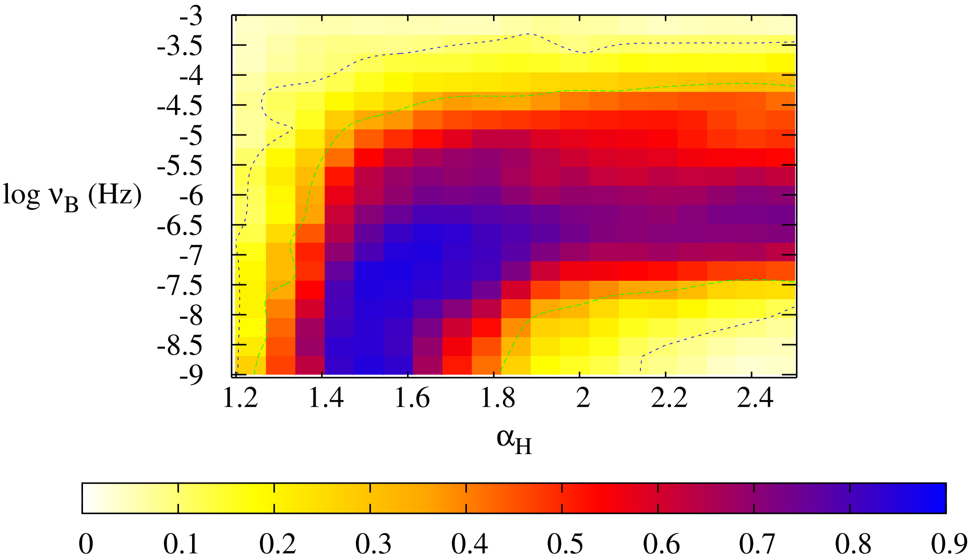

Figure 4.5: Acceptance probability as a function of α_H and ν_B for the parameter space searched. α_L was fixed at 1.1, for direct comparison with X-ray PSD. The best fit parameters yield an acceptance probability of 0.902. The lines superimposed on the colour plot are the 67% and 90% confidence contours.

clear from this figure that the best-fit bend frequency in the single-bend model is towards the lowest frequencies (longest time-scales) probed. A single-bend PSD cannot be ruled out for this system, but it would require further monitoring to confirm the existence of a bend at low frequencies. I therefore conclude that, with the current data, the optical power spectrum is best described by an unbroken power law model with slope $\alpha = 1.4$.

4.4 Cross-correlation analysis

4.4.1 X-ray – optical correlation

In order to test whether there is a measurable delay of one light curve with respect to the other, I calculate their cross-correlation function (CCF), using the interpolation method of Gaskell and Sparke (1986) and White and Peterson (1994). As discussed in Appendix A, I implement the method in two ways: in the first case, I linearly interpolate between adjacent points and resample both light curves to obtain equally spaced points for calculating the correlation ("equally sampled", or EQ method). For most of the monitoring time, however, the X-ray light curve is better sampled than the optical light curve. To take advantage of this and maximise the use of real, rather than interpolated data, I also use the "single interpolation" (SI) method, in which only the optical light curve is interpolated. The observed fluxes and observation times of the X-ray light curve are used in the calculation. The two methods give consistent results throughout, but for completeness the cross-correlation results from both methods are listed in Table 4.3.

To take account of the gaps in the optical light curve when the galaxy is not observable from ground-based observatories, the light curves are divided into segments, defined by these gaps and the correlation calculated between each segment and its corresponding segment of the X-ray light curve. The resulting CCFs are averaged, weighting them by the length (in time) of the light curve segments. The final CCF, calculated in this way, is shown in Figure 4.6. It shows a clear peak at $1.2^{+1.0}_{-0.3}$ days, and another at $38.9^{+2.7}_{-8.4}$ days. The errors are calculated using a simple bootstrap method. I select at random two-thirds of the points in the X-ray light curve, each along with its closest optical data point, recalculate the CCF and then measure the peak and centroid. I performed 1000 such selections to yield a distribution of peak and centroid values. The error range reported contains 68% of the measured values about the median. Here, and throughout this thesis, a positive

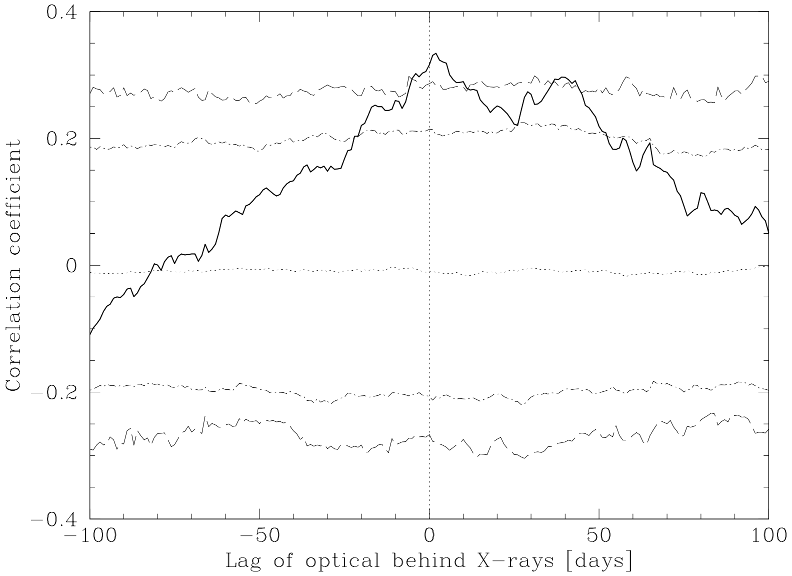

Figure 4.6: CCF between the X-ray and long term optical light curves, shown in Figure 4.1. The horizontal dotted, dot-dashed and dashed lines are the mean, 95% and 99% confidence levels, calculated from 1000 Monte Carlo simulations. The vertical dotted line indicates the zero lag position. Both the peaks are significant at greater than 99% significance.

lag indicates the longer wavelength band lagging behind the shorter wavelength band.

The segmentation technique also allows us to take account of the small difference in the flux level of the V band and 5100Å light curves due to different aperture sizes and a possible difference in the galaxy subtraction. The mean of each segment is calculated individually and subtracted from the segment before the correlation is calculated. The segmentation has the effect of removing long time-scale power from the light curve and allows a more accurate measure of the short time-scale lag between the light curves. Any small differences in the relative calibration of the light curves are therefore eliminated from the calculation.

I perform Monte Carlo simulations to test the significance of these lags in the following way: I generate 1000 random red noise light curves with the same statistical properties as the observed X-ray light curve, based on the method of Timmer and Koenig (1995) and the X-ray power spectrum parameters of NGC 4051 (Summons, 2008, see also this work, chapter 4.3). Each of these random, uncorrelated light curves is then sampled in the same way as the observed X-ray light curve and cross-correlated with the real, observed optical light curve, using the same segmentation technique as described above. The resulting CCF is recorded in each case

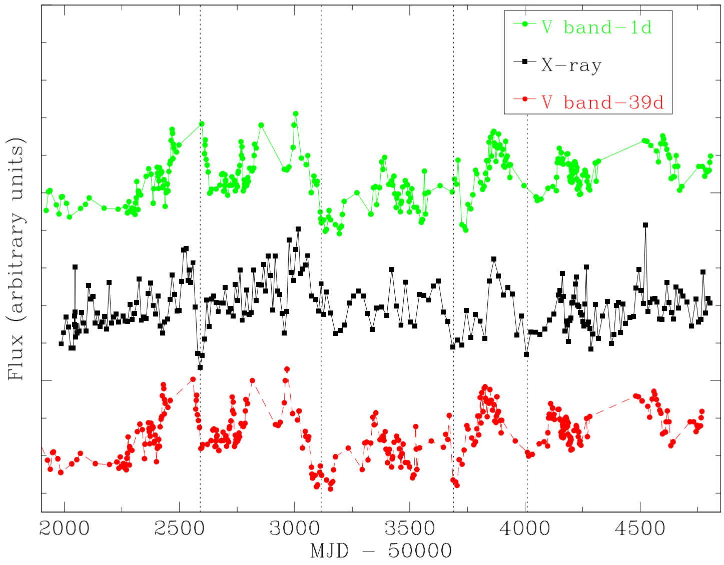

Figure 4.7: The optical *V* band light curve shifted back by 1 d (top) and 39 d (bottom), compared to the X-ray light curve (middle). The X-ray light curve was binned in 5 day bins for clarity. The short time-scale correspondence between X-ray and the optical light curve at the top is clear. The vertical lines indicate some of the variations which align better when the optical light curve is shifted back by 39 days, rather than by the main 1 day lag.

and compared with the CCF of the observed light curves. In this way the probability of finding spurious correlations may be assessed, i.e. chance correlations due to the red noise character of the light curves, that are higher than that of the real light curves. I overlay the mean, 95% and 99% levels of these simulations on top of the calculated CCF, in Figure 4.6. Both peaks reach higher than the 99% line, showing that the correlations are significant at greater than 99% confidence.

To illustrate the origin of the two lags in the light curves, I show in Figure 4.7 the optical light curve shifted by 1 (top) and by 39 days (bottom), in comparison to the X-ray light curve (middle). The X-ray light curve was binned in 5-day bins for clarity. Most of the X-ray variations on time-scales of days to weeks show corresponding variations in the optical light curve shifted by 1 day. However, a few of the minima and maxima align better with the 39-day shifted version of the optical light curve. Note that since both lags are short compared to the total duration of the light curve, only the largest amplitude variations can be clearly seen in Figure 4.7. The most obvious examples of the delayed variations are marked by dotted lines in that figure.

4.4.2 Lags between optical bands

It is clear from the light curves in Figure 4.2 that a strong correlation exists between the optical bands. Optical interband lags in this source have been measured by Sergeev et al. (2005) and Cackett et al. (2007), confirming the apparent correlation. Here I will consider the relationship between the X-rays and each of the optical bands.

Using the same segmentation technique as before, I calculate the correlation between the X-ray light curve and each of the different optical bands. The CCFs are shown in Figure 4.8, and the values of the peaks and centroids of the CCFs are summarised in Table 4.3. The centroid is calculated as the weighted average of the CCF points around the peak, at a value $\geq 85\%$ of the peak correlation coefficient. As before, a positive value of the lag indicates that the variations in the optical band are lagging behind the X-ray variations. All light curves, except the u band, for which the sampling is much sparser than the other light curves, show a correlation significant at greater than 99% confidence. The second peak near ~ 40 days is also seen, though not always at a significant level. Note however, that the strength of the second peak, *relative* to the peak at ~ 0 days, remains approximately constant.

The V band light curve used in this part of the analysis, consists of only those observations which overlap in time with the other colour light curves. From this segment of the data I measure a slightly shorter lag than from the full light curve, but the results are consistent within the 1σ errors. Also note that the lags measured from the central CCF peak are well within the ~ 6 light day estimate of the location of the Hβ broad line region (BLR) in this source (Peterson et al., 2000; Kaspi et al., 2000; Peterson et al., 2004), indicating that most of the variable optical emission originates in a structure smaller than the BLR.

In order to assess the influence of the delayed line emission on the measured lag, I first estimate the line contribution to the flux measured through the broad band filters. Using an average optical spectrum from the AGN Watch program, convolved with the filter response, I find a 3% line contribution to the V band flux and a 4% contribution to the B band flux. I then generate correlated X-ray and optical light curves, using the method described in Section 4.4.1, to represent the continuum emission. The line flux is represented as a smoothed version of theX-ray light curve, delayed by 6 days, as would be appropriate for a thin spherical shell of radius 6 light-days. The delayed line flux is added to the simulated, undelayed optical light curve in the ratios measured from the spectrum. 1000 such simulations

Table 4.3: Cross-correlation lags (in days). The centroid is the weighted average of the CCF values $\geq 85\%$ of the peak correlation coefficient.

CCF X-ray vs.	Peak (EQ)	Centroid (EQ)	Peak (SI)	Centroid (SI)
Optical¶				
first peak	$2.0^{+1.2}_{-0.6}$	$2.4^{+0.9}_{-1.6}$	$1.2^{+1.0}_{-0.3}$	$1.8^{+1.3}_{-2.0}$
second peak	$35.2^{+6.6}_{-5.1}$	$39.4^{+2.2}_{-2.1}$	$38.9^{+2.7}_{-8.4}$	$38.7^{+1.3}_{-1.0}$
u	$0.3^{+1.5}_{-1.3}$	$0.5^{+1.4}_{-1.6}$	$-0.2^{+1.6}_{-1.1}$	$0.1^{+2.0}_{-1.5}$
B	$2.3^{+1.5}_{-0.7}$	$2.6^{+0.5}_{-0.6}$	$1.5^{+0.8}_{-0.6}$	$2.0^{+0.8}_{-1.1}$
V	$1.1^{+0.5}_{-0.3}$	$2.2^{+0.3}_{-0.4}$	$0.6^{+0.4}_{-0.6}$	$1.3^{+0.8}_{-1.0}$
R	$3.1^{+1.0}_{-1.6}$	$2.8^{+0.6}_{-0.7}$	$1.5^{+1.6}_{-0.6}$	$2.0^{+0.9}_{-1.1}$
$R1$	$4.8^{+2.1}_{-3.3}$	$2.3^{+1.3}_{-1.7}$	$1.9^{+3.1}_{-1.0}$	$2.0^{+1.3}_{-2.2}$
I	$4.9^{+1.9}_{-2.4}$	$2.0^{+1.2}_{-1.9}$	$1.7^{+3.3}_{-0.8}$	$1.7^{+1.0}_{-1.7}$

¶This is the light curve shown in Fig. 4.1, including both the V band data and 5100Å continuum AGN Watch data.

yield a peak lag of $\tau_{\rm peak} = 0.0 \pm 0.1$ days and a centroid lag of $\tau_{\rm cent} = 0.1 \pm 0.6$ days, which is well within the errors on the lag measured in the real light curve. I therefore conclude that the line emission contributes too small a fraction of the total V band emission to noticeably affect the measured lag.

4.5 Reprocessing

The short, but measurable delays between the X-rays and the optical bands, as well as the small amplitude of the optical variations, suggest that reprocessing of X-rays plays a role in producing the optical variations. To test this hypothesis, I use the observed X-ray light curve to construct a model reprocessed optical light curve. This model light curve can then be compared to the observed optical light curve, as was done for Mrk 79 in Section 3.4.

As discussed in that section, the model assumes that the disc temperature is determined by the combined effects of viscous dissipation in the disc and variable heating by an X-ray source at height h_x above the disc and on its axis of symmetry. Assuming that each annulus of the disc emits as a blackbody, the temperature of

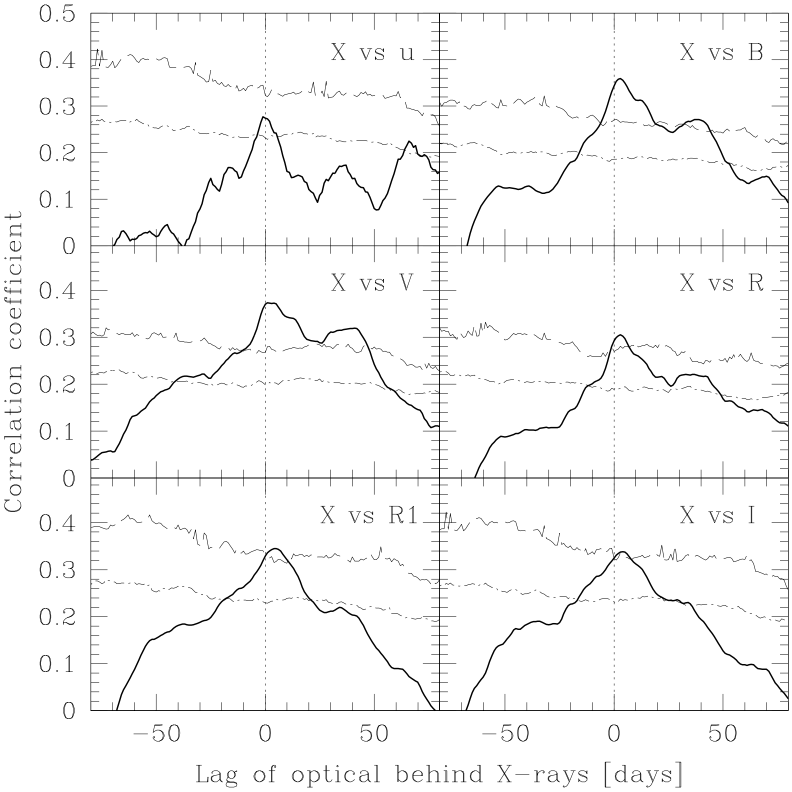

Figure 4.8: CCF between the X-ray and optical bands as labelled. The vertical dotted line indicates the zero lag position. For simplicity, we only show the 95% (dot-dashed line) and 99% (dashed line) confidence levels.

the disc is then given by

$$T(R,t)=\left[\frac{3\dot{M}c^2}{8\pi\sigma R_g^2}\frac{1}{R^3}\left(1-\sqrt{\frac{R_{\rm in}}{R}}\right)+\frac{(1-\mathcal{A})L_x(t)}{4\pi\sigma(h_x^2+R^2)}\cos\theta\right]^{\frac{1}{4}}. \tag{4.5}$$

Here $\dot{M}$ is the disc accretion rate in kg s^{-1}, R the distance of the disc surface element from the centre, $R_{\rm in}$ the location of the inner edge of the accretion disc, $L_x(t)$ the variable X-ray luminosity, $\mathcal{A}$ is the average disc albedo and θ the angle between the disc surface and the direction of the X-ray source. R, $R_{\rm in}$ and h_x are measured in units of the gravitational radius $R_g = GM/c^2$, where M is the mass of the black hole in kg. The delay between the variations of different wavebands is then due to the difference in light travel time to regions of the disc of different temperature.

I show in Figure 4.9 the lags predicted by this model, plotted as a dashed line, assuming $M = 1.91 \times 10^6 M_\odot$ (Peterson et al., 2004), $\dot{M} = 0.15\dot{M}_{\rm Edd}$ (Woo and Urry, 2002), $R_{\rm in} = 6$, $h_x = 10$, $\mathcal{A} = 0.3$ and a constant X-ray luminosity of $L_x = 3 \times 10^{42}$ erg s^{-1} (Smith and Vaughan, 2007). The points with error bars are the measured centroid lags (of the light curves shown in Figure 4.2 versus the X-rays) as a function of wavelength.

The irradiated disc model, with parameter values as taken from literature, does not provide a particularly good fit to the measured lags. Note however that the radial dependence of both terms in Eqn. 4.5 scale as $R^{-3/4}$ for large radii. 'Large' here implies $R \gg R_{\rm in}$ and $R \gg h_x$, since we can write $\cos\theta = h_x/(h_x^2 + R^2)^{1/2}$. In combination with the peak of the emission scaling as $T \propto \lambda^{-1}$, and writing the delay between different bands as $\tau = R/c$, we obtain the well-known relationship between the wavelength of the emission and the expected delay between variations in different bands, $\tau \propto \lambda^{4/3}$. Clearly, in regions where the large radius assumptions break down the relationship between the lag and the emitted wavelength is somewhat modified (see also Gaskell, 2008). Nevertheless, this simple argument shows that an irradiated disc is also expected to follow a $\tau \propto \lambda^{4/3}$ relationship at large radii. I therefore additionally show a simple $\lambda^{4/3}$ model in Figure 4.9 (dotted line), fitted to the measured lags via an arbitrary scaling constant. The error bars are too large to constrain the model tightly, but the increase in the delay with wavelength is consistent with a $\lambda^{4/3}$ dependence, as expected for reprocessing by an accretion disc. The factor of ∼2 difference between the two curves can easily be accounted for within the uncertainties on the model parameters.

To construct a model light curve, the emitted flux as a function of time may be computed by integrating the emission over all light travel time delays τ to different parts of the disc, and throughout all disc radii,

$$f_\lambda(t) = \int_{R_{\rm in}}^{R_{\rm out}} dR \int_{\tau_1}^{\tau_2} A(R,\tau) B_\lambda(T(R, t-\tau))\, d\tau \tag{4.6}$$

where $T(R,t)$ is given by Eqn. 4.5. A is an area function obtained by considering the effect of the disc inclination on the distance between the X-ray source and the disc (see Berkley et al., 2000), and $B_\lambda(T)$ is the Planck function. $R_{\rm out}$ is a large value, appropriate for the outer edge of the disc.

I allow the inner disc radius $R_{\rm in}$, the accretion rate $\dot{m} = \dot{M}/\dot{M}_{\rm Edd}$, height of the X-ray source h_x and disc inclination θ to vary, to find the parameters best describing the observed optical light curve. The mass was fixed at the reverberation-mapped value, $1.91 \times 10^6 M_\odot$ (Peterson et al., 2004).

Figure 4.10 shows the observed optical light curve compared to a typical model reprocessed light curve. Due to the short light-travel time to the optical emitting region, the rapid variability of the X-rays is preserved in the model light curves and we find that a range of input parameter values produce nearly identical model light curves. As expected, the model reprocessed light curve is highly correlated with the X-ray light curve, trailing it by $0.4 - 0.8$ days, depending on the input parameters.

This is a very simple model, which assumes the X-rays to be emitted by a compact source located on the symmetry axis of the system, at a height h_x above the disc surface. In reality, it is more likely that the X-rays come from an extended corona. The compact source model used here may be viewed as a first order approximation of the centroid of such a corona. This simplified model is a sufficient approximation in this case, as h_x is much smaller than the radius where most of the optical emission is coming from. The break in the X-ray power spectrum, which is thought to be associated with the inner edge of the disc, corresponds to the dynamical time-scale at $35R_g$, or the viscous time-scale of a thick disc ($\alpha = 0.1, H/R \sim 0.5$) at $3R_g$, so the bulk of the X-rays are probably emitted within a radius smaller than, or comparable to this. Using Comptonization models Uttley et al. (2000) estimate the size of the emission region to be $< 20R_g$. Integrating the blackbody emission through the disc, 95% of the V band emission is found to originate from outside a radius of $400R_g$. From this distance, even an extended corona would resemble a point source, making a more detailed model of the X-ray

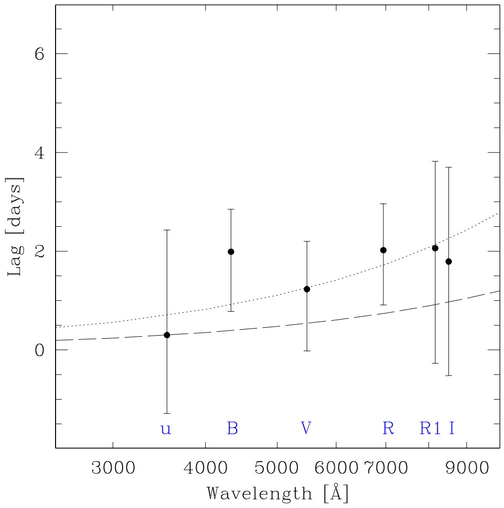

Figure 4.9: Centroid lags measured from the CCFs between the X-rays and optical colours. The dashed line shows the predicted lags from an irradiated accretion disc model for parameters appropriate to NGC 4051 (see text). The dotted line is a simple $\lambda^{4/3}$ model, fitted to the data by an arbitrary scaling constant.

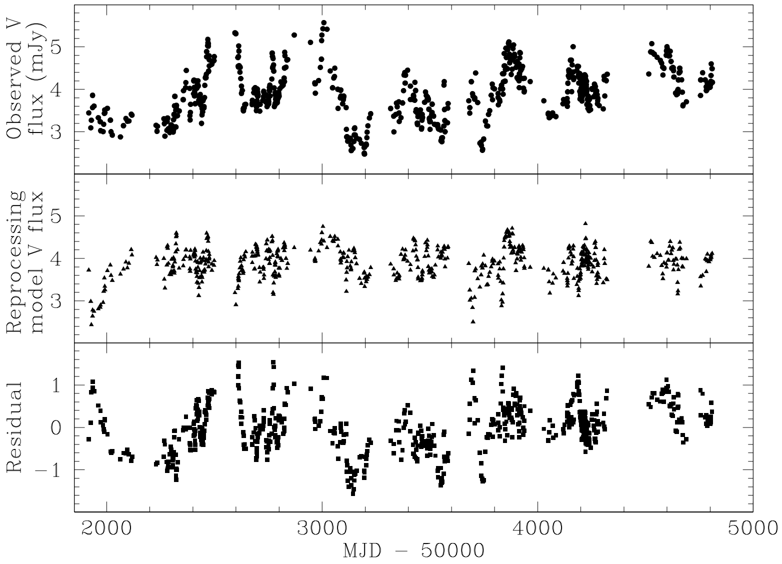

Figure 4.10: *Top panel:* Galaxy-subtracted V band light curve. *Middle panel:* Best-fit model reprocessed V band light curve, using the observed X-ray light curve as input. *Bottom panel:* Residual variations in the optical light curve after the reprocessed component has been removed.

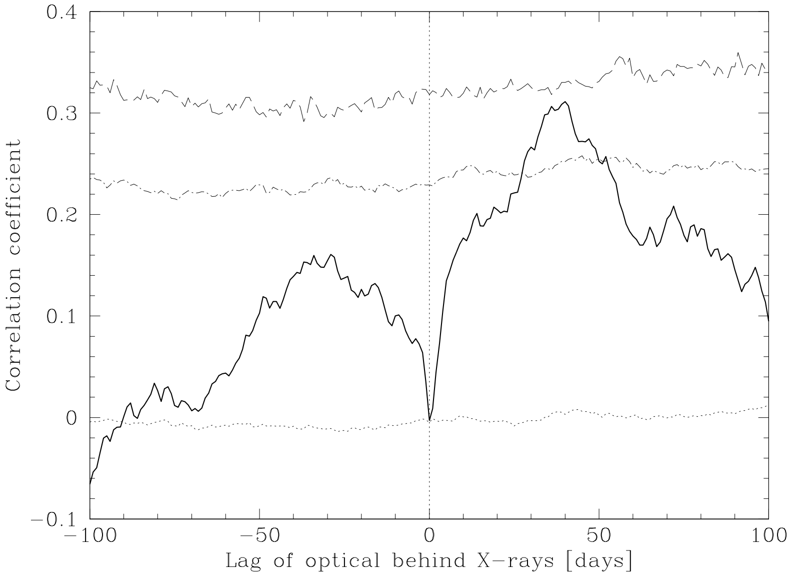

Figure 4.11: Cross correlation of the reprocessing-subtracted residual light curve with the X-rays. The ~ 0 day peak is removed entirely from the CCF, leaving only the longer time-scale correlation peak. The horizontal lines are the 50% (dotted), 95% (dot-dashed) and 99% (dashed) significance levels. The peak is significant at 98.4%.

source unnecessary.

Reprocessing by a standard, thin disc appears to describe the observed lag and the short time-scale (∼days) variations of the optical light curve well, but it fails to simultaneously reproduce the larger amplitude flares on time-scales of ∼months. Closer inspection of the light curves in Figure 4.1 confirms that it is these larger amplitude fluctuations which lag the X-rays by ~ 40 days (see e.g. MJD ~ 50750, 52500 and 53700 for obvious examples). Attempting to isolate these variations, I show in the bottom panel of Figure 4.10, the residual of subtracting the reprocessing model light curve from the observed light curve. Cross correlation of the X-rays with this "residual curve" yields the CCF shown in Figure 4.11. As the model light curve is very well correlated with the X-rays at near 0 days, subtracting it removes this correlation peak entirely from the CCF (the correlation at this lag drops to zero). Isolating the second peak this way, allows for a more precise measurement of the lag it corresponds to. The peak is found to be at $38.9^{+1.2}_{-3.3}$ days, and the 85% centroid at $38.5^{+2.5}_{-2.2}$ days. I calculate the significance of the correlation as before, by cross-correlating random red noise light curves with the difference light curve. It is found to be significant at 98.4% confidence. It is therefore clear that reprocessing by a flat disc can only account for the short lags in the light curve and that the second peak must be produced by optical emission from a structure further out.

4.6 Discussion

The detection of two significant peaks in the X-ray/optical correlation function suggest that the optical variability originates from more than one location in the system, or through more than one process. In the previous section I discussed the correlation at short lags in terms of reprocessing by an accretion disc. I showed that this model can only reproduce the short time-scale variations in the light curve, and that the second peak must be the result of optical emission coming from beyond the disc and BLR.

In this section I will investigate the origin of the second peak in the correlation function. The lag is found to be consistent with the light travel time to the inner radius of the dust torus in this source, so I investigate the possibility of optical emission originating from the torus. Firstly I will consider reprocessing of X-rays by the dust, and secondly the dust reflecting optical light from the accretion disc.

4.6.1 Second peak in the CCF – optical emission from the torus?

The standard model of AGN holds that the disc and BLR is surrounded by a large molecular torus. It is now widely accepted that the infrared emission from AGN is the result of reprocessing of high energy radiation by hot dust in the torus (e.g. Glass, 2004). I investigate here whether it is possible that the second peak detected in the correlation function could be the result of optical emission coming from the torus.

4.6.1.1 Distance to the torus

The inner radius of the dust distribution is set by the dust sublimation radius, inside which the flux from the central source will destroy the dust particles. Detailed radiative transfer calculations (Nenkova et al., 2008a) places this radius at

$$r_{\rm subl} = 0.4 \left(\frac{L}{10^{45}\,{\rm erg\ s^{-1}}}\right)^{0.5} \left(\frac{T}{1500\,{\rm K}}\right)^{-2.6} \quad {\rm pc.} \tag{4.7}$$

where T is the dust temperature and L the UV-optical luminosity.

Where adequate data exist, the optical to near-infrared delays show reasonable agreement with this model. Using both their own monitoring data as well as results from literature, Oknyanskij and Horne (2001), Minezaki et al. (2004) and Suganuma et al. (2006) show that the optical-to-infrared lag is proportional to $L^{0.5}$ over a range of luminosities.

The exact temperature at which the dust in the torus sublimates is not well known, as it depends on the composition of the dust. The dust is generally assumed to be a mixture of graphite and silicate particles, with sublimation temperatures in the range 1500–2000 K. The emission from hot dust at the inner edge of the torus is therefore expected to peak in the K band. As graphite can survive higher temperatures, it is assumed that the dust at the inner edge will mostly consist of graphite grains.

Gaskell (2007) pointed out that at such high temperatures, there must be a small, yet significant amount of optical emission coming from the torus as well, as part of the Wien tail of the $\sim$1500–2000 K emission. He proposed that the increase in time delay measured between the optical bands could be the result of contamination by the additional optical emission coming from large radii. Optical emission coming from the torus will of course also be delayed with respect to the X-rays, by the same amount as the infrared emission. This will cause an asymmetry in the X-ray–optical correlation function, or, if the signal is strong enough, another peak may be seen, corresponding to the light travel time to the inner edge of the torus. The dust recombination time-scale is expected to be long compared to the sublimation time-scale (Koshida et al., 2009), so that the inner edge of the torus is determined by the largest of the X-ray/UV flares. Any variations we see in the emitted flux is then probably due to temperature variations of the dust (below the sublimation temperature), rather than a change of the torus inner radius.

The $H - K$ colour measured for NGC 4051 by Suganuma et al. (2006), corresponds to a blackbody temperature of approximately 1600 K, so I adopt this value as the temperature of the dust in this source. I scale the ionizing X-ray-UV-optical luminosity ($\sim$13.6 eV–13.6 keV), estimated by Ogle et al. (2004), to a distance of 15.2 Mpc, giving $L_{\rm ion} = 1.1 \times 10^{43}$ erg s^{-1}. The sublimation radius (Eqn. 4.7) of NGC 4051 is then $r_{\rm subl} = 42.2$ light-days. The position of the second peak in our correlation function agrees well with this value. I note, however, that the V-to-K lag found by Suganuma et al. (2006) is only $\sim$ 20 light-days. This may be expected if the disc V band emission is contaminated by optical emission from large radii (such as the torus), as this will shift the peak of the V vs. K CCF to shorter lags.

Several studies (Peterson et al., 2000; Kaspi et al., 2000; Peterson et al., 2004) measure the location of the BLR to be at ~ 6 light-days, placing even the smallest estimates of the torus well outside the disc and BLR.

4.6.1.2 Energetics

Detailed models of AGN dust tori (e.g. Nenkova et al. 2008a, Nenkova et al. 2008b) take account of the fact that the torus probably consist of clumpy material rather than a smooth distribution of dust. One effect the clumps has is to cause a steep radial temperature gradient in the torus, as optically thick clouds closer to the source can shield those further away from direct irradiation. It also takes into account the diffuse heating of clumps by each other. Such a detailed analysis is beyond the scope of this investigation, but as we are mainly interested in the hottest dust here, a simplified approach may be sufficient to determine whether it is energetically possible to get the 1–2 mJy V band flux required to explain the large amplitude optical fluctuations, from the torus.

A blackbody at 1600 K emits roughly 16% of its total emission in the K band, and only 0.04% in the Wien tail at V band wavelengths. The fraction of V band emission decreases very rapidly as the dust temperature decreases, so no significant contribution to the optical emission is expected from further into the torus. I will assume that the optical emission is identified with the inner edge of the dust distribution only, where the hottest dust is located. For simplicity, I also assume a sharp boundary, although the transition is most likely a gradual one, given the difference in sublimation temperatures of different dust particles. I follow the prescription of Barvainis (1987) to calculate the luminosity emitted by the dust. I assume a grain radius of $a = 0.05\mu$m and infrared (K band) absorption efficiency $Q_{\rm abs} = 0.058$. The luminosity of a single grain is given by $L_\nu^{\rm gr} = 4\pi a^2\, \pi Q_\nu\, B_\nu(T)$ erg s^{-1} Hz^{-1}, where B_ν is the Planck spectrum of a grain at temperature T. The K band spectral luminosity of a graphite grain at $T = 1600$ K is then $L_K^{\rm gr} = 3.6 \times 10^{-17}$ erg s^{-1} Hz^{-1}. The average galaxy-subtracted K band flux measured by Suganuma et al. (2006) is 31 mJy, which corresponds to a total K band luminosity of $L_K = 8.6 \times 10^{27}$ erg s^{-1} Hz^{-1}. Hence the total number of hot dust grains is $N \sim 2.4 \times 10^{44}$. For UV-optical radiation, the absorption efficiency is $Q_{\rm abs} \sim 1$ for grains of this size (Wickramasinghe et al., 1974). The optical emission of a grain at 1600 K is $L_V^{\rm gr} = 1.9 \times 10^{-19}$ erg s^{-1} Hz^{-1}. If we assume the same number of grains to be emitting this optical emission (i.e. only the hottest dust) then the total V band luminosity we may expect from the torus is

$L_V = 4.4 \times 10^{25}$ erg s^{-1} Hz^{-1}. This translates to an observed flux of only 0.16 mJy, which is an order of magnitude smaller than required to explain the additional variability in the observed V band light curve.

One of the main uncertainties in this model is the dust composition, as there is no guarantee that dust in the vicinity of the active nucleus will be the same as dust found in molecular clouds. The temperature of the grains is determined by the balance between UV absorption and infrared emission, which vary with grain size and type. This, in turn, affects the sublimation temperature. If we allow the dust temperature to increase to 1800 K (which is still within range of the sublimation temperature of graphite), the emitted luminosity per grain increases to $L_V^{\mathrm{gr}} = 1.15 \times 10^{-18}$ erg s^{-1} Hz^{-1}, and the additional flux observed in the V band to 1.1 mJy. Such an increase in the temperature the dust particles can sustain will of course move the sublimation radius inwards as well, to a distance of $r_{\mathrm{subl}} = 31.1$ light-days. This is within the 1σ error of the peak measured on the X-ray–optical CCF (Figure 4.6), and within 2σ of the peak measured from the CCF calculated using residual light curve (Figure 4.11). The uncertainty on L_{ion} would also allow a factor of $\sim$2 change in the sublimation radius. A similar analysis for the other optical bands, using $T = 1800$ K and the appropriate absorption efficiencies, yields $u = 0.004$, $B = 0.08$, $R = 5.8$, $R1 = 13.2$ and $I = 16.6$ mJy. For wavelengths R and longer, the reprocessing model therefore predicts a higher flux to come from the torus alone than the total galaxy-subtracted flux we measure. The measured fluxes in these bands must however include a significant contribution from the disc as well, as their correlation functions with the X-rays (Fig. 4.8) all display a significant peak at short lags.

For increasing wavelength, the torus reprocessing model naturally predicts an increase in the amount of reprocessed flux originating in the torus, as the redder bands include a larger fraction of the total flux emitted by the dust. The data do not appear to support such an increase, so it is unlikely that all the additional optical flux result from dust reprocessing. The possibility that some of the optical emission in this source is originating in the dust torus, can nevertheless not be excluded.

4.6.1.3 Optical reflection

In this section I will consider the reflection of optical light by the torus. Apart from the illumination by the central source, the torus will also receive UV and optical light from the accretion disc. The dust absorbs energy at these wavelengths very efficiently, so some of this reprocessed optical emission will be absorbed by the dust and contribute to the variable heating of the torus, as discussed in the previous section. Depending on the solid angle subtended by the torus at the optically-emitting part of the disc, some of the optical emission may also be elastically scattered and reflected by the torus. The efficiency of reflection is strongly geometry dependent, so I will limit this discussion to a qualitative description of the main observable results expected. Reflection from different geometries have been considered by Goosmann and Gaskell (2007) in the development of their Monte Carlo polarization code STOKES.

Most of the UV/optical illumination will be relatively steady, or will vary on the very long (years) viscous time-scales on which the intrinsic emission from the disc will vary. However, as I have already shown, a small fraction of the optical illumination, resulting from reprocessing of X-rays by the accretion disc, will follow the pattern of the X-ray variations. As the optically-emitting region is about a light-day away from the central X-ray source, the torus will see optical emission which broadly follows the X-ray emission, but which is smoothed on a time-scale of a day or two relative to the X-ray variability pattern.

The component of the optical emission illuminating the torus which has a phase relationship with the X-rays (so that it causes a peak in the CCF), must have arisen from reprocessing of X-rays in the disc. The amount of scattered light depends on the solid angle the torus subtends at the optically emitting part of the disc, so for large solid angles, the elastically scattered optical photons may produce a noticeable contribution to the optical variations, and will lag the X-rays by about 40 days. Dust models by Draine (2003) suggest that the scattering albedo (scattering cross section as a fraction of the total extinction cross section) of Milky Way type dust may be as high as 0.5–0.8, for different dust compositions. Dust in AGN probably consists of larger grains (smaller grains are evaporated by the intense radiation field), so the albedo is uncertain, but it may still be high enough for the scattered light to contribute significantly to the observed optical radiation.

Reflection models are supported by spectropolarimetric studies which are used to detect the broad line region in Seyfert 2 galaxies, such as NGC 1068, through polarized light. In these systems, the continuum source and BLR clouds are hidden from our view by the molecular torus, but their emission is scattered into our line of sight by warm electrons and dust lying outside the torus opening, polarizing the light. In Seyfert 1 galaxies, however, the optical polarization position angle is generally observed to be parallel to the radio axis (which is assumed to be the system axis), suggesting that the scattering medium has an equatorial geometry, perhaps a ring of material co-planar with with accretion disc (Smith et al., 2002, 2004), or the inner edge of the torus (Cohen and Martel, 2002). The optical continuum polarization in NGC 4051, as measured by Smith et al. (2002), is low however. They find 0.5 per cent of the optical continuum at 7000Å to be polarized, amounting to a mere ~ 0.05 mJy. It is also not clear to what extent this is intrinsic to the source or whether the measurement is contaminated by foreground interstellar polarization. If intrinsic, the position angle of the polarization is approximately parallel to the radio axis, suggesting that the scattering occurs in the equatorial region. Unfortunately their polarization observation was made during a time for which we do not have optical monitoring data available, so I cannot comment on the general optical behaviour of the source at that time.

There is also evidence for diffuse continuum emission and reprocessing by the BLR, as well as reflection by the broad line clouds (Korista and Ferland, 1998; Korista and Goad, 2001; Arévalo et al., 2009) in some Seyfert galaxies. Though, as mentioned before, any lags associated with the BLR (~6 days for NGC 4051) are likely to be much shorter than those associated with the torus.

As an aside, we note that the high energy emission may also be reflected by the torus. X-ray spectra show evidence of X-ray reflection by high density gas in the form of the "Compton bump" and the Fe Kα fluorescence line at 6.4 keV. This line is thought to originate in the accretion disc, and is therefore expected to be broadened by relativistic Doppler motions. Broad Fe lines like this are seen in X-ray spectra, but the line is found to have a narrow component as well, which is associated with reflection by distant, optically thick material such as the molecular torus (e.g. Nandra et al., 2007).

Neither the reprocessing nor the scattering model can on its own fully account for the optical flux causing the second peak in the correlation function, but it is possible that either or both may contribute to the optical emission observed from the system. Overall I conclude that there are many possible sources of optical emission in the inner parts of AGN but all those associated with the torus, albeit reprocessing or simple reflection, will give more or less the same lag. Our current data are not suited to constrain these models further, so a more detailed discussion is beyond the scope of this thesis.

4.6.2 The complex optical variability in NGC 4051

Shemmer et al. (2003) find that part of the optical emission leads the X-ray variations by approximately 2 days, contrary to what is seen here (see Table 4.3). As was shown in previous sections, there is more than one effect contributing to the optical variations in this source. Variations on time-scales longer than, or similar to, their 3 month monitoring period may cause asymmetries in the correlation function and hence a centroid at negative lags. Shemmer et al. (2003) interpret their result as a combination of reprocessing and longer time-scale variations, similar to what we find over much longer time-scales. I note that the peak of their cross-correlation function is consistent with the peak lag we find here, ~ 1 day.

In red noise time series, such as the X-ray and optical light curves used here, peaks and troughs may sometimes line up even if the light curves are not really correlated, producing spurious peaks in the CCF. I believe that the second peak we measure in the CCF here, is not simply due to statistical fluctuations like these, as it is present in most of the individual segments used to calculate the final CCFs. If this was an effect only due to a random correlation in a red noise process, we would expect to see it in, e.g. only one of the segments' CCFs. We note that the peak does shift between $\sim 30 - 50$ days in the CCFs of the different segments. The probability that the peak is due to such statistical fluctuations was assessed through Monte Carlo simulations in Section 4.4, and was found to be 1.6%.

So far I have interpreted the second peak in the CCF only in terms of a light crossing time-scale. Other time-scales of interest are the dynamical (Kepler) time-scale, and the viscous time-scale, on which we expect accretion rate fluctuations to propagate through the disc. A lag of the optical variations behind the X-rays, as seen here, would require such fluctuations to be propagating outwards through the disc for this time-scale to be relevant. A viscous time-scale of 40 days corresponds to $R = 50R_g$ in a moderately thin, optically thick disc ($H/R \sim 0.1$, $\alpha_{\rm disc} = 0.1$), or to $R = 440R_g$, in a geometrically thick disc ($H/R \sim 0.5$, $\alpha_{\rm disc} = 0.1$). $R = 50R_g$ lies well within the Far- to Extreme UV emitting part of the disc; less than 0.5% of the optical emission come from within this radius. $R = 440R_g$ contains approximately 6% of the optical emission. Enhanced emission due to viscous instability in this region could therefore only cause a $\sim 6\%$ variation in the light curve. This translates to a flux variation of 0.2 mJy, which is not enough to explain the variations seen in the light curve. As an orbital time-scale, 40 days corresponds to the radius which contains 69% of the V band emission, but is is difficult to associate an orbital time-scale with a lag between the emission in different wavebands, as seen here.

If this is indeed optical emission from the torus, why has this not been seen in other sources? NGC 4051 is a low mass, low luminosity system, which means that it is physically smaller than higher mass AGN. Lags between the optical and near-infrared suggest that dust sublimation radii in most sources are several tens to hundreds of days, but here it is only ∼20–40 days. The optical emission from the torus will be a very weak signal, so long enough light curves are necessary to include several cycles of the correlated variations to produce a significant peak in the CCF. For example, calculating the CCF using only half of the V band data, decreases the significance of the second peak in Figure 4.6 to 96.3%, or to below 95% if only a quarter of the light curve is used.

More importantly, in low mass systems the V band emission originating in the torus is probably a larger fraction of the total V band emission emitted by the system, than it is in more massive systems. This is due to the variation in disc temperature with black hole mass. For a standard disc (e.g. Frank et al., 2002) with characteristic disc spectrum $F_\nu \propto \nu^{1/3}$, the integrated emission in the V band, as a fraction f of the total disc emission, is $f \propto (\nu/\nu_{\rm p})^{4/3}$, where $\nu_{\rm p}$ is the frequency at the peak of the emission. This frequency depends on the disc temperature through Wien's law, $T \propto \nu_{\rm p}$, so that for fixed ν, the fraction $f \propto \nu_{\rm p}^{-4/3} \propto T^{-4/3}$. T here refers to the temperature of the hottest part of the disc, near the inner edge. For an accretion disc around a black hole of mass M and fractional accretion rate $\dot{m}$, the temperature varies as $T \propto M^{-1/4}\dot{m}^{1/4}$, so that $f \propto M^{1/3}\dot{m}^{-1/3}$. For example, for a fixed accretion rate of $\dot{m} = 0.10$, a disc around a $10^8 M_\odot$ black hole emits 1.9% of its total luminosity at V band wavelengths, but for a $10^6 M_\odot$ black hole the disc is hotter, the bulk of the energy is emitted at bluer wavelengths and the fraction of the total emission emitted at V band wavelengths decreases to 0.4%. On the contrary, the torus in all sources is expected to be at approximately the same temperature (as its inner radius and temperature is determined by dust sublimation). Assuming that the torus covers the same solid angle in all sources, and using the fact that the radius scales $L^{0.5}$, the area of the inner face of the torus and hence the reprocessed emission scale as L. The V band emission originating in the torus also scales as L if the temperature is constant; it is a constant fraction of the total torus emission. Comparing this constant fraction with the V band emission originating in the disc, the torus contributes a larger *fraction* to the total V band emission in the $10^6 M_\odot$ source than it does in the $10^8 M_\odot$ source. In more massive systems the V band emission is dominated by the disc, so the weak optical emission from the torus will be very hard to isolate.

Long-term multicolour optical and infrared monitoring of NGC 4051 is needed to reliably measure the inner radius of the dust torus and the possible contribution of the disc to the near-infrared (e.g. Tomita et al., 2006). Detailed modelling of the torus emission, taking into account both the geometry of the system as well as the dust albedo and emission properties, is also necessary to properly assess the contribution this could have to the optical emission observed.

4.7 Summary

In this chapter, I have presented a 12.6 year 3–10 keV X-ray light curve from our ongoing long term X-ray monitoring program on *RXTE*, along with concurrent optical monitoring light curves. I combined the V band data from four different telescopes with archival 5100Å continuum data, to construct an optical light curve spanning the same length in time. I also include light curves in the u, B, R, $R1$ and I optical bands, each of length between 3.6 and 6.6 years in time.

I find both the X-ray and optical emission to be highly variable, but find the amplitude of the optical emission to be smaller than that of the X-rays, even after subtracting the contaminating host galaxy flux falling inside the aperture. The power spectra show that the optical variability power is lower than the X-rays on all time-scales probed. With the current data, the optical PSD is best described by an unbroken power law of slope $\alpha = 1.4$, which is much steeper than the low frequency slope of the X-ray PSD ($\alpha_L = 1.1$). This suggests that the variations in the different bands do not have a common origin or that they are not related in a simple way. This issue is considered again in Chapter 5, Section 5.3, and will be addressed in more detail in a future study.

I measured the galaxy flux inside the $15''$ aperture by decomposition of the optical images, and find the measured fluxes to agree well with a template spectrum of a similar non-active spiral galaxy.

The cross-correlation function between the optical light curve and the X-rays displays two statistically significant peaks. The strongest peak corresponds to the optical variations lagging the X-rays by $1.2^{+1.0}_{-0.3}$ days. This time-scale is consistent with the light travel time to the optical emitting region of the accretion disc, and points to X-ray reprocessing as the source of the fast optical variations. The delays measured between other optical colours and the X-rays are also consistent with this interpretation. However, using a reprocessing model, I find that all the optical variability cannot be accounted for this way. Reprocessing appears to describe the small amplitude, fast variations well, but it fails to reproduce the larger amplitude variations on time-scales of months–years that are also seen in the light curve.

The second significant peak in the CCF is at an optical lag of $38.8^{+2.9}_{-8.4}$ days behind the X-rays. By subtracting a model reprocessed light curve from the observed optical light curve and recalculating the cross-correlation, this peak can be constrained more precisely, viz. $38.9^{+1.2}_{-3.3}$ days. Interpreting this as a light travel time, the corresponding radius is consistent with the dust sublimation radius in this AGN, which is a theoretical estimate of the inner radius of the dust torus.

As such, I have investigated the origin of the additional optical emission, both in terms of a weak optical contribution from X-ray reprocessing by the dust, and in terms of reflection of optical light from the disc by the dust. Neither process can on its own explain the origin of the second peak in the CCF of NGC 4051, but it remains possible that both these processes may contribute to the optical emission observed. Detailed modelling of the dust emission properties at optical wavelengths, as well as further optical polarimetry will be required to thoroughly test this hypothesis.

In general, the weak (though significant) short time-scale correlation reported here is consistent with a model where the strength of the correlation is determined by the mass of the central black hole and disc accretion rate (Uttley et al., 2003). When scaled in terms of gravitational radius, a standard accretion disc (e.g. Shakura and Sunyaev, 1973) around a smaller mass black hole, with a given accretion rate, is hotter. The optical emitting region will therefore be further away from the centre and the viscous time scale here will be much longer than near the centre, where the X-rays are emitted. The variations in the different bands may therefore be expected to vary incoherently, weakening the strength of the correlation. Furthermore, the mass-dependence of the disc temperature may also explain why an optical contribution from the torus is detected in this source and not in more massive systems: the cooler discs around more massive systems will emit most of their luminosity at optical wavelengths, dominating over the weak optical signal from the torus. In low mass systems with hotter discs, such as NGC 4051, the peak of the disc emission is shifted to shorter wavelengths, decreasing the fraction of the emission emitted at V band wavelengths and hence increasing the possibility of detecting optical emission from the torus.

5 Investigating the mass dependence of optical variability

5.1 Introduction

Variability studies provide a powerful probe into the size and physical processes at work in the inner regions of AGN, but the origin of the optical continuum variations has long been debated. It is known that the characteristic variability time-scales of a system are largely determined by the mass of the central black hole (through the gravitational radius $R_g = GM/c^2$), so our targets for long term monitoring were selected to span a range in black hole mass in order to identify properties which depend on this parameter. All figures, tables and results in this chapter are arranged in order of increasing black hole mass, so that patterns which emerge may be identified more easily.

Table 5.1 lists the basic properties of all the galaxies considered in this chapter. Note that it does not form a statistically representative sample — the selection was based on galaxies which were already part of our X-ray monitoring program on *RXTE*. Detailed analysis of the light curves of Mrk 79 and NGC 4051 were presented in Chapters 3 and 4, and in this chapter I will consider the sample of seven Seyfert galaxies as a whole.

I start by summarising and comparing the variability properties of the X-ray and optical light curves and then compare the optical power spectral densities with those of the X-rays. The optical power spectra points to a common, or

Table 5.1: Basic properties of the Seyfert galaxies monitored for an optical/X-ray correlation, arranged in order of increasing mass

Target	R.A. (2000.0)	Dec. (2000.0)	z	Mass ($\times 10^6 M_\odot$)	Ref.	$L_{\rm bol}/L_{\rm Edd}$
NGC 4051	$12^{\rm h}03^{\rm m}09.6^{\rm s}$	$+44^\circ 31' 53''$	0.002	1.6	*a*	0.22
NGC 4593	12 39 39.4	−05 20 39	0.009	9.8	*b*	0.10
NGC 7469	23 03 15.6	+08 52 26	0.016	12	*c*	1.24
Mrk 110	09 25 12.9	+52 17 11	0.035	18	*d*	0.23
NGC 3227	10 23 30.6	+19 51 54	0.003	42	*c*	0.01
Mrk 79	07 42 32.8	+48 48 35	0.022	52	*c*	0.06
NGC 5548	14 17 59.5	+25 08 12	0.017	65	*e*	0.08

Position and redshift (z) from NASA/IPAC Extragalactic Database (NED), $L_{\rm bol}/L_{\rm Edd}$ from Woo and Urry (2002), Mass references: (*a*) Denney et al. (2009), (*b*) Denney et al. (2006), (*c*) Peterson et al. (2004), (*d*) Kollatschny (2003), (*e*) Bentz et al. (2007).

closely related, origin of the X-ray and optical variability in five out of the seven galaxies studied here, and cross-correlation analysis finds reprocessing of X-rays to be a key contributor to the optical variations of all the targets.

Finally, I consider the relationship between the strength of the X-ray/optical correlation with disc temperature, mass and accretion rate, to determine the underlying reason for the wide range of variability behaviour observed in Seyfert galaxies.

5.2 Properties of the light curves

5.2.1 The monitoring sample

Our parallel X-ray and optical monitoring programs, along with the optical monitoring by our collaborators and published data, have yielded concurrent X-ray and optical light curves of between 4 and 13 years in length.

With the exception of NGC 3227 and Mrk 79, all the X-ray light curves presented in this chapter are 3–10 keV light curves produced as described in Chapter 2. The NGC 3227 light curve is a 2–10 keV light curve made by D. Summons as part of his thesis work (Summons, 2008). This light curve includes all the data of this source available in the *RXTE* archive, so it was not updated for use in this work. The data were reduced in exactly the same way, and the flux obtained by integrating the best fit power law between 2 and 10 keV. The Mrk 79 light curve, as already mentioned in Chapter 3, is also a 2–10 keV light curve. It was made by P. Uttley, following the same method. I show here only the part of the X-ray light curves overlapping in time with the optical monitoring.

The optical light curves are the result of the combined observational efforts of many observers. The light curves obtained at different observatories were combined in a least squares fashion and scaled to a reference data set (see Section 2.2.3). For most of the light curves, I chose the MAGNUM light curve as the reference dataset, as it was made using the smallest aperture, so includes the least amount of host galaxy flux in the aperture. NGC 4051 was scaled to the 15″ CrAO light curve, for consistency with the colour light curves presented in Section 4.2.3. The NGC 4593 light curve consists mostly of LT data, with only a few points from other telescopes, so everything was scaled to match the 18″ LT light curve.

The origin of each of the light curves, observation dates and other observational characteristics are summarised in Table 5.2. The light curves are shown in Figures 5.1a–g. The V band light curves of Mrk 79 and NGC 4051 which were shown in Chapters 3 and 4 are repeated here, for convenience of the reader.

Table 5.2: Details of the full sample of optical light curves (top) and X-ray light curves (bottom)

Target	Telescope(s)[‡]	Observation dates (MJD)	Aperture diam./ energy range	N	T (d)	$\Delta t_{\rm mean}$ (d)	$\Delta t_{\rm med}$ (d)
Optical:							
NGC 4051	A	50095.0 – 51022.6	$5'' \times 7.5''$	126	927	7.42	3.15
NGC 4051[†]	L,F,M,C	51917.3 – 54811.1	$15''$	629	2894	4.61	1.94
NGC 4593	L,F,D	53385.2 – 54978.9	$18''$	301	1594	5.31	1.92
NGC 7469	M,C	52075.5 – 54331.4	$8.''3$	298	2256	7.59	2.97
Mrk 110[†]	M	52676.3 – 53881.3	$8.''3$	49	1205	25.1	15.8
Mrk 110	L	54515.3 – 54978.9	$8.''3$	112	464	4.18	1.92
NGC 3227	L,M,C	52226.6 – 54282.3	$8.''3$	328	2055	6.29	2.99
Mrk 79	L,F,M,C,N,U	52283.5 – 54250.9	$8.''3$	461	1967	4.28	1.63
NGC 5548	L,M,C,A	50008.2 – 54671.0	$8.''3$	1386	4663	3.40	1.03
X-ray:							
NGC 4051	*RXTE*	50196.5 – 54811.3	3–10 keV	1811	4615	2.55	1.96
NGC 4593	*RXTE*	53314.0 – 54943.0	3–10 keV	794	1629	2.05	1.38
NGC 7469	*RXTE*	52737.0 – 54349.6	3–10 keV	323	1613	5.08	4.27
Mrk 110	*RXTE*	53433.4 – 54999.1	3–10 keV	999	1566	1.57	1.89
NGC 3227	*RXTE*	52000.6 – 53709.0	2–10 keV	603	1708	2.84	2.03
Mrk 79	*RXTE*	52720.4 – 54495.6	2–10 keV	975	1775	1.82	1.89
NGC 5548	*RXTE*	50196.7 – 54346.7	3–10 keV	958	4150	4.34	4.23

[‡] L = Liverpool Telescope, F = Faulkes Telescope North, M = MAGNUM Telescope, C = 0.7-m CrAO Telescope, N = 0.4-m University of Nebraska Telescope, U = 0.6-m telescope at Mt. Maidanak Observatory, Uzbekistan, A = public AGN Watch data, D = Denney et al. (2006).

[†] Light curves for which there is no overlap between the segments are listed separately.

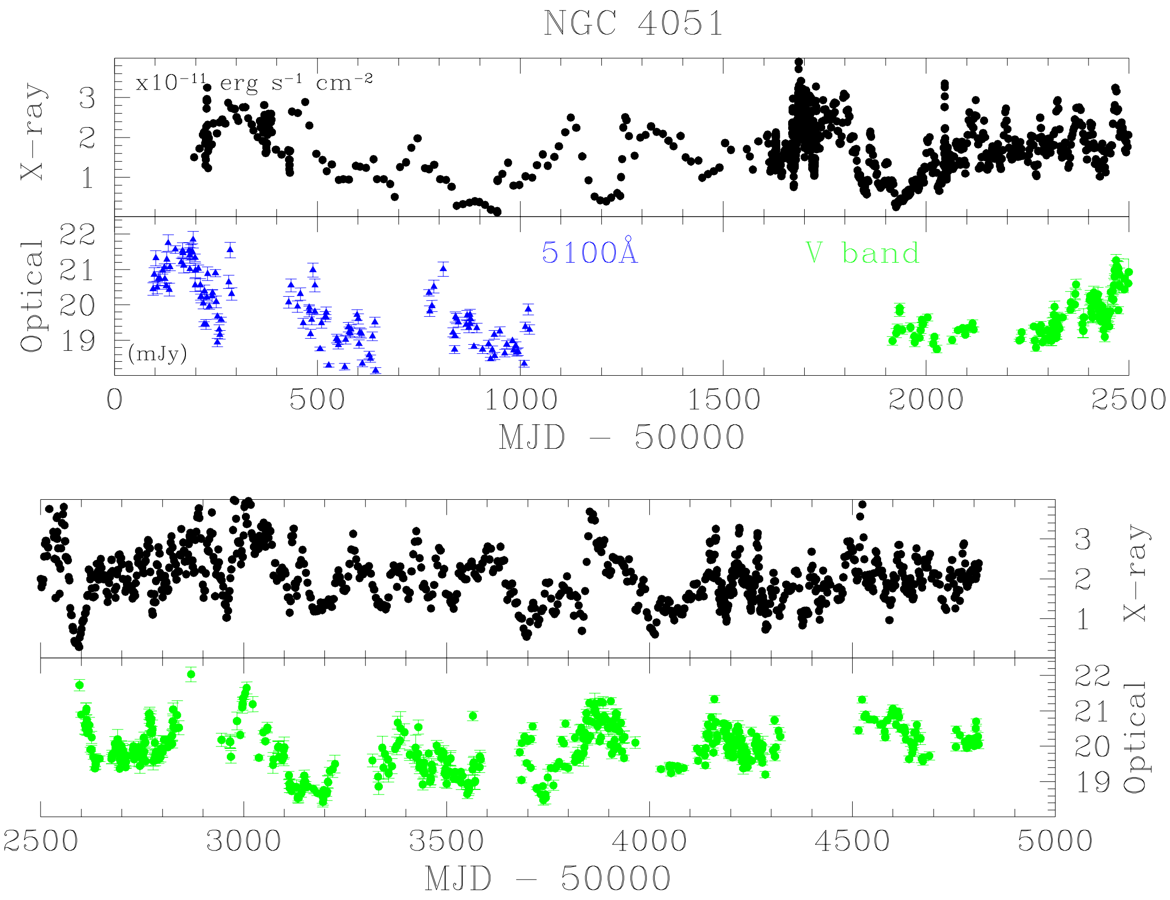

Figure 5.1a: $3 - 10$ keV X-ray (top panel) and V band (bottom panel) light curves of NGC 4051. The X-ray light curve is smoothed with a 4 point (~8 day) boxcar, to highlight the variations on time-scales similar to that of the optical light curves. The X-ray light curve is in units of 10^{-11} erg s^{-1} cm^{-2}, the optical light curve is in mJy. Optical points plotted in green were obtained through a V band filter at various observatories. Points in blue are the 5100Å continuum fluxes from the AGN Watch program, converted to mJy. Host galaxy flux has not been subtracted.

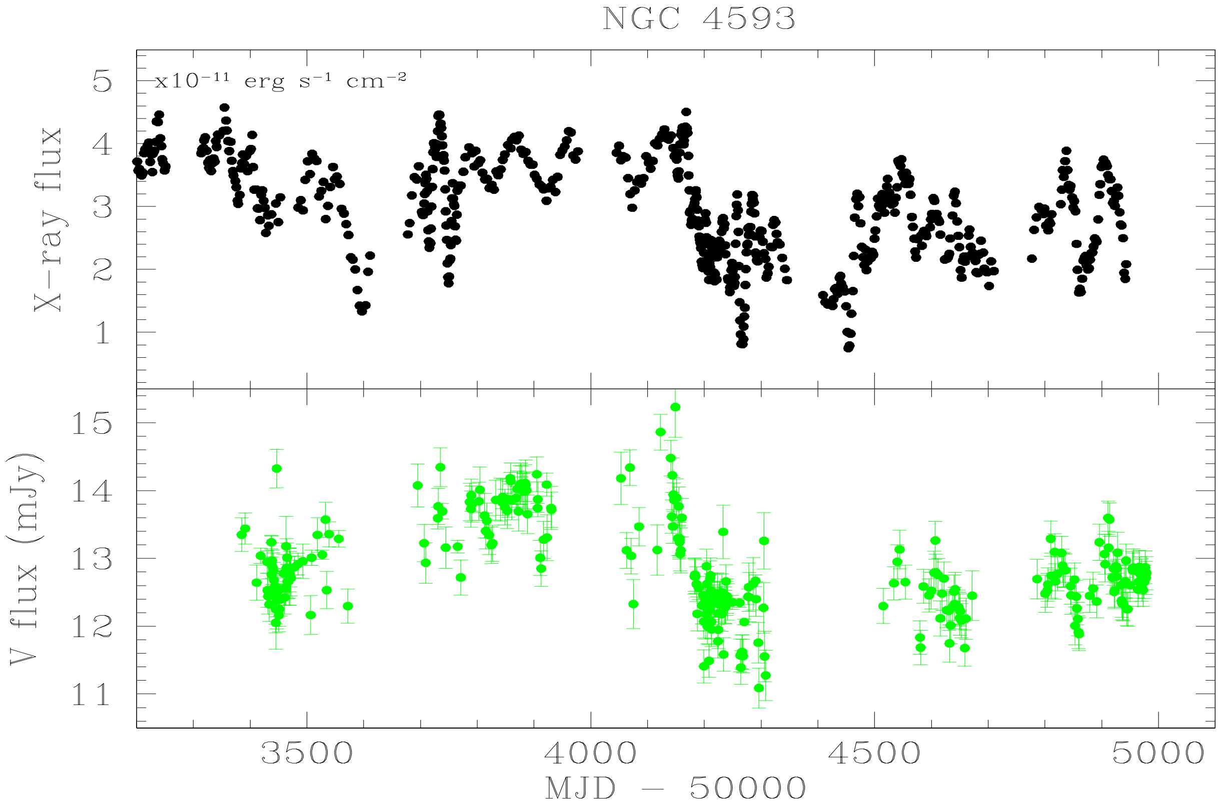

Figure 5.1b: 3 – 10 keV X-ray (top panel) and V band (bottom panel) light curves of NGC 4593. The X-ray light curve is smoothed with a 4 point (∼8 day) boxcar, to highlight the variations on time-scales similar to that of the optical light curves. The X-ray light curve is in units of 10^{-11} erg s^{-1} cm^{-2}, the optical light curve is in mJy. No host galaxy contribution has been subtracted.

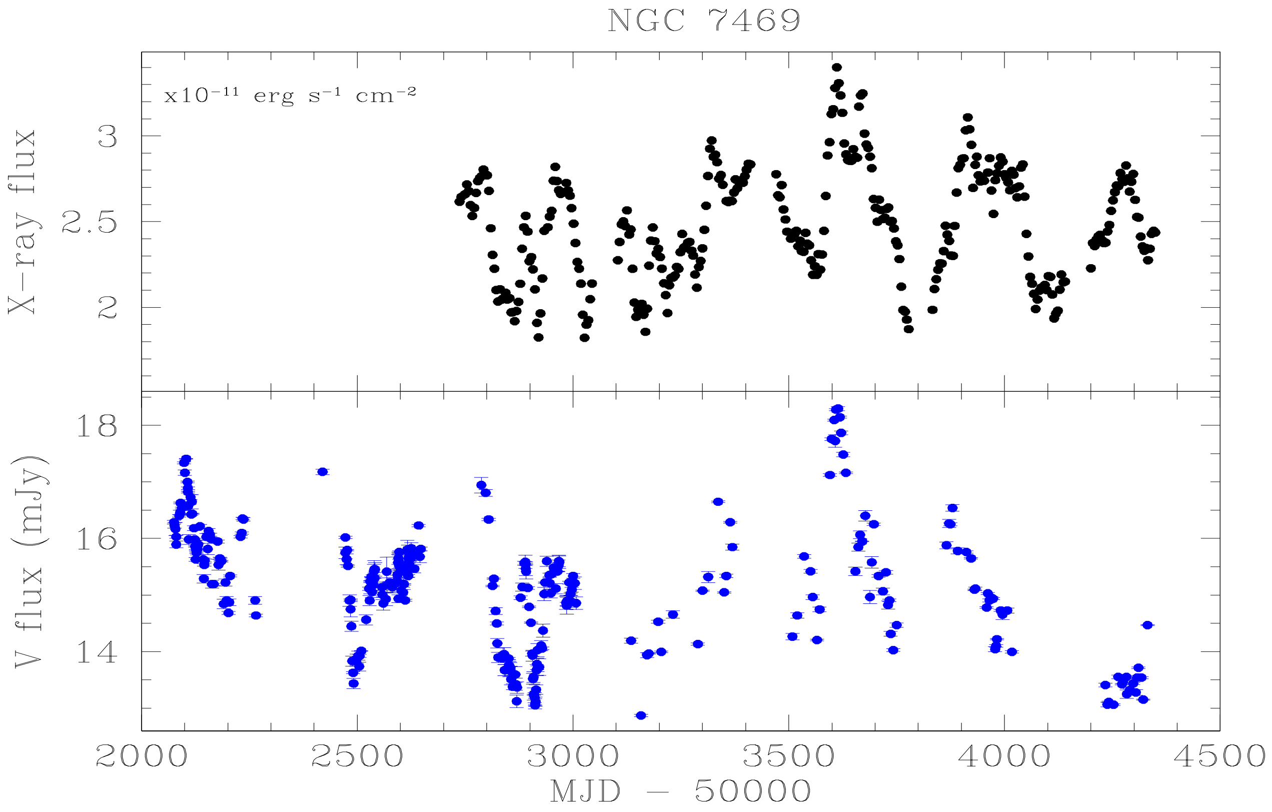

Figure 5.1c: $3-10$ keV X-ray (top panel) and V band (bottom panel) light curves of NGC 7469. The X-ray light curve is smoothed with a 4 point (∼8 day) boxcar, to highlight the variations on time-scales similar to that of the optical light curves. The X-ray light curve is in units of 10^{-11} erg s^{-1} cm^{-2}, the optical light curve is in mJy. No host galaxy contribution has been subtracted.

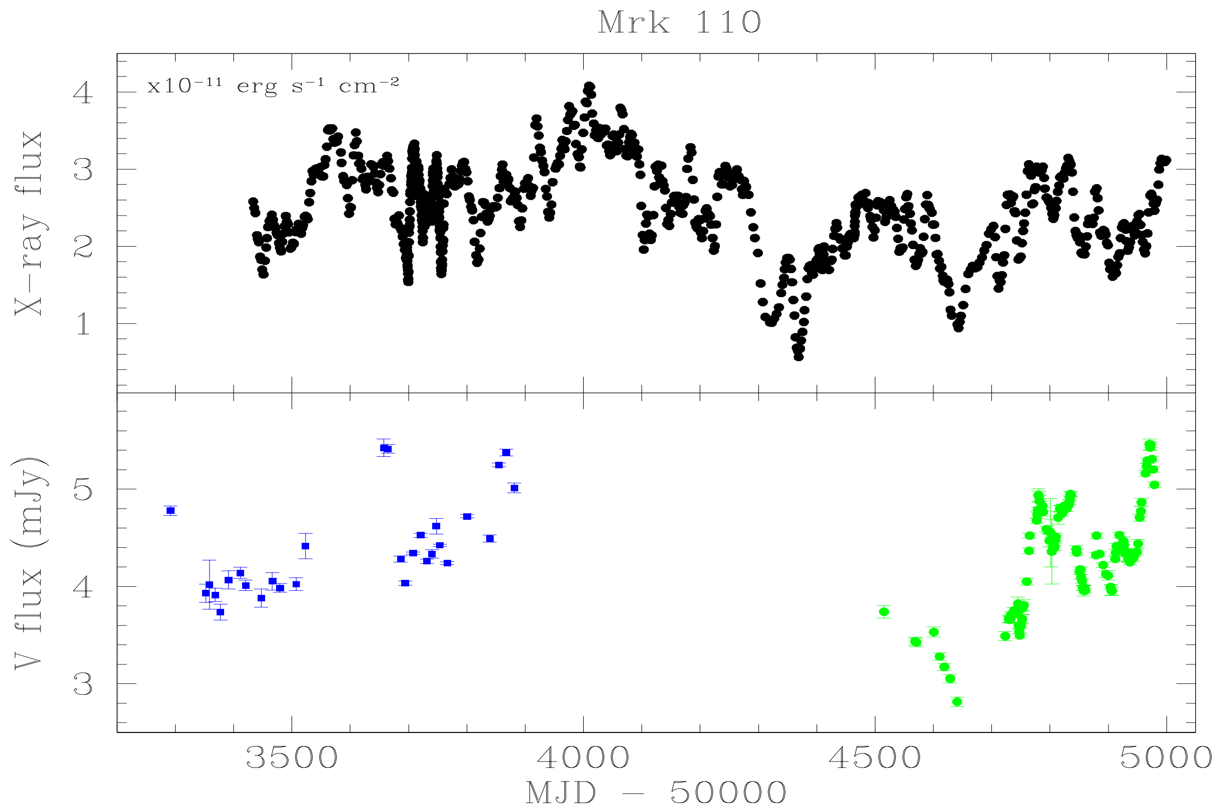

Figure 5.1d: 3 – 10 keV X-ray (top panel) and *V* band (bottom panel) light curves of Mrk 110. The X-ray light curve is smoothed with a 4 point (~8 day) boxcar, to highlight the variations on time-scales similar to that of the optical light curves. The X-ray light curve is in units of 10^{-11} erg s^{-1} cm^{-2}, the optical light curve is in mJy. No host galaxy contribution has been subtracted. Optical points plotted in blue were obtained with the MAGNUM telescope, while the green points are from the Liverpool Telescope. Although the same filter and photometric aperture was used, the relative calibration between the two light curves is uncertain. This does not affect the cross-correlation analysis, however (see text).

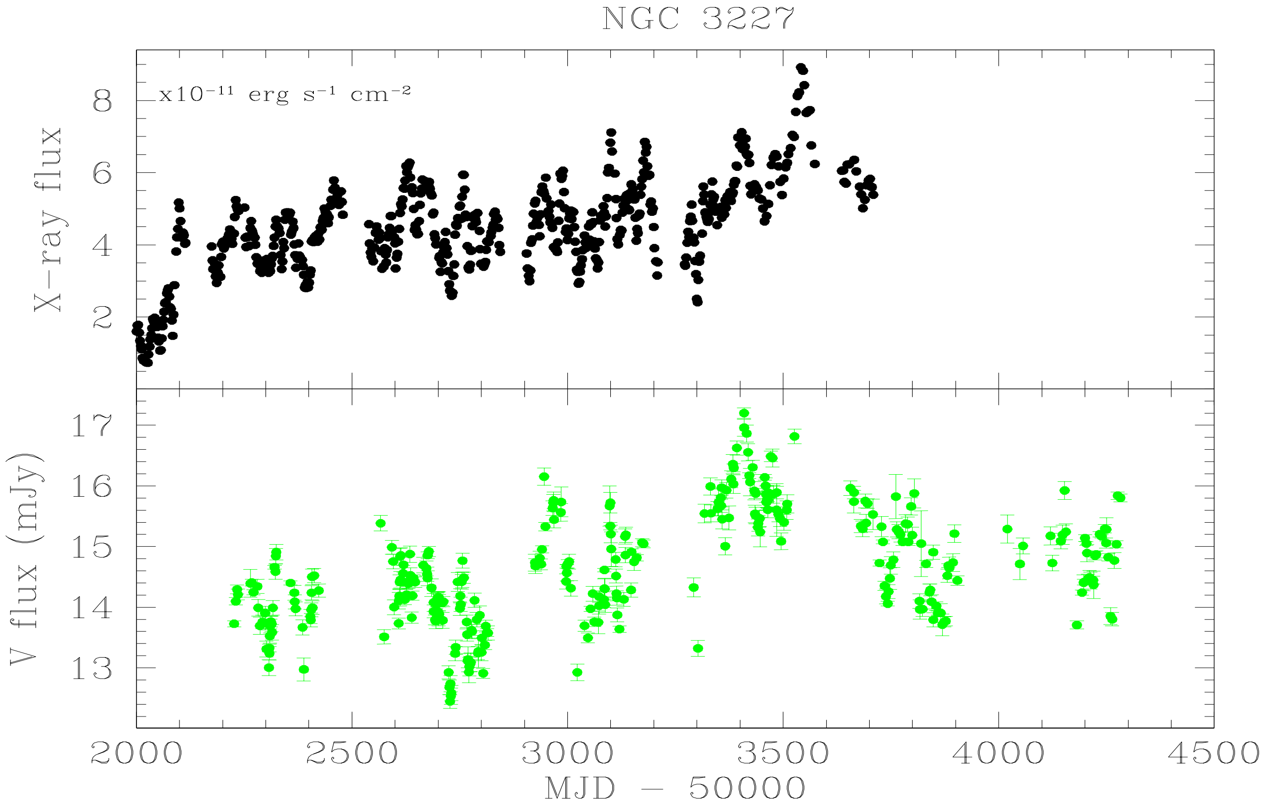

Figure 5.1e: $2 - 10$ keV X-ray (top panel) and V band (bottom panel) light curves of NGC 3227. The X-ray light curve is smoothed with a 4 point (∼8 day) boxcar, to highlight the variations on time-scales similar to that of the optical light curves. The X-ray light curve is in units of 10^{-11} erg s^{-1} cm^{-2}, the optical light curve is in mJy. No host galaxy contribution has been subtracted.

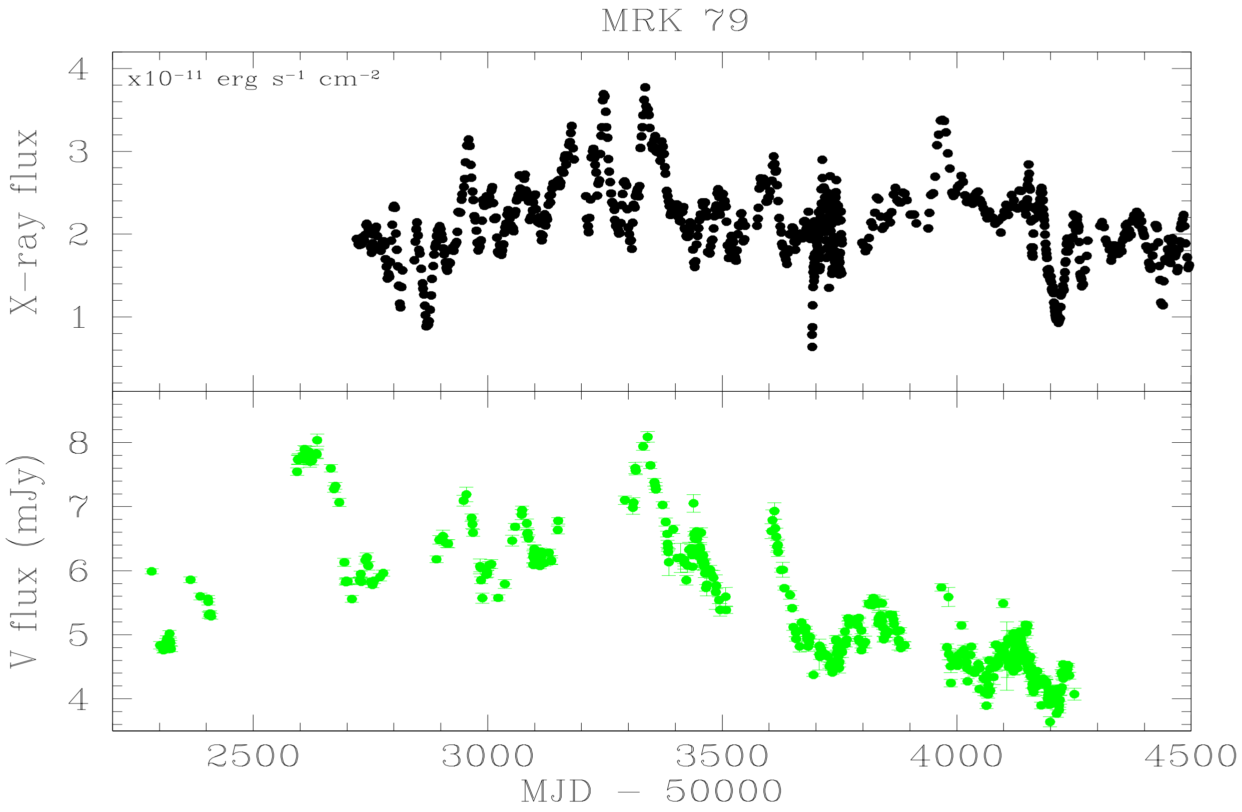

Figure 5.1f: 2 – 10 keV X-ray (top panel) and V band (bottom panel) light curves of Mrk 79. The X-ray light curve is smoothed with a 6 point (∼12 day) boxcar, to highlight the variations on time-scales similar to that of the optical light curves. The X-ray light curve is in units of 10^{-11} erg s^{-1} cm^{-2}, the optical light curve is in mJy. No host galaxy contribution has been subtracted.

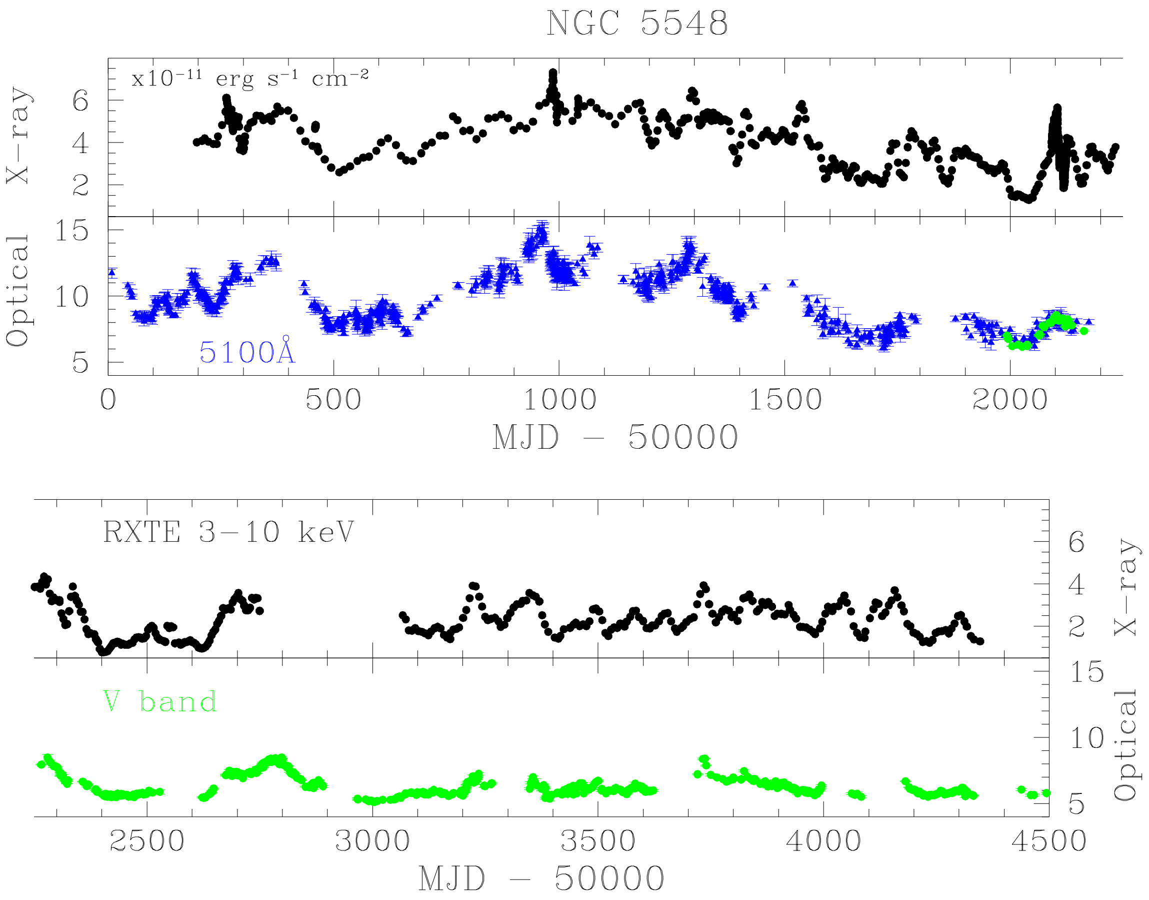

Figure 5.1g: 3 – 10 keV X-ray (top panel) and *V* band (bottom panel) light curves of NGC 5548. The X-ray light curve is smoothed with a 4 point (∼8 day) boxcar, to highlight the variations on time-scales similar to that of the optical light curves. The X-ray light curve is in units of 10^{-11} erg s^{-1} cm^{-2}, the optical light curve is in mJy. Optical points plotted in green were obtained through a *V* band filter at various observatories. Points in blue are the 5100Å continuum fluxes from the AGN Watch program, converted to mJy and scaled to match the *V* band light curve. No host galaxy contribution has been subtracted.

5.2.2 Host galaxy contribution

In order to compare the variability amplitudes of the optical light curves with the X-rays and with each other, the constant host galaxy flux falling inside the aperture must be accounted for.

The galaxy fitting routine GALFIT (Peng et al., 2002) allows one to fit a combination of analytic functions to the surface brightness profile of a galaxy. In this way, the contribution from the galaxy and the nucleus may be separated, and their relative contribution to the flux in the photometric aperture determined. The signal-to-noise of our individual images from the Liverpool Telescope was generally too low to for a multi-component model to converge. Instead, I stacked 5–14 images of each source to produce a single, high signal-to-noise image to use for the decomposition. To account for the variability of the nucleus, I selected only images from which the same flux was measured in the light curve and which were taken under similar seeing conditions. Consequently, I could measure the flux of the galaxy and nucleus directly from the stacked image.

I fitted the images of NGC 3227, 4051, and 5548 with an exponential disc, a de Vaucouleur bulge profile and a PSF, representing the nucleus. Suitable stars in the field of view were used as a model for the PSF. Mrk 110 appears pointlike in our images, with only a very small contribution from the bulge ($< 10\%$) and no visible disc, so it was fitted with a de Vaucouleur bulge and PSF only. The foreground star which blends into the wings of the galaxy profile was removed by fitting another PSF at its position. For Mrk 79 and NGC 4593 I followed Bentz et al. (2009) and fitted a PSF, exponential disc, an 'inner' Sersic bulge and an 'outer' Sersic bulge to account for the bar. This combination produced a lower χ^2 fit than fitting a de Vaucouleur profile together with the PSF and disc. The resulting flux of Mrk 79 also agrees remarkably well with the flux estimated from the *HST* image in Section 3.2.3. Note that NGC 7469 was not part of the LT monitoring program, so its host galaxy flux was taken from literature (Suganuma et al., 2006). I subtracted the bulge and the disc components of the best fit model from the image and then measured the residual nuclear flux on the image, using exactly the same photometry and background apertures used to construct the light curves. The difference between this value, and the flux measured from the original image, was taken to be the galaxy contribution. I also inverted the measurement, subtracting only the nucleus from the image and measuring the remaining flux on the nucleus-free image. The difference between the two results was found to be negligible, presumably because the spatial resolution of these images is too low to

Table 5.3: V band host galaxy flux in the photometric aperture

Target	Aperture	f_g (mJy)	Ref.
NGC 4051	15″	16	This work
NGC 4593	18″	11	This work
NGC 7469	8″.3	8.6	Suganuma et al. (2006)
Mrk 110	8″.3	0.73	This work
NGC 3227	8″.3	8.6	Y. Sakata, private comm.
Mrk 79	8″.3	2.6	This work
NGC 5548	8″.3	4.2	Y. Sakata, private comm.

resolve any finer structure of the galaxies.

All these measurements were done using LT data, so I measured the galaxy flux using the same size aperture as originally selected to make the LT light curves (Chapter 2). To convert this flux to the effective flux in the 8″.3 aperture used to construct the MAGNUM light curves, I applied the same scaling I calculated to convert the LT light curve to match the MAGNUM light curve (Eqn. 2.3). This resulted in a host galaxy flux estimate of 4.3 and 9.3 mJy for NGC 5548 and NGC 3227, respectively. The MAGNUM group had independently estimated the host galaxy flux inside the 8″.3 aperture, using both MAGNUM data and high resolution *HST* images, and found 4.2 and 8.6 mJy for these two galaxies (T. Minezaki, Y. Sakata, private communication). As both both these galaxies' light curves contain more data from the MAGNUM Telescope than from the LT, I will adopt their estimate of the host galaxy flux in the analysis that follows, as it was measured directly from the data. Nevertheless, the close agreement between my scaled estimates and the direct estimates obtained by Y. Sakata, shows the validity of my approach. Similarly, scaling my estimate of the galaxy flux for NGC 4051 to the 8″.3 aperture of the MAGNUM light curve, yields 8.3 mJy, which compares very well to their estimate of 8.0 – 8.6 mJy (Y. Sakata, in preparation, Suganuma et al. 2006). The photometric error on the galaxy fluxes are $\sim 1\%$, but this does not include an error due to the brightness profile fitting. The galaxy contribution for all sources (in the relevant photometric aperture) are listed in Table 5.3.

5.2.3 Variability statistics

As before (Sections 3.2.3 and 4.2.6) I calculate the fractional variability (Eqn. 4.1) and its error (Eqn. 4.2) of the X-ray and galaxy-subtracted optical light curves, to compare the intrinsic variability of the AGN in the sample. It is shown in Table 5.4, along with the mean of each light curve and the ratio of the maximum to minimum flux. The error on F_{var} quoted in Table 5.4 allows for a 15% error on the galaxy flux, which appears to be the approximate precision of the galaxy decomposition method. (See, e.g. Chapter 4, section 4.2.5 for measurements of NGC 4051, and Suganuma et al. 2006, who used the same technique).

The fractional variability of the optical light curves is less than that of the X-rays in all but the two most massive sources. Hence reprocessing alone cannot be the only contributor to the optical variations in these sources. The case of Mrk 79 has already been discussed in detail in Chapter 3 — the large amplitude, long time-scale optical variations may be attributed to a variation of the disc accretion rate or a change in the geometry of the system. The optical variations of NGC 5548 appear to be larger in the first half of the light curve (Figures 5.1g and 5.2). It is this part of the light curve which is largely responsible for the high value of fractional variability of the optical light curve. NGC 5548 appears to have gone into a state of low optical luminosity (see also Bentz et al., 2007) and has displayed less variability in the past few years than in the earlier half of the monitoring. The normalised light curves shown in Figure 5.2 illustrates this clearly. Calculating the fractional variability of the optical light curve using only data past MJD 52966, (i.e. after the gap in the optical light curve) yields $F_{\mathrm{var}} = 23.5 \pm 2.5$. The corresponding part of the X-ray light curve is also slightly less variable, with $F_{\mathrm{var}} = 34.8 \pm 0.3$, though the decrease is much less dramatic than for the optical light curve.

There does not appear to be a simple relationship between the mass of the black hole and the fractional variability in either the X-rays or the optical in this sample. Note that in NGC 4593, which hosts one of the least massive black holes, the X-ray and optical variability are of comparable magnitude. The large errors on $f_{\mathrm{max}}/f_{\mathrm{min}}$ for the X-ray light curves of NGC 3227 and NGC 4051, and the optical light curve of NGC 4593, result from relatively large flux errors on near-zero fluxes.

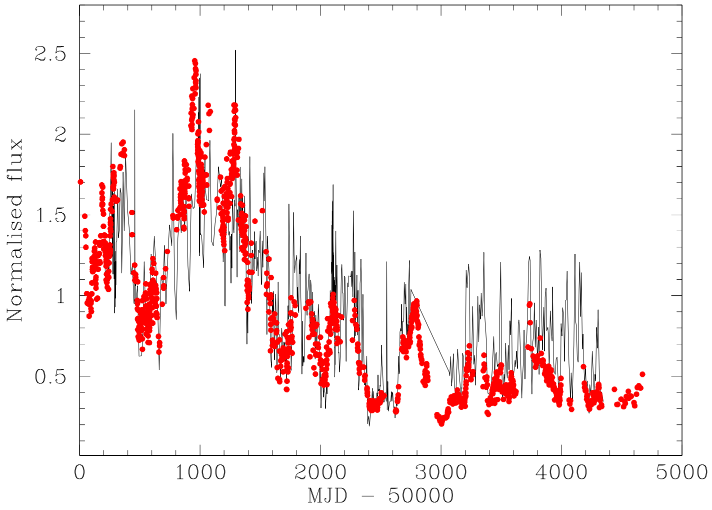

Figure 5.2: The X-ray (black line) and optical (red dots) light curves of NGC 5548, each normalised to its mean flux to show the relative variability amplitudes. In the first part of the monitoring the long time-scale optical amplitude exceeds the X-ray variations, but the opposite is true for the latter half of the light curves. The good correlation between variations on time-scales of days–months is clear. 4.2 mJy host galaxy flux was subtracted from the optical light curve before normalising.

Table 5.4: Variability statistics of the X-ray and optical light curves

	Mean flux*		$F_{\rm var}$(%)		$f_{\rm max}/f_{\rm min}$	
Target	X-ray	Optical	X-ray	Optical	X-ray	Optical
NGC 4051	1.9 ± 1.0	4.1 ± 0.6	48.8 ± 0.8	15.4 ± 3.1	89.0 ± 26.5	2.5 ± 1.6
NGC 4593	3.0 ± 1.0	2.1 ± 0.7	34.6 ± 0.1	30.8 ± 3.1	13.8 ± 2.7	13.6 ± 12.3
NGC 7469	2.5 ± 0.6	6.5 ± 1.1	21.9 ± 1.8	16.7 ± 0.4	4.5 ± 0.4	2.3 ± 0.1
Mrk 110$^{\natural}$	2.5 ± 0.6	3.6 ± 0.5	23.6 ± 0.1	14.8 ± 0.8	14.5 ± 8.1	2.3 ± 0.1
NGC 3227	4.5 ± 1.7	7.8 ± 0.9	36.0 ± 0.5	11.8 ± 0.3	19.7 ± 25.4	2.1 ± 0.1
Mrk 79	2.1 ± 0.6	2.8 ± 1.0	27.3 ± 0.2	36.0 ± 1.9	10.5 ± 1.8	5.0 ± 0.4
NGC 5548	3.5 ± 1.4	4.1 ± 2.4	41.1 ± 0.1	56.9 ± 2.8	13.2 ± 1.8	12.0 ± 0.7

*X-ray flux in units of $\times 10^{-11}$erg s^{-1} cm^{-2}, optical in mJy. Galaxy flux has been subtracted from the optical light curves.

$^{\natural}$Using the LT data only for the optical, as the relative calibration between segments is uncertain.

5.3 Optical power spectra

The power spectral density (PSD) of a variable source describes the frequency distribution of the variability power in the light curve. It is a commonly used technique used to characterise and describe the aperiodic brightness fluctuations displayed by AGN and black hole X-ray binary systems (Uttley et al., 2002; Markowitz et al., 2003; van der Klis, 1994). X-ray light curves of AGN generally display variability with a characteristic power spectral shape: the variability power $P(\nu)$ increases towards lower frequencies in a power law fashion, i.e. $P(\nu) \propto \nu^{-\alpha}$, with $\alpha \sim 2$. At a frequency characteristic of each system, the power law breaks and flattens to a slope of $\alpha \sim 1$ (e.g. M$^{\rm c}$Hardy et al., 2004; Summons, 2008). The PSD is calculated as the modulus-squared of the Discrete Fourier Transform (DFT) at discrete frequencies ν sampled by the time series

$$|F_N(\nu)\,|^2 = \left(\sum_{i=1}^{N} f(t_i)\cos(2\pi\nu t_i)\right)^2 + \left(\sum_{i=1}^{N} f(t_i)\sin(2\pi\nu t_i)\right)^2 \tag{5.1}$$

where $f(t_i)$ represent the flux observations in the light curve at times t_i and N the number of data points in the light curve. The frequencies used in the calculation are equally spaced between the minimum frequency contained in the data, $\nu_{\rm min} = 1/T$, where T is the total time span of the light curve, and the Nyquist frequency $\nu_{\rm Nyq} = N/2T$. To obtain the power $P(\nu)$, equation 5.1 is multiplied by the root-mean-squared (rms) normalisation,

$$P(\nu) = \frac{2T}{\mu^2 N^2}|F_N(\nu)\,|^2 \tag{5.2}$$

where μ is the mean flux level of the light curve (e.g. Uttley et al., 2002).

Uttley et al. (2002) introduced a Monte Carlo fitting technique, PSRESP, to calculate the true underlying power spectrum of the X-ray light curves, in the presence of distortions due to uneven sampling and possibly long gaps in the light curves. Summons (2008) has made various improvements to the code, e.g. to correct for the effects of red noise leak[1] and aliasing[2]. The method simulates a

---

[1] Variability in the light curve at frequencies lower than the minimum frequency $\nu_{\rm min} = 1/T$ sampled by the data adds additional long time-scale power across the whole power spectrum. The amount depends on the amount of low frequency variability present in the light curve at frequencies lower than $\nu_{\rm min}$

[2] Variations on time-scales shorter than the average sampling interval artificially adds high frequency power to the power spectrum. This power appears to be “reflected” about the Nyquist frequency into the measured PSD (see e.g. van der Klis, 1989).

large number of light curves from a given power spectral shape and applies the same sampling, rebinning and interpolation to each as for the observed light curve. Calculating and averaging the power spectrum from each of these simulated light curves therefore gives the (average) shape of the known, underlying power law model, distorted by the sampling function of the observed light curve. This realisation of the underlying power spectrum is usually referred to as the *periodogram*. The spread of the different periodogram realisations can be used to estimate the error on the periodogram shape, so that it may be compared directly with the periodogram calculated from the observed light curve. Stepping through a series of different underlying power law shapes, the best fit to the observed periodogram may be determined. The technique is described in detail by Uttley et al. (2002).

Here I use the current version of PSRESP to calculate the optical PSD of the sources in our sample. The large amplitudes of some of the optical light curves noticed in Section 5.2 suggests that there is considerable long time-scale power in the optical light curves, and that especially the effects of red noise leak has to be accounted for when measuring the optical power spectra of AGN. PSRESP incorporates the effect of red noise leak by generating the simulated the light curves 300 times longer than the observed light curve, so that the low frequency variations are folded in before the simulated light curve is sampled like the observed light curve.

In order to extract the maximum frequency information from the light curves, I bin them to produce a long (months) and medium (days) time-scale light curve. The long time-scale light curve is binned in bins of approximately half the width of the longest gap in the light curve, so that at most one interpolated point is added in the gap. The most frequently sampled section of the light curve is extracted as the medium time-scale light curve, typically binned in bins of 1 – 2 days width. AGN are not generally found to vary in the optical on time-scales less than a day (e.g. Done et al., 1990; Klimek et al., 2004), although NGC 4051 does show some evidence for variability on these time-scales. The microvariability light curve of NGC 4051 from the Klimek et al. (2004) study is included here as a short time-scale light curve, to constrain the high frequency end of the PSD further in this source. The final periodogram is binned logarithmically in bins of width 1.5ν, where ν is the frequency at the start of the bin. Throughout this work I will adopt the ν vs. νP_ν form of the PSD plots. In this representation, a power law of slope $\alpha = 1$ appears as a horizontal line, so deviations from such a slope is more noticeable and the bend or break frequency becomes more pronounced.

Table 5.5: Best-fit unbroken power law slope α and model acceptance probability p for the optical PSDs

Target	α	p
NGC 4051	$1.4^{+0.6}_{-0.2}$	0.795
NGC 4593	$1.5^{+0.5}_{-0.5}$	0.649
NGC 7469	$2.1^{+0.4}_{-0.4}$	0.205
Mrk 110	$3.8^{+0.2}_{-2.0}$	0.489
NGC 3227	$1.6^{+0.9}_{-0.2}$	0.599
Mrk 79	$2.3^{+0.2}_{-0.5}$	0.521
NGC 5548	$1.9^{+0.2}_{-0.1}$	0.484

5.3.1 Unbroken power law model

I start by fitting an unbroken power law model

$$P(\nu) = A\nu^{-\alpha} \tag{5.3}$$

to the power spectra, allowing the slope α and the normalisation A to vary. The best fit for each of the targets is shown in Figure 5.3, and the best-fit slopes and model acceptance probability is given in Table 5.5. The acceptance probability is the probability that the observed PSD is a realisation of the underlying power law model. The errors on α indicate the parameter values for which the acceptance probability drops below 10 per cent. The large error bars on some of the points at high frequencies is the result of unfolding the observed PSDs of the effects of Poisson noise.

The optical power spectra of all the targets in this sample are consistent with a simple unbroken power law model. The acceptance probabilities are high enough that a more complex model will not describe the data significantly better, when the extra free parameters of such a model are taken into account.

The previous observation that the long term optical variability amplitudes are larger in the optical than in the X-rays in NGC 5548 and Mrk 79, and of similar magnitude in NGC 4593, is clearly evident from the PSDs as well. The optical PSD on these three targets intersect and exceed the X-ray PSD at low frequencies. The steep slopes of the best-fit unbroken power law to e.g. Mrk 110 and NGC 3227 suggest that the same may happen in those sources. However, further monitoring

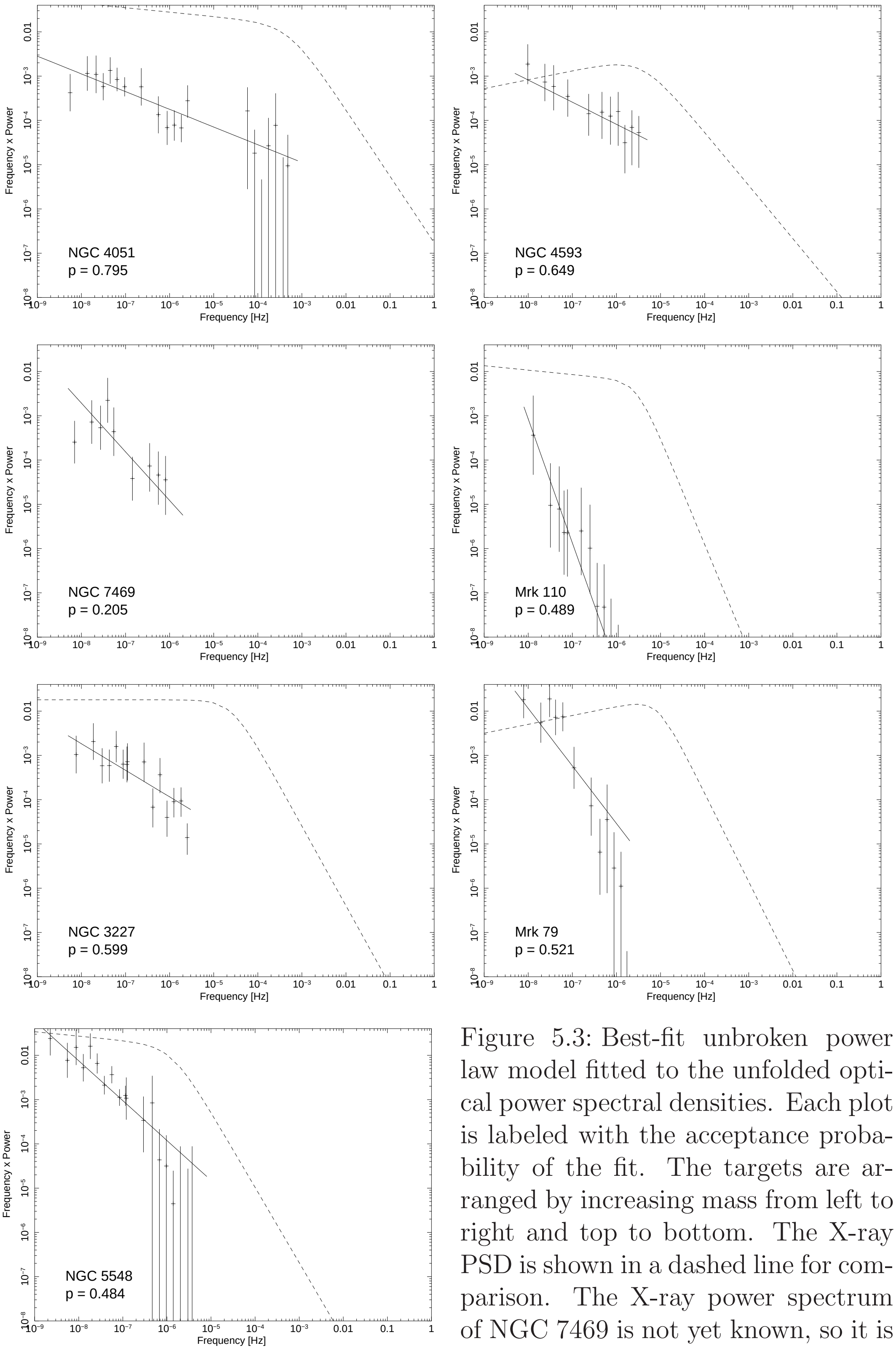

Figure 5.3: Best-fit unbroken power law model fitted to the unfolded optical power spectral densities. Each plot is labeled with the acceptance probability of the fit. The targets are arranged by increasing mass from left to right and top to bottom. The X-ray PSD is shown in a dashed line for comparison. The X-ray power spectrum of NGC 7469 is not yet known, so it is not shown here.

would be required to extend the frequency range of the light curves and confirm this conjecture.

The best-fit single bend power law model to the X-ray power spectra, as measured by Summons (2008), are also shown in Figure 5.3, for direct comparison with the optical PSDs. From visual inspection it appears as if the shape of the optical PSD could be similar to the X-ray PSD for at least some of the targets. I investigate this possibility in more detail the next section.

5.3.2 Single bend power law model

A bending power law model is described by

$$P(\nu) = \frac{A\nu^{-\alpha_L}}{1 + (\nu/\nu_B)^{\alpha_H - \alpha_L}} \tag{5.4}$$

with α_L the low frequency slope, α_H the high frequency slope and ν_B the frequency at the bend (M$^{\rm c}$Hardy et al., 2004).

The optical data are not good enough to constrain all the parameters. A more reliable estimate may be obtained by fixing one of the parameters to a reasonable value and testing the other parameters against it. Motivated by the steep best-fit slopes of the unbroken model to the optical PSDs, I fixed α_H to the best-fit high frequency slope of the X-ray PSDs and allowed α_L, ν_B and A to vary. This also allows me to test whether the optical and X-ray PSDs may be described by the same set of parameters. The best-fit parameters for the single bend model calculated this way are listed in Table 5.6 and shown in Figure 5.4.

The measured low frequency slope of NGC 3227, NGC 4051, NGC 5548, Mrk 79 and Mrk 110 are all consistent with the X-ray low frequency slopes, within errors. To illustrate this, Figure 5.4 shows both the best fit (in a solid line) and the fit when the low frequency slope is also forced to the corresponding X-ray value (in a dotted line). The acceptance probabilities are generally very high, suggesting that the optical power spectra may be described by the X-ray PSD parameters and hence that the underlying variability generating processes are closely related. The model parameters cannot be constrained tightly however, and the higher value of p is most likely the result of fitting a more complex model with more free parameters, rather than a true increase in the probability of the fit. In most cases the break frequency measured is towards the lowest frequency that can be measured in the dataset, so it appears that, if the optical power spectra do have a bending power law shape as well, the break will be at lower frequencies than the X-ray bend. However, the bend frequency is unconstrained by the data, so no conclusions can be drawn from the measured values.

For NGC 4593 and NGC 7469, the best fit single bend model has a lower acceptance probability than the unbroken model, so that the former can be confidently rejected in favour of the simpler unbroken model. NGC 7469 has the lowest acceptance probability in the sample for an unbroken power law, but it is fit even more poorly by a single bend model in which the high frequency slope is fixed to a typical X-ray value. As its X-ray PSD is not yet available (Markowitz et al., in preparation) I cannot compare the optical PSD fit to the X-ray fit as for the other targets. As shown in Table 5.6, the bending power law is rejected by the data – the low frequency slope increases until it reaches the same value as the high frequency slope. The bending power law model shown in Figure 5.4 is the best fit obtained by forcing a break to a typical X-ray low slope value. The 'best' fit has $\alpha_L = 0.9$, but a very low likelihood of acceptance, $p = 0.081$.

5.3.3 Physical interpretation?

Due to the difficulties in obtaining long enough optical light curves of sufficient quality (especially in terms of sampling) optical variability power spectra are not commonly found in literature. The optical variability power is usually studied using a structure function analysis instead (e.g. Collier and Peterson, 2001), which can be calculated entirely in the time domain (rather than the frequency domain, like the PDS). Here I wanted to take advantage of the detailed Monte Carlo simulations of PSRESP which account for the problems of sampling effects and red noise leak, to compare the results directly to the X-ray PSDs.

Czerny et al. (1999) measured the optical power spectrum of NGC 5548 and found evidence of a break in the power law spectrum at a frequency corresponding to $\sim$ 100 days. Their analysis does not take account of red noise leak and other distorting effects introduced by the sampling of the light curve, however, so it is unclear what the uncertainty on this measurement is. The bend frequency of the best fit single bend model I measured here is of similar magnitude, corresponding to $\sim$ 200 days. However, this break time-scale is completely unconstrained by the data, so the result is highly uncertain. Based upon the high acceptance probability of the unbroken power law model, I have to conclude that, although the possibility that a break could be present in the optical PSD cannot be excluded, the current

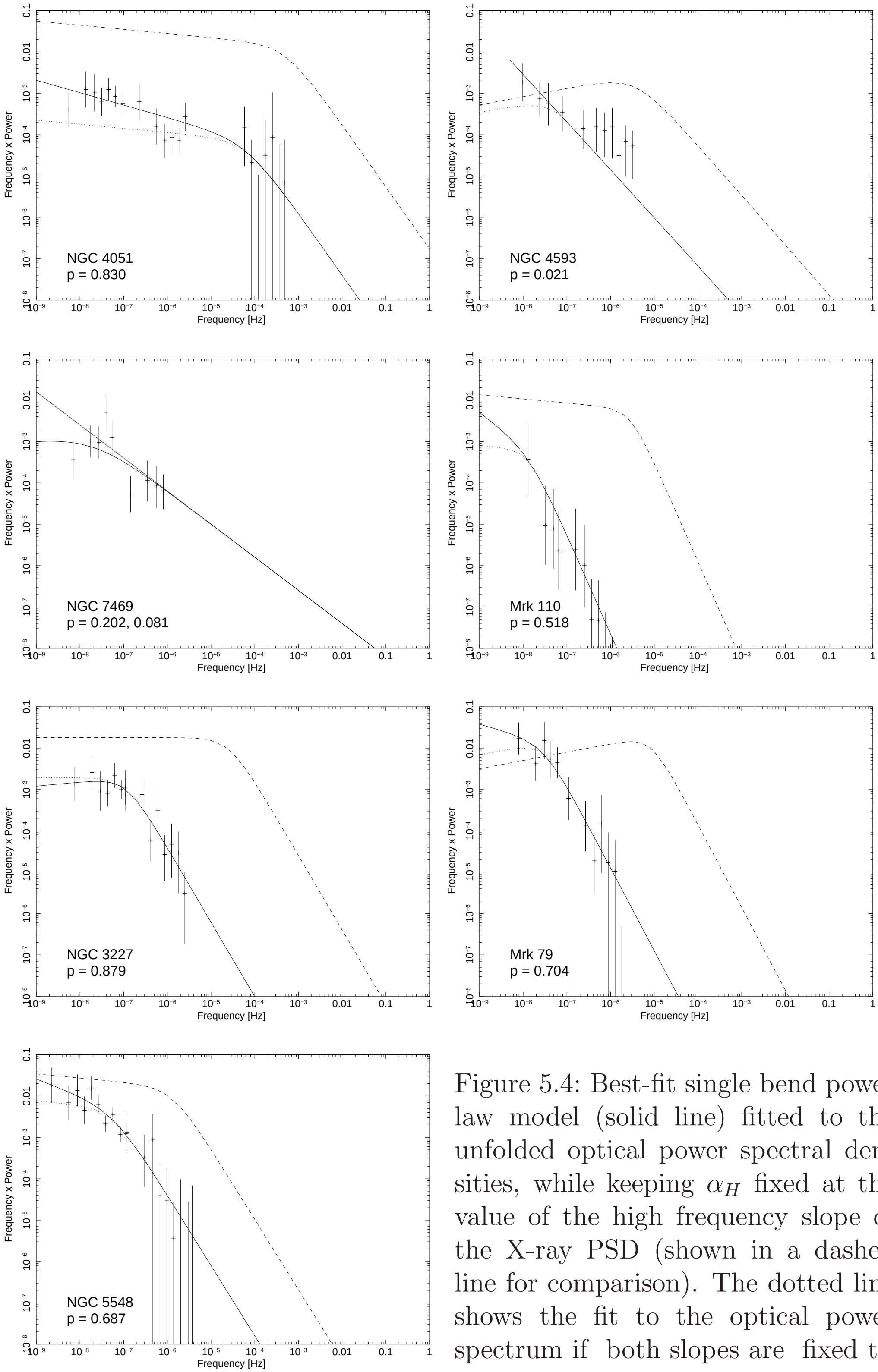

Figure 5.4: Best-fit single bend power law model (solid line) fitted to the unfolded optical power spectral densities, while keeping α_H fixed at the value of the high frequency slope of the X-ray PSD (shown in a dashed line for comparison). The dotted line shows the fit to the optical power spectrum if both slopes are fixed to the X-ray values. The acceptance probabilities refer to the best-fit (solid) line in each case. For NGC 4593 and NGC 7469 an unbroken model is clearly preferred. A break can be forced, but the acceptance probability is low.

Table 5.6: Best-fit low frequency power law slope α_L, break frequency ν_B and model acceptance probability p, when fixing α_H to the X-ray PSD high frequency slope

Target	α_H	α_L	ν_B (Hz)	p
NGC 4051	2.5	$1.3^{+0.2}_{-0.3}$	$6.7^{+*}_{-0.1} \times 10^{-5}$	0.830
NGC 4593	2.2	$2.1^{+0.1}_{-0.6}$	$5.0^{+*}_{-*} \times 10^{-8}$	0.021
NGC 7469	1.8	$1.8^{+0.0}_{-1.0}$	$2.0^{+*}_{-*} \times 10^{-8}$	0.202
Mrk 110	3.4	$1.8^{+1.5}_{-1.1}$	$1.4^{+3.2}_{-*} \times 10^{-8}$	0.518
NGC 3227	2.8	$0.9^{+1.1}_{-0.2}$	$1.1^{+7.51}_{-*} \times 10^{-7}$	0.879
Mrk 79	3.0	$1.3^{+0.7}_{-0.6}$	$3.0^{+*}_{-*} \times 10^{-8}$	0.704
NGC 5548	2.7	$1.4^{+0.2}_{-0.9}$	$5.8^{+*}_{-*} \times 10^{-8}$	0.687

Table 5.7: Parameters of the best-fit single bend power law model to the X-ray PSDs, as determined by Summons (2008). NGC 7469 was not part of this study.

Target	α_H	α_L	ν_B (Hz)
NGC 4051	$2.5^{+0.0}_{-0.8}$	$1.1^{+0.1}_{-0.4}$	$5.1^{+4.9}_{-2.6} \times 10^{-4}$
NGC 4593	$2.2^{+0.3}_{-0.3}$	$0.8^{+0.3}_{-0.3}$	$3.8^{+4.8}_{-2.1} \times 10^{-6}$
Mrk 110	$3.4^{+0.1}_{-0.9}$	$1.1^{+0.2}_{-0.4}$	$2.9^{+11.8}_{-1.4} \times 10^{-6}$
NGC 3227	$2.8^{+0.2}_{-0.8}$	$1.0^{+0.3}_{-0.3}$	$2.6^{+6.1}_{-1.8} \times 10^{-5}$
Mrk 79	$3.0^{+0.0}_{-1.0}$	$0.8^{+0.4}_{-0.1}$	$8.5^{+20.3}_{-6.0} \times 10^{-6}$
NGC 5548	$2.7^{+0.3}_{-0.7}$	$1.1^{+0.1}_{-0.6}$	$1.3^{+1.6}_{-0.9} \times 10^{-6}$

data is best described by a simple, unbroken power law model. In fact, this is true of all the sources in this sample.

In a related study to the present investigation, Arévalo et al. (2009) measured the X-ray and optical power spectra of NGC 3783, and also found (as in the case of NGC 5548, NGC 4593 and Mrk 79 here) that the optical power exceeds the X-rays at low frequencies. Comparing the rejection probability contours of the X-ray and optical PSD fits, it is shown that in that source, the X-ray and optical power spectra are significantly different, i.e. they cannot be described simultaneously by the same set of parameters.

M^{c}Hardy et al. (2006) has shown that the time-scale associated with the X-ray PSD break frequency scales approximately linearly with the black hole mass, over many orders of magnitude (from AGN to Galactic black hole X-ray binaries). It therefore appears to be a characteristic common of accreting black holes and is therefore generally associated with the accretion flow. This relationship depends on the accretion rate as well, as the scatter in the correlation can largely be accounted for by considering the difference in accretion rate between the systems in the sample.

The physical reason for the change in variability at a characteristic frequency is not yet clear. The model of Lyubarskii (1997) explains the broad range of variability time-scales seen in AGN as the multiplicative effect of fluctuations at the outer parts of the disc (where the natural time-scales are longer) propagating inward, modulating the local, faster variability at smaller radii on time-scales characteristic of the outer disc. Hence the high frequency variations characteristic of the inner regions of the disc also include variability at much lower frequencies. This model relates mainly to accretion rate fluctuations in the disc, but it has been extended by Churazov et al. (2001) to include modulation of the X-ray emission as well, through a thick inner flow. Arévalo and Uttley (2006) have shown that inward propagating fluctuations like this can successfully account for the flattening of the X-ray power spectral densities at low frequencies, as well as the linear rms-flux relation observed in the X-ray light curves of AGN and X-ray binaries (Uttley and M^{c}Hardy, 2001). This model has also been applied, in combination with X-ray reprocessing by the accretion disc, to explain the optical variability of the quasar MR2251-178 (Arévalo et al., 2008).

I will illustrate the main physical time-scales of importance in this region with a few examples. The break frequency is too low to be associated with a light crossing time-scale. For example, for a typical black hole mass of $10^{7} M_{\odot}$, the light crossing time to the inner edge of the disc (assumed to be $6R_g$, the last stable orbit around a non-spinning black hole) is only 300 s, or 3×10^{-3} Hz. A typical X-ray break time-scale of 10^{-5} Hz corresponds to a light crossing distance of $2030R_g$ which is much larger than the size of the X-ray emitting region inferred from the shortest variability time-scales. Instead it is usually assumed that the variability originates in the accretion flow and that the break time-scale is associated with the disc. 10^5 s corresponds to the orbital time-scale at $47R_g$ or the viscous time-scale at $\sim 10R_g$ if the inner disc is as thick as $H/R \sim 0.5$.

If the optical power spectra do have breaks as well, and they are at longer time-scales than the X-ray breaks, as the fits in Figure 5.4 suggest, it may point to similar physical processes operating in the optically emitting region of the disc. For example, the optical emitting region of a $10^7 M_\odot$ black hole with a fractional accretion rate of $\dot{m} = 0.05$ is at $\sim 2700R_g$. At this distance the viscous frequency is 1×10^{-10} Hz for a moderately thin disc ($H/R \sim 0.1$) or 4×10^{-9} Hz for a thick ($H/R \sim 0.5$) disc. Both these estimates are towards the longest time-scales sampled by the optical PSDs, or longer, so if the break is caused by instabilities propagating on the viscous time-scale, it would not be measurable from the current data. It seems likely that some of the large amplitude, long time-scale variations are driven by such fluctuations (e.g. Arévalo et al., 2008, 2009, and Chapter 3 herein) and may be the cause of the large optical variability amplitude on long time-scales. Hence it manifests in the power spectra as the high power at low frequencies.

I will now consider the effect of X-ray reprocessing on the optical power spectrum. Using the method of Timmer and Koenig (1995), I simulated a typical X-ray light curve of power spectral shape $\alpha_L = 1.0$, $\alpha_H = 2.5$ and $\nu_B = 10^{-6}$ Hz. Using the M^{c}Hardy et al. (2006) relation between break time-scale, mass and bolometric luminosity, this break frequency would be appropriate for a system with a luminosity $L_{\rm bol} \sim 5 \times 10^{44}$ erg s^{-1} and mass $M \sim 10^8 M_\odot$. Thus assuming an accretion rate of $L_{\rm bol}/L_{\rm Edd} \sim \dot{m} = 5\%$, I calculated a corresponding V band light curve, assuming that it is the combined effect of intrinsic disc emission and reprocessing of the X-rays. I followed the model of Kazanas and Nayakshin (2001), discussed in detail in Section 4.4.2. I then calculated the power density spectrum of the resulting model V band light curve. The power spectra are shown in Figure 5.5.

The reprocessed PSD is fitted very well by the same power law slopes as the input X-ray power spectrum, but as in the observed PSDs, the bend frequency appears at lower frequencies than the X-ray bend. The bend frequency shown here

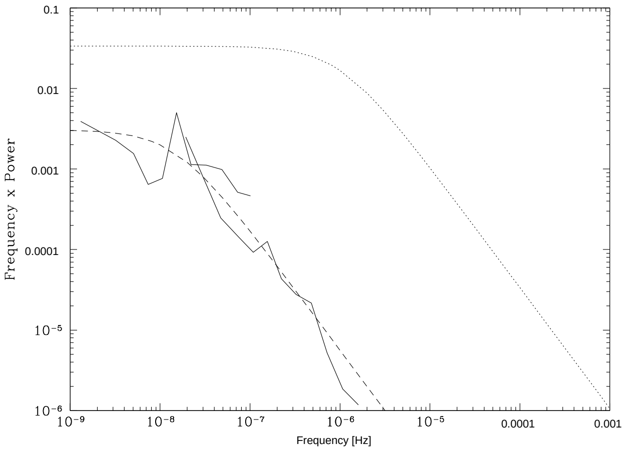

Figure 5.5: Optical power spectrum calculated from a reprocessing model, plotted in solid lines. The input X-ray power spectrum assumed to irradiate the accretion disc is shown in a dotted line. As in the observed PSDs, the break frequency moves to lower frequencies. The dashed line shows the shape of the X-ray power spectrum (i.e. both slopes fixed to the X-ray value) fitted to the optical PSD.

is at 1.5×10^{-8} Hz (770 days), which is included in the frequency range spanned by most of the optical light curves used here, albeit towards the lowest frequencies measurable. Comparison of this simulated PSD to the observed PSDs suggests that the possible flattening of the optical power spectrum results directly from the X-ray variations imprinted on the optical light curve through X-ray reprocessing. Note also, that as we have assumed reprocessing to be the only driver of the optical variations, the amplitude (and hence the power) of the optical variability is lower than that of the X-rays. These simulations are however still at a preliminary stage and should be tested over a wider range in mass and accretion rate than the single case considered here.

Various avenues of this research have indicated that reprocessing cannot be the only contributor to the optical variations. Model reprocessed light curves are always much better correlated with the input X-ray light curve than is observed in real data, so other effects play an important role as well and reduce the strength of the correlation. Such effects will no doubt have important consequences for the power spectra as well. So far, the break frequencies of the observed optical power spectra are unconstrained, so comparisons can only be made qualitatively.

Although the current optical PSDs are best described by an unbroken power law model, continuing to rise towards the lowest frequencies probed, the PSD is expected to flatten at some frequency, otherwise the total power would diverge.

The physical interpretation of a break in the optical power spectrum is not yet clear, but it may be associated with a characteristic time-scale as part of the reprocessing of X-rays or the local viscous time-scale in the disc.

5.4 Cross correlation analysis

5.4.1 X-ray/optical correlations

For each of the targets, I calculated the cross-correlation between the unsmoothed, unbinned X-ray light curve and the V band optical light curve. Figure 5.6 shows the correlation functions calculated using the Interpolation Cross-correlation function (ICCF) of White and Peterson (1994). Each correlation was also calculated using the Discrete Correlation Function (DCF) of Edelson and Krolik (1988) as a separate check. The two methods agree well for all the targets, but as the interpolation method is more successful at recovering the small lags expected between the two time series, I prefer this method. I discuss this choice of correlation function in more detail in Appendix A, as well as the advantages and disadvantages of the different correlation methods. To account for large gaps in the light curves, where linear interpolation would be a very inaccurate representation of the behaviour of the light curve, I break the light curves into smaller segments, defined by the largest gaps in the light curve. I calculate the correlation function for each optical segment with its corresponding segment of the X-ray light curve individually, and then average the correlation functions, weighted by the length (in time) of the light curve segments. In most cases the gaps in the light curves are when the source is near solar conjunction, so the X-ray light curves often have gaps at these times as well, albeit smaller than those in the optical light curves. The segmentation effectively removes the variability power on time-scale longer than the length of the segments, narrowing the peak of the correlation function. This allows the short term lag to be determined more precisely.

For each correlation, I record the lag of the optical variations behind the X-rays at the peak of the correlation function, as well as its centroid, in Table 5.8. The centroid is calculated as the weighted sum of all the CCF values on either side of the peak, for which the correlation coefficient was greater than 85% of the peak correlation coefficient. The error on the lag was calculated using the flux randomization/random subset selection (FRRSS) method of Peterson et al. (1998b).

The red noise nature of the X-ray and optical variations may cause peaks (or troughs) in the light curves to line up by chance, even if there is no true underlying correlation between the light curves. This will cause spurious peaks in the correlation function, so we have to assess the statistical significance of the apparent correlations we find. As briefly described in Sections 3.3.1 and 4.4.1, I used the method of Timmer and Koenig (1995) to generate random X-ray light curves to compare to the optical light curve. This method uses the X-ray power spectrum of each source, together with a randomized phase and amplitude at each Fourier frequency, to simulate light curves with the same statistical properties as the observed X-ray light curves. Six of the targets studied here are part of our (PI: I. M^{c}Hardy) long term X-ray monitoring program on *RXTE*, to measure the broad band X-ray variability power spectral densities (PSD) of a large sample of AGN. Much of the analysis was carried out by Summons (2008) and I used his best-fit single-bend power law parameters for each of the six sources to create simulated X-ray light curves. The seventh target in the sample, NGC 7469, is not part of our monitoring program, but the X-ray power spectral parameters were kindly provided to me by A. Markowitz (Markowitz et al, in preparation).

For each source, I generated 1000 random X-ray light curves from its power spectrum. To take account of long term variations in the light curves, the light curves are simulated ten times longer than the observed X-ray light curve, to include these long time-scale variations. The observational noise of each observed light curve is measured, and noise was added to the simulated light curves at the same level. The simulated light curve is then sampled in the same way as the observed light curve and cross-correlated with the observed optical light curve. The light curves are broken into segments in exactly the same way as the real data, and the final CCF weighted according to the length of each segment. The simulated light curves are uncorrelated by design and hold no relationship with the optical light curves. Any correlation peak found in their cross-correlations must therefore be purely due to the red noise character of the light curves. The mean, 95% and 99% extremes of the resulting distribution of CCFs may then be compared to the correlation function between the observed X-ray and optical light curves. A peak exceeding the 99% line, can then said to be significant at greater than 99% confidence, as it reaches higher than 99% of the correlations with randomly generated red noise light curves.

The correlation functions of all targets, together with the results from the Monte Carlo simulations just described, are shown in Figures 5.6a–d. All seven sources in our sample show a statistically significant peak at short (∼1–2 days) lags, with the

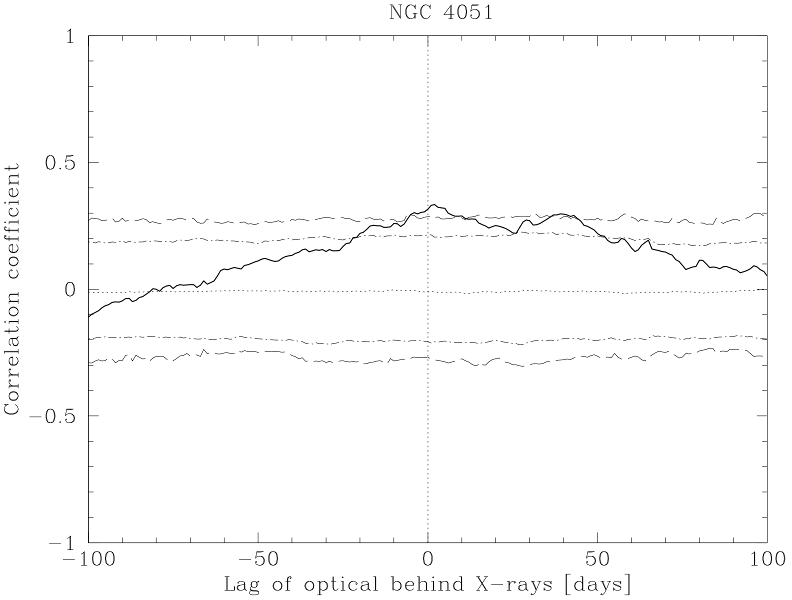

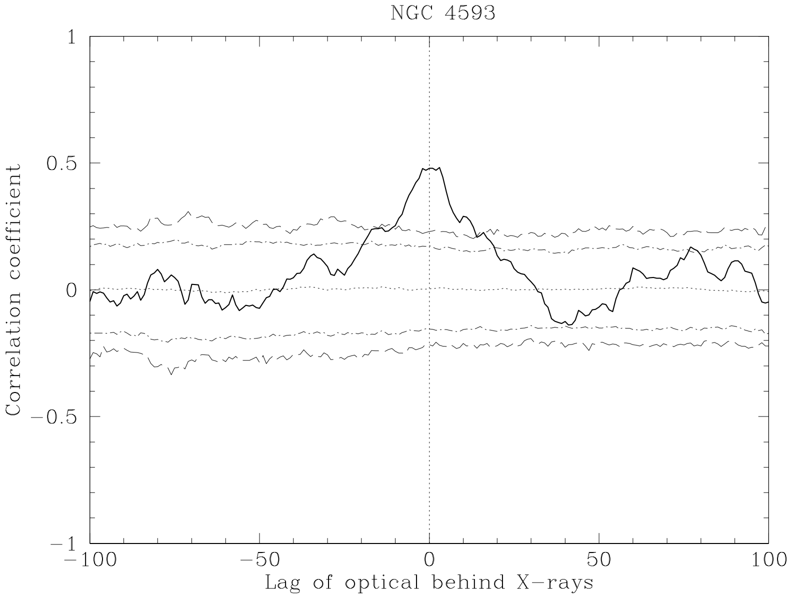

Figure 5.6a: CCF between the X-ray and optical light curves of NGC 4051 (top) and NGC 4593 (bottom). The horizontal dotted, dot-dashed and dashed lines are the mean, 95% and 99% confidence levels, calculated from 1000 Monte Carlo simulations. The vertical dotted line indicates the zero lag position. The CCF of NGC 4051 is the same as in shown in Figure 4.6, but plotted on the same vertical scale as the other CCFs presented in this chapter, for direct comparison.

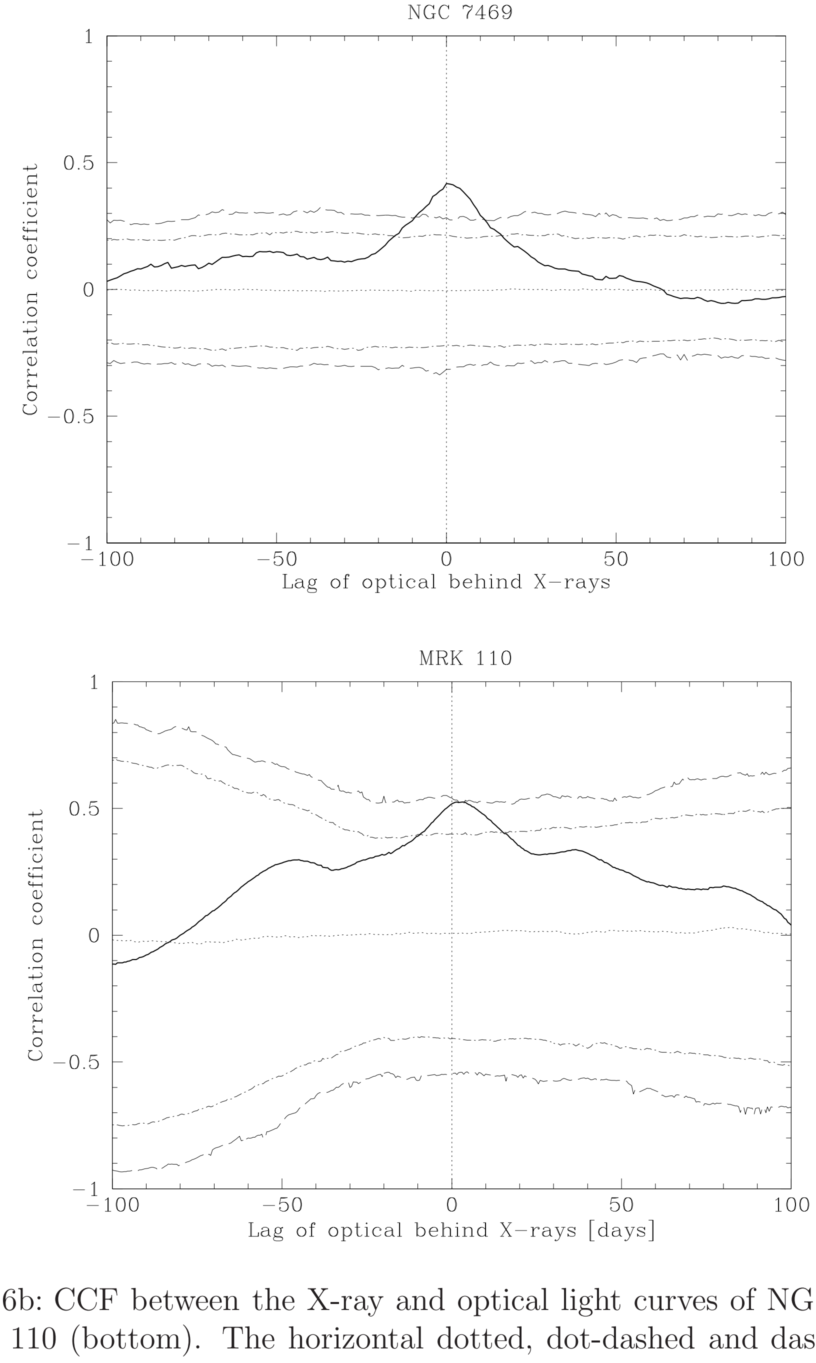

Figure 5.6b: CCF between the X-ray and optical light curves of NGC 7469 (top) and Mrk 110 (bottom). The horizontal dotted, dot-dashed and dashed lines are the mean, 95% and 99% confidence levels, calculated from 1000 Monte Carlo simulations. The vertical dotted line indicates the zero lag position.

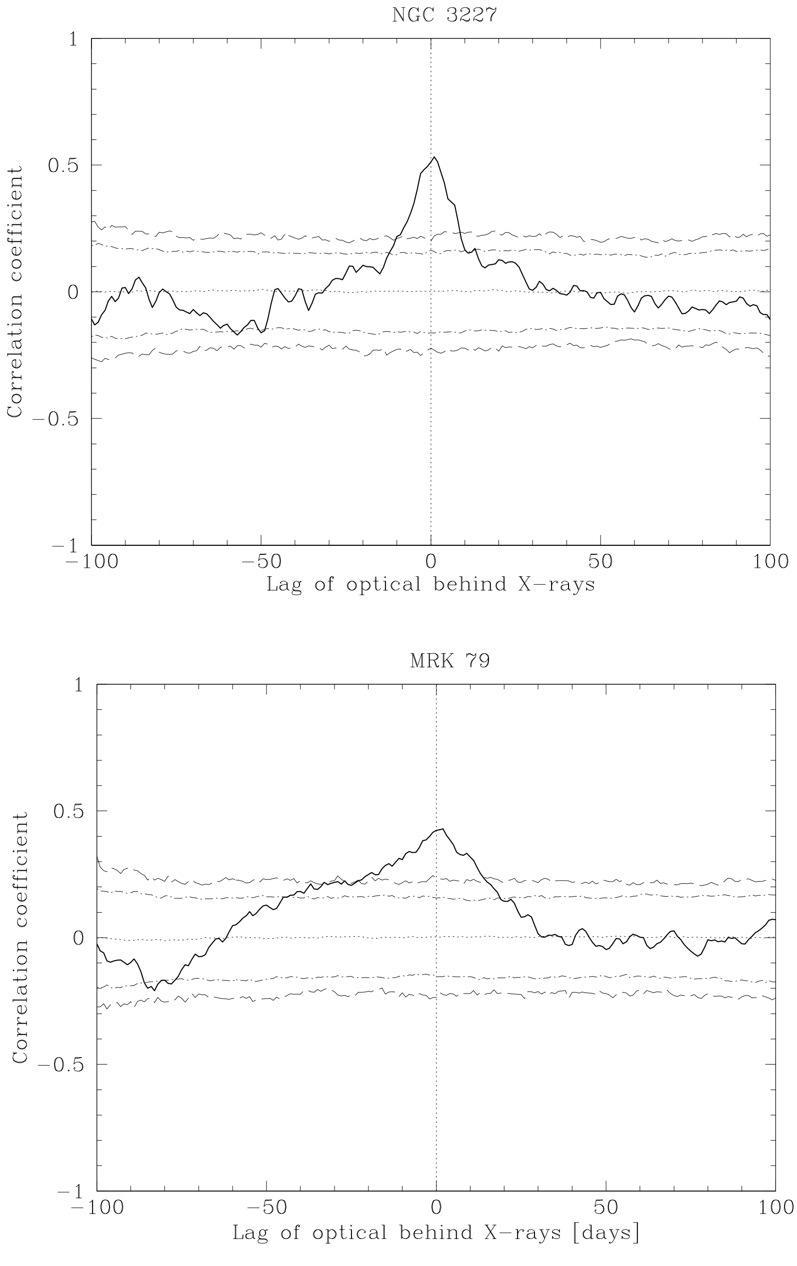

Figure 5.6c: CCF between the X-ray and optical light curves of NGC 3227 (top) and Mrk 79 (bottom). The horizontal dotted, dot-dashed and dashed lines are the mean, 95% and 99% confidence levels, calculated from 1000 Monte Carlo simulations. The vertical dotted line indicates the zero lag position. For Mrk 79, the same function, calculated using the DCF, is shown in Fig. 3.4.

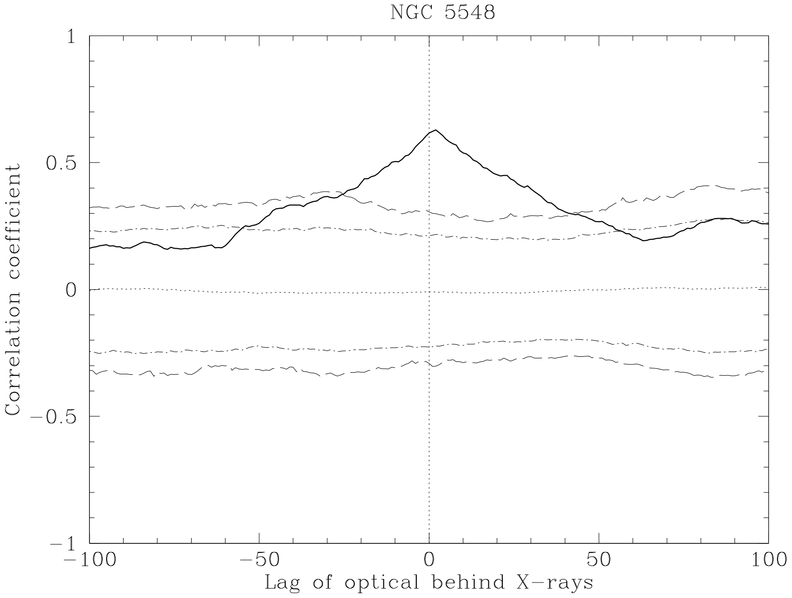

Figure 5.6d: CCF between the X-ray and optical light curves of NGC 5548. The horizontal dotted, dot-dashed and dashed lines are the mean, 95% and 99% confidence levels, calculated from 1000 Monte Carlo simulations. The vertical dotted line indicates the zero lag position.

Table 5.8: Cross-correlation lags (in days). The centroid is calculated at the level of 85% of the peak correlation coefficient.

Target	Peak (EQ)	Centroid (EQ)	Peak (SI)	Centroid (SI)	Peak coeff (SI)
NGC 4051	$2.0^{+1.2}_{-0.6}$	$2.39^{+0.94}_{-1.60}$	$1.2^{+1.0}_{-0.3}$	$1.83^{+1.30}_{-1.97}$	0.378 ± 0.033
NGC 4593*	$1.8^{+1.3}_{-1.1}$	$1.53^{+1.62}_{-1.34}$	$1.8^{+1.2}_{-1.5}$	$1.25^{+1.24}_{-1.18}$	0.480 ± 0.073
NGC 7469	$0.1^{+0.7}_{-0.1}$	$0.58^{+0.79}_{-0.82}$	$0.1^{+0.9}_{-0.6}$	$0.96^{+0.83}_{-0.84}$	0.426 ± 0.036
Mrk 110	$2.9^{+1.0}_{-0.6}$	$5.33^{+1.16}_{-1.34}$	$1.9^{+1.2}_{-0.5}$	$3.31^{+0.97}_{-0.94}$	0.526 ± 0.032
NGC 3227	$0.9^{+0.5}_{-0.8}$	$0.75^{+0.64}_{-0.68}$	$0.8^{+0.4}_{-0.7}$	$0.47^{+0.60}_{-0.72}$	0.593 ± 0.049
Mrk 79	$0.0^{+0.1}_{-0.1}$	$-1.28^{+0.96}_{-1.00}$	$1.7^{+0.1}_{-1.8}$	$0.50^{+0.85}_{-1.22}$	0.429 ± 0.031
NGC 5548	$1.6^{+0.7}_{-0.5}$	$1.95^{+1.14}_{-1.03}$	$1.4^{+0.7}_{-0.8}$	$1.67^{+1.67}_{-2.00}$	0.629 ± 0.024

* Calculated using BI, rather than SI method (see text).

Table 5.9: Width (in days) of the X-ray and optical autocorrelation functions, calculated at correlation strengths of 50% and zero.

	FWHM		Width at 0.0	
Target	X-ray	Optical	X-ray	Optical
NGC 4051	3.2	43.6	84	212
NGC 4593	5.5	8.1	111	120
NGC 7469	7.7	34.5	146	196
Mrk 110	11.0	42.6	139	>200
NGC 3227	3.2	17.1	73	54
Mrk 79	6.8	37.0	129	97
NGC 5548	19.5	114.8	127	>200

optical variations following the X-ray variations. These results favour reprocessing of X-rays by an optically thick accretion disc as a major contributor to the optical variability. The measured peaks and centroids, as well as the maximum value of the correlation coefficient, are shown in Table 5.8. The error on the correlation coefficient was also calculated using the FRRSS method of Peterson et al. (1998b). For NGC 4593, I decided to calculate the correlation using the BI method (see Appendix A), which averages the correlations from interpolating the X-ray and optical light curves in turn. The reason for this is that the photometry errors in this light curve are larger than in the other light curves, due to the bright host galaxy. The increased scatter in the optical light curve may therefore make the interpolation less reliable. The difference between the two methods is marginal, however. The peak of the correlation using the BI method is slightly higher (0.48 vs. 0.46), which lies well within the error on this value.

5.4.2 Autocorrelation functions

The autocorrelation function (ACF) measures the relationship of a light curve to itself, i.e. a measure of how much the value of $f(t_i + \Delta t)$ depends on $f(t_i)$, or how similar it is to a time-shifted version of itself. The ACFs of each of the X-ray and optical light curves are shown in Figure 5.7. In order to compare these to the cross-correlation functions, they were calculated using the same technique: ACFs were calculated from individual segments of the light curve (as were used in the CCF calculation) and combined as a weighted average. It is immediately obvious that the X-ray ACFs are much narrower than the optical ACFs, owing to the

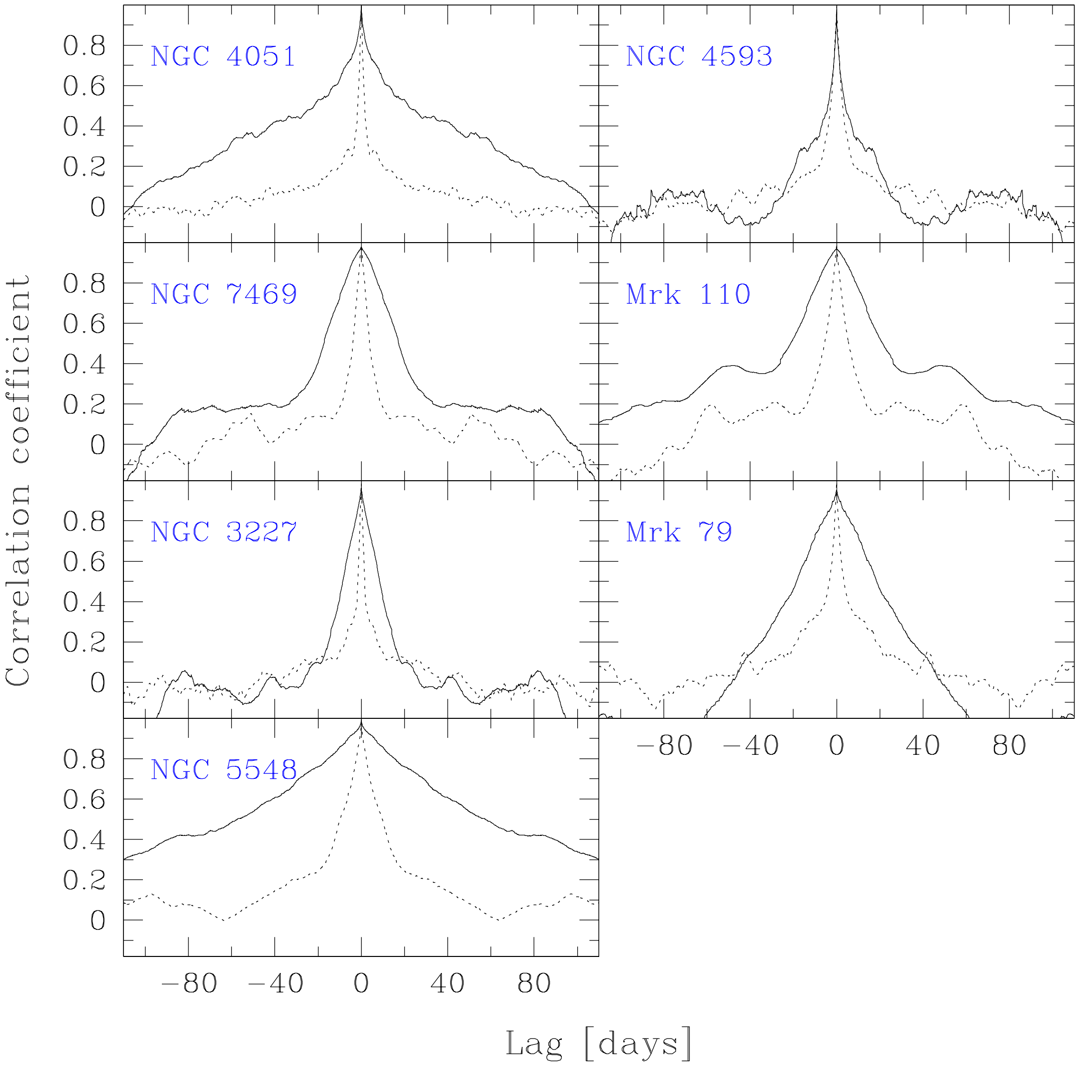

Figure 5.7: X-ray (dotted line) and optical (solid line) autocorrelation functions of all targets, calculated using the same segmentation technique as was used to calculate the CCFs.

longer time-scale variability present in the optical light curves. The width of the autocorrelations at 0.5 and 0.0 correlation strength are listed in Table 5.9. The self-correlation of the X-ray light curves decrease to 0.5 in less than 20 days, while for the optical light curves it can take more than 4 times this long.

It is not straightforward to compare the widths of the ACFs among each other, as they will be affected by the segmentation of the light curves. The segmentation removes long time-scale power from the light curves, hence narrowing the peak. The amount by which the width of the peak is changed depends on the amplitude of long time-scale variations present in the light curve as well as the lengths of the segments used to calculate the ACF. The same segmentation is applied to the X-ray and optical light curves, so their relative widths may be more instructive to consider. Apart from NGC 4051, which is discussed in detail in Chapter 4, the relative width of the X-ray to optical ACF width increases with black hole mass, i.e. the optical variations in high black hole mass systems are slower than in less massive systems.

Also important to note is that the observed ACF is the convolution between the true ACF of the data and the ACF of the "sampling function" (see Gaskell and Peterson, 1987). The width of the observed ACF therefore also depends on the details of the sampling. Many of the "shoulders" seen in the ACFs in Figure 5.7 can most likely be attributed to the sampling, rather than real variability behaviour of the light curves.

5.4.3 Notes on individual objects

NGC 4051

This NLS1 displays a complex set of variability characteristics on different time-scales, discussed in detail in Section 4.6.2. It is is the only galaxy in the sample which appears to show significant optical variability lagging the X-ray variations on time-scales of months, in addition to the peak at short positive lags (days). The length of this second lag suggests that it may be associated with the dust torus.

NGC 4593

Spectral fits to the UV/optical continuum and the relatively narrow Fe Kα line in this Seyfert galaxy require the accretion disc to be truncated at $\sim 30R_g$ (Lu and Wang, 2000). The flow is assumed to turn into an ADAF interior to this radius. As much as 3% of the total V band optical emission may originate from within $30R_g$ in a standard thin disc which extends down to $6R_g$, for a system of this mass and accretion rate. A truncated disc will of course have an even greater influence on the emission of bluer wavelengths such as the *U* band. The correlation function shown here indicates a correspondence between the X-ray and optical variations which is consistent with reprocessing. Fitting reprocessed model light curves to simultaneous multicolour observations of this galaxy (as was done in Section 3.4 for Mrk 79) could therefore provide an additional test of the truncated disc requirement.

NGC 7469

This galaxy is perhaps best known for the bright circumnuclear starburst ring within a $\sim 1''.5$–$2''.5$ of the nucleus (e.g. Davies et al., 2004, and references therein). The starburst is estimated to contribute $\gtrsim 50\%$ of the bolometric luminosity of the galaxy. I make the assumption that the emission due to starburst activity is constant over the monitoring period, so that it can be removed from the light curve along with the host galaxy flux. The galaxy flux in the aperture was measured by Suganuma et al. (2006) by modeling and subtracting the nucleus from the images, and measuring the flux remaining on the nucleus-free image. It is therefore included in the host galaxy flux measurement.

There is a complex relationship between the X-ray and UV emission in this galaxy, broadly suggestive of a Comptonization origin of the X-ray emission from upscattered UV photons (Nandra et al., 1998, 2000). Wavelength-dependent delays observed between the UV and optical bands favour an accretion disc origin of the optical emission, enhanced by reprocessing of variable X-ray emission (Collier et al., 1999). Our cross-correlation results here are consistent with this interpretation.

Mrk 110

This is by far the shortest light curve in the sample and the Monte Carlo simulations show that the correlation peak is only just reaching 99% significance at the moment (Fig. 5.6b). Further monitoring of the source is expected to increase the statistical significance of the result. Experience with other targets have shown that increasing the length of the light curve decreases the number of random correlations with the simulated light curves, so that the significance levels drop. (Notice that the significance lines in Figure 5.6b are higher than for any other target). The peak correlation coefficient, on the other hand, is not found to change very much with increased monitoring. It is for this reason that Mrk 110 can be included in the correlation calculations in Section 5.5.2, even though the correlation detection is formally less significant than for the other targets.

NGC 3227

Derived X-ray spectral parameters, as well as the low accretion rate ($\dot{m} \sim 0.01$) suggest that the inner accretion flow in this galaxy may be advection dominated (Markowitz et al., 2009). However, the highly significant correlation between the X-rays and optical emission shown here implies that at least the region of the disc where the optical emission is generated, must be optically thick and radiatively efficient.

Mrk 79

Mrk 79 is the only source in the sample which shows a strong asymmetry towards negative lags (i.e. optical leading the X-ray variations). This is an effect of the long time-scale variability clearly visible in the optical light curve. I have shown in Chapter 3 that this long time-scale trend can be reproduced by allowing the accretion rate or the geometry of the system to vary on time-scales of ∼years. The short time-scale variations are driven by the variable X-ray heating however, and the peak of the CCF is consistent with the light travel time to the optical emitting part of the disc in this source.

NGC 5548

The cross-correlation lag measured here agrees very well with that reported by Suganuma et al. (2006), who found the optical emission to lag the X-rays by $1.6^{+1.0}_{-0.5}$ days. While it is clear that in the earlier part of the monitoring of NGC 5548 the optical variations exceeded the X-ray variations (as also reported by Uttley et al. 2003), the system has gone into a less variable state with lower optical luminosity in recent years. Although the X-ray emission is slightly less variable as well, the decrease is not as dramatic as for the optical. Considering only this low optical luminosity part of the light curve, the X-ray variations exceed the optical variations by several per cent. This low-luminosity state has also been noticed by Bentz et al. (2007).

5.5 Discussion

5.5.1 X-ray/optical lags

The cross-correlation results presented in Section 5.4 show a small positive lag of the optical behind the X-ray variations for all the targets in the sample. The correlation peaks of Mrk 79 and NGC 7469 are consistent with zero days.

Assuming a simple model of an X-ray source at height h_X above the accretion disc and on the axis of symmetry of the system, one can calculate the lag expected between the X-ray and optical variations, if they were connected through reprocessing of X-rays. In this scenario the lag is interpreted as a light travel time and the optical radiation is the combined effect of viscous dissipation in the disc and heating by the variable X-ray source.

For the targets in our sample the expected X-ray/optical lags are 1.4 days for NGC 4051, 1.9 days for NGC 4593, 2.6 days for NGC 7469, 4.0 days for Mrk 110, 1.9 days for NGC 3227, 1.7 days for Mrk 79 and 4.1 days for NGC 5548. Uncertainties in the mass, accretion rate, X-ray luminosity and geometry of the system allow for an error of $\sim$1.5 days either way. The lag of the correlation peaks given in Table 5.8 are therefore all consistent with the lags expected for reprocessing.

These results suggest, for the first time, that reprocessing is a common occurrence in Seyfert galaxies. I point out that the values of the peak correlation coefficients are generally low (although significant), which implies that at least part of the X-ray and optical emitting regions vary incoherently and that reprocessing is not the only contributor to the optical variations. It is for this reason that reprocessing is not easily detected from short light curves. The cross-correlation results of the sample as a whole do however show that reprocessing plays a key role in generating the short time-scale optical variations observed in Seyfert galaxies. This conclusion is also supported by the wavelength-dependent delays consistent with the $\tau \propto \lambda^{4/3}$ prediction from X-ray reprocessing, observed in a sample of 14 AGN by Cackett et al. (2007).

Note that this result does not rule out correlated variability occuring on long (viscous) time-scales as well. As shown in Arévalo et al. (2008) by using simulated data, the rapid variations due to reprocessing dominate the correlation function, regardless of whether the amplitude of the long time-scale variations are larger than the fast variations or not. Even if there is an unambiguous delay between the long term variations in the absence of reprocessing, the peak of the correlation function is shifted to a short lag when reprocessing is included in the simulations. In calculating the correlation functions here, I have attempted to reduce the contribution from these long time-scale variations (by calculating the correlation from individual segments) to make a more accurate determination of this short time-scale lag.

5.5.2 Strength of the correlation

For the seven Seyfert 1 galaxies under consideration, we can now investigate the dependence of the strength of the X-ray/optical correlation on the galaxy parameters.

Uttley et al. (2003) proposed that the dominant process driving the observed optical variability, was dependent on the mass and accretion rate of the black hole, as these parameters define the temperature profile of the accretion disc. From Eqn. 5.5 it follows that AGN with a smaller black hole mass and/or higher accretion rate, will have hotter discs than systems of high mass/low accretion rate. Scaled in terms of the gravitational radius, the X-ray and optical emitting regions are further apart in the low mass systems, so the viscous time-scale in the optical emitting region is very long compared to that in the inner disc, where the X-rays originate from. In massive systems, with a smaller difference in R_g between the X-ray and optical emitting regions, variations on time-scales of months–years will therefore be closely coupled, resulting in a strong correlation. On the contrary, in less massive systems, the characteristic time-scales at the X-ray and optical emitting regions will be very different (since it scales with r/R_g), weakening the correlation.

In order to test this hypothesis, I use the parameters given in Table 5.1 to calculate a characteristic temperature for each system. Scaled in terms of the fractional accretion rate $\dot{m} = \dot{M}/\dot{M}_{\rm Edd}$ and gravitational radius $R_g = GM/c^2$, the temperature at radius $R = r/R_g$ in the accretion disc is given by

$$T(R) = 3.8\times10^6 \; \dot{m}^{\frac{1}{4}} \; m_6^{-\frac{1}{4}} \; R^{-\frac{3}{4}} \quad \mathrm{K} \tag{5.5}$$

(see Section 1.1.1). m_6 is the mass of the black hole in units of $10^6 M_\odot$. I assume the temperature at $r = 10R_g$ as representative, since this should correspond approximately to the maximum temperature of a full disc (i.e. extending down to $6R_g$). Note that this relationship does not take into account any dissipation of accretion power into a corona, for example, or the effects of propagating instabilities in the disc. Nevertheless, the assumption that a more massive black hole hosts a cooler disc, is a reasonable one, so Eqn. 5.5 can still be used as a gauge of the disc temperature.

Figure 5.8 shows the strength of the correlation, using the peak correlation coefficient as an indicator, plotted against the disc temperature. The peak correlation coefficients are shown in Table 5.8. To increase the sample size I also include the

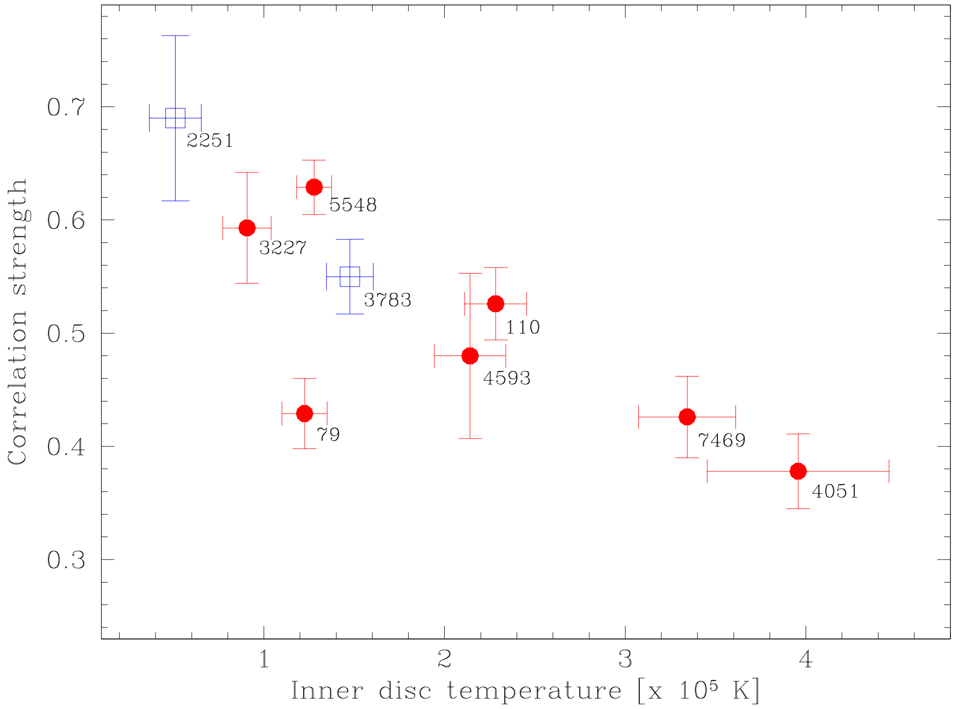

Figure 5.8: Relationship between the strength of the X-ray/optical correlation and disc temperature. The label at each point identifies the sources studied in this chapter. The two points plotted in blue squares are MR2251-178 from Arévalo et al. (2008) and NGC 3783 from Arévalo et al. (2009).

cross-correlation results of MR2251-178 and NGC 3783 from Arévalo et al. (2008) and Arévalo et al. (2009), respectively. The mass of the black hole in MR2251-178 is not well known. Using the relationship between the X-ray PSD break time-scale, accretion rate and mass, derived by M^{c}Hardy et al. (2006), together with the break time-scale measured by Summons (2008), a lower limit on its mass is found to be $4\times10^8 M_\odot$. I follow Arévalo et al. (2008) in assuming a mass of $M = 8\times10^8 M_\odot$ and allow for factor of 2 uncertainty either way.

The results are highly suggestive of a trend that stronger correlated variability is found in cooler accretion discs. Under the assumption of a standard thin disc, these are the systems with very massive black holes and/or low accretion rates.

The Kendall Tau rank correlation coefficient (Kendall, 1970) is a generalised linear correlation statistic, used especially for non-parametric datasets (i.e. when no assumption is made about the underlying probability distribution of the variables). As the name suggests, it compares the data pairs by their rank (order) in a sequence, and the coefficient represents a probability of linear correlation between the pairs of variables. It takes on values between 1 and –1 for, respectively, perfect rank agreement (perfectly correlated and increasing) to perfect rank reversal (perfectly correlated and decreasing). No relationship between parameters is indicated by $\tau_K = 0$. It is viewed as superior to the Spearman Rank Correlation test for ease of interpretation. A detailed discussion on the Kendall Tau and other non-parametric tests may be found in Press (2002), pp. 639–645.

For the correlation strength—temperature relationship shown in Figure 5.8, the Kendall coefficient is $\tau_K = -0.67$, indicating only a moderate probability of correlation. It appears from that figure to be adversely affected by the relatively lower correlation coefficient of Mrk 79. A possible reason for the low correlation coefficient of that source is the large amplitude, long time-scale variations in the optical light curve which weaken the correlation, as similar variations are not present in the X-rays.

The trend is suggestive of a (linear) relationship between the disc temperature and the correlation strength and is consistent with a picture where the strength of the correlation is determined by the relative locations of the X-ray and optical emitting regions in AGN (Uttley et al., 2003). Further targets would need to be included in this correlation to determine whether it is real. Also important to consider is the effect different correlation methods and binning of the light curves have on the correlation coefficient. All these correlations were calculated using unbinned light curves and a preliminary investigation into the effects of different correlation methods suggest that it can be accounted for within the given error bars.

In order to assess the relative contribution of accretion rate and black hole mass to the temperature correlation, I also show in Figures 5.9 and 5.10 their relationship to the correlation strength. The correlation seems to be dominated by the correlation with mass (Kendall coefficient $\tau_K = 0.72$) with only a very weak dependence on accretion rate ($\tau_K = 0.28$). In fact, calculating the partial correlation coefficient[3] (Akritas and Siebert, 1996), which measures the strength of the relationship in the presence of a third variable (the black hole mass, in this case), it is found that the variation in disc temperature between the different sources can be accounted for entirely by the variation in their mass; the accretion rate is not required. The accretion rate correlation was calculated using physical units rather than fractional units, to remove the implicit dependence on mass

---

[3] Partial correlation coefficient calculated using the FORTRAN code available from the Centre for Astrostatistics at Penn State University, http://astrostatistics.psu.edu/. Based upon the Kendall tau rank correlation method outlined by Akritas and Siebert (1996).

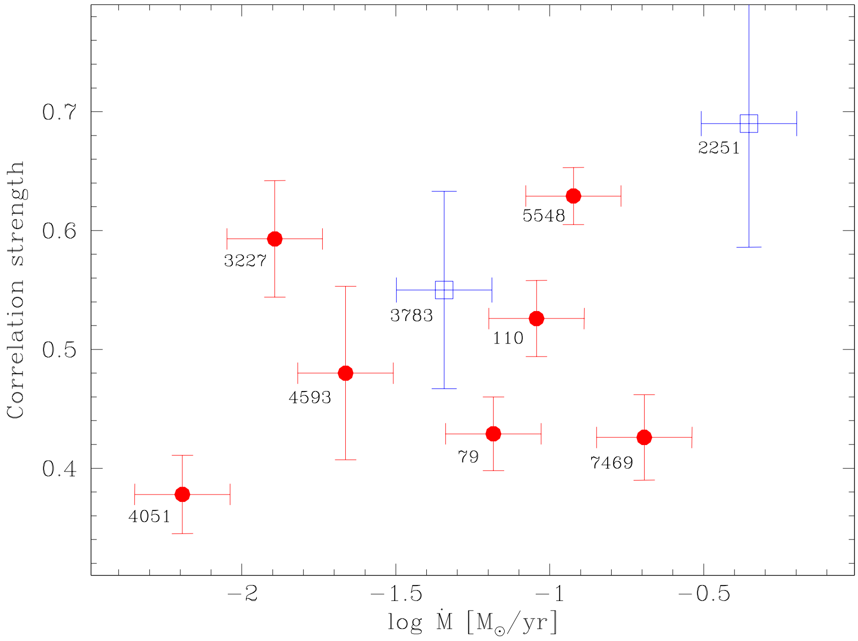

Figure 5.9: Relationship between the strength of the X-ray/optical correlation and the accretion rate (in physical, rather than fractional units).

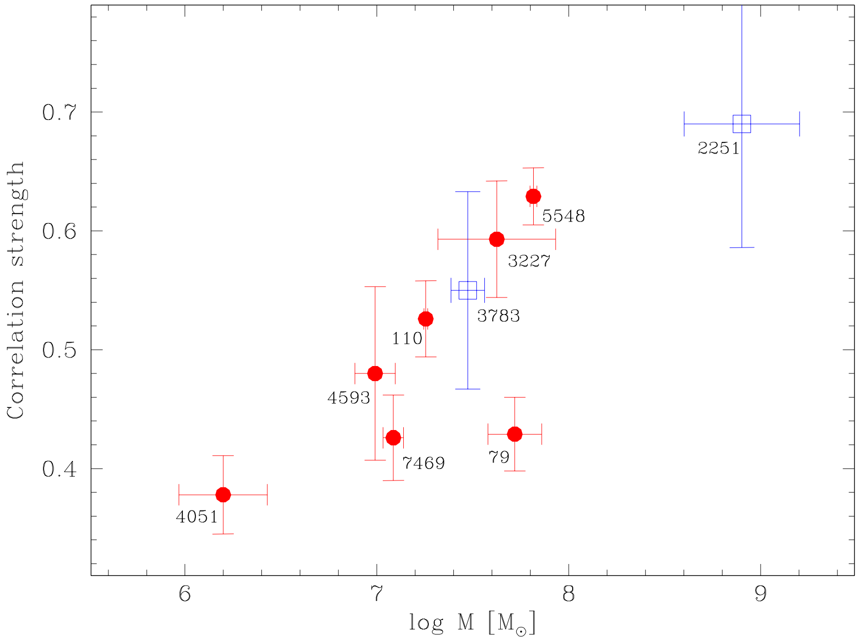

Figure 5.10: Relationship between the strength of the X-ray/optical correlation and black hole mass.

through the Eddington luminosity.

A possible reason for the weak dependence on $\dot{m}$ is that the range in $\dot{m}$ for the current sample, is smaller than the range in black hole mass, especially when considered in terms of the Eddington fraction. For this small sample ($N = 9$ objects), the relationship seems to depend strongly on the quasar MR2251-178 which anchors the high mass (low temperature) end of the correlation. Further simultaneous X-ray/optical monitoring of AGN across a range of black hole mass and accretion rate would be very useful to constrain this relationship and to determine whether the strength of the correlation is mass–, rather than temperature dependent, as the current sample suggests.

6 Conclusions and future work

6.1 Summary of findings

I have presented in this thesis the longest yet concurrent X-ray and optical light curves of a sample of seven Seyfert galaxies. The aim of this study was to determine the previously highly ambiguous relationship between the X-ray and optical variability in Seyfert galaxies, by comparing their long term light curves.

The optical data used in this thesis result from our long term optical monitoring program on the Liverpool Telescope, with some additional monitoring data from the Faulkes Telescope North. These light curves were combined with data obtained from collaborators at the Crimean Astrophysical Observatory and the University of Tokyo, as well as some archival data, to produce optical light curves covering a total time-scale of between four and thirteen years, for the individual sources. The X-ray data is part of our ongoing X-ray monitoring program on *RXTE* to measure the broadband X-ray power spectral densities of AGN.

The main conclusions of this work are summarized as follows:

i. Highly correlated variability is seen on time-scales of days to months. Cross-correlation analysis reveal a statistically significant correlation between the X-ray and optical variations in *all* the galaxies in this sample.

ii. All the correlation functions show a lag of the optical emission behind the X-ray variations, on time-scales of 1–2 days. For each galaxy the lag is consistent with what is expected for the light travel time to the optically emitting region of the accretion disc, in an X-ray reprocessing model. For Mrk 79 and NGC 7469, the optical lag is consistent with zero days, within errors.

iii. The observed rapid optical variations appear to have their origin in reprocessing of X-rays by an optically thick accretion disc and the above results seem to suggest that it is a common occurrence in Seyfert galaxies.

iv. The X-ray and optical light curves are all highly variable. When host galaxy contamination is corrected for in the optical light curves, two galaxies (Mrk 79 and NGC 5548) display a larger fractional variability in the optical than in the X-rays, and another one (NGC 4593) has X-ray and optical variability amplitudes of comparable magnitude. This is inconsistent with a pure reprocessing origin of the optical variations.

v. Reprocessing can only account for the short time-scale (∼days) variability, but it fails to reproduce the variations seen on time-scales of months and longer. It therefore cannot be the only process generating optical variability.

vi. In order to explain the long time-scale optical behaviour observed in these Seyfert galaxies, a separate source of variability is required. The high amplitude, long time-scale variability observed in the optical light curve of Mrk 79 can be reproduced by allowing, in addition to X-ray reprocessing, the accretion rate, the geometry of the X-ray source or the geometry of the accretion disc to vary over time-scales of a ∼year.

vii. There may also be a contribution to the optical emission from radii as far out as the dust torus. The X-ray/optical cross-correlation function of NGC 4051 displays a second statistically significant peak at an optical lag of $39^{+2.7}_{-8.4}$ days. Interpreted as a light travel time, this lag corresponds to the dust sublimation radius in this source. Neither the Wien tail of the reprocessed dust emission or reflection of optical light by the dust can on its own account for the flux associated with the second peak, but I showed that both probably contribute to the optical emission observed from this NLS1 galaxy.

viii. With the current data, the optical PSDs are best described by an unbroken power law model. However, the optical PSDs of five out of the seven galaxies in this sample can be fit with the same bending power law parameters as their X-ray PSDs (up to a normalisation factor and the frequency of the bend) with a high acceptance probability. The bend, if real, appears to be roughly two to three decades lower in frequency in the optical than in the X-rays. The similarity in the power spectral shapes suggests that, although the variations are probably not generated as part of the same emission process, there is nevertheless a close connection between the variations in different bands. Preliminary simulations show that reprocessing of power law irradiation may shift the optical bend to lower frequencies, while keeping the overall shape of the irradiating power law. The bend frequency may also be associated with the viscous time-scale at the optically emitting region of the disc, similar to what is thought to be the case in the X-rays. Both these models predict optical bend frequencies towards the longest time-scales probed in this study, so further monitoring would be required to test these hypotheses. Given the cross-correlation and long time-scale results, the reality is probably a combination of the two.

ix. There is some evidence that the strength of the X-ray/optical correlation varies with accretion disc temperature or black hole mass. This can be understood in terms of the relative locations of the X-ray and optical emitting regions in systems of differing black hole mass and/or accretion rate. High black hole mass/low accretion rate sources have cooler discs, so that the optical emitting region is closer to the centrally concentrated X-ray emitting region, in terms of gravitational radii of the system. This means that their intrinsic variations will be much more closely coupled than in a low black hole mass/high accretion rate system, so that the regions vary coherently, producing a strong correlation. Further work is required to verify this relationship and determine its strength.

6.2 Implications for AGN variability studies

One of the main results of this work is that the observed emission in a particular waveband is not necessarily emitted from just one part of the active nucleus. The optical emission, though primarily generated through viscous dissipation in the accretion disc, is enhanced by external heating from the central X-ray source. Further contributions may come from the Wien tail of the torus emission, reflection by the dust or diffuse emission by the BLR clouds (Korista and Goad, 2001). The same is true for the infrared emission: it is dominated by reprocessing and thermal emission from the dust torus, but a significant contribution may originate in the outer parts of the accretion disc as well (see Section 6.3.3 below).

Hence, in order to model the different emission components, the relative contributions from the disc and torus need to be separated. A similar result has already been presented by Kishimoto et al. (2008) — the infrared emission from the accretion disc in a sample of quasars exhibit the characteristic $\nu^{1/3}$ spectrum expected for an optically thick, locally heated disc. The disc emission is thought to be scattered by a scattering medium in the plane of the disc, so it could be isolated from the dominating torus emission by viewing the system in polarised light. The result presents strong evidence for the existence of a disc and shows that, at least in the outer regions of the disc, the local black body assumption must be a good approximation.

One of the most successful techniques for estimating the mass of the black hole in AGN (especially those in which stellar populations cannot be resolved) is reverberation mapping (Blandford and McKee, 1982; Kaspi et al., 2000; Peterson et al., 2004; Denney et al., 2006; Bentz et al., 2009).

The technique relies on the delay τ between the ionising continuum (usually measured in the form of the optical flux at 5100Å) and the response of different emission lines (notably Hβ), in order to "map" their velocity distribution. The mass of the central black hole is estimated under the assumption that the BLR gas is virialized, so that

$$M_{\rm BH} = \frac{f c \tau (\Delta V)^2}{G} \, . \tag{6.1}$$

f is a scaling constant ~ 1 which depends on the geometry, kinematics and inclination of the BLR and ΔV the velocity dispersion of the line emission.

From large samples of reverberation-mapped AGN, several useful scaling relations have been determined, such as that between the radius of the BLR, $R_{\rm BLR}$ and the central source luminosity, L. In its latest form, it is found that $R_{\rm BLR} \propto L^{0.52}$ (Bentz et al., 2009), which is consistent within errors with the naive expectation that the BLR clouds are all identical in their physical nature (such as density and ionization parameter) and that the emitted energy spectrum of the ionizing source is constant. These assumptions lead to a predicted $R_{\rm BLR} \propto L^{0.5}$ relationship. The advantage of such a scaling relationship is that it allows one to estimate the masses of AGN from a single epoch spectrum.

Work in recent years has focused on detailed modeling of the host galaxy contribution to the luminosity measurements (Bentz et al., 2006, 2009) which artificially steepened the slopes measured in previous analyses (Kaspi et al., 2000; Peterson et al., 2004; Kaspi et al., 2005). However, the scatter of individual points is still $\sim 40\%$ (Bentz et al., 2009). The scatter is usually attributed to internal reddening, as it is known to affect especially the results of NGC 3227.

Central to the assumptions of reverberation mapping is that the continuum emission originates in a single central source and that there is a simple relationship between the measured optical continuum and the ionizing continuum. The cross-correlation result of NGC 4051 presented in Chapter 4 casts doubt on the validity of this assumption in at least that source. A significant peak in the cross-correlation function at 40 days behind the X-rays suggests that there is a significant amount of radiation coming from large radii, possibly associated with the dust torus. If the BLR clouds are significantly heated by emission from large radii, the delay τ will be larger than when assumed to be heated from a central source only, since the emission has to travel from the central source to the torus and back to the BLR. A lag of this magnitude will not be easily detected over the typical reverberation mapping monitoring length (usually a few months), but its influence may be enough to shift the correlation peak to larger τ and hence giving a larger BLR radius, $R_{\rm BLR} = c\tau$.

In a recent reverberation mapping campaign of NGC 4051 (Denney et al., 2009), the BLR was measured to be smaller than the previous estimate (Peterson et al., 2000). Using the Peterson et al. (2000) estimate, NGC 4051 deviates significantly from the best fit $R_{\rm BLR} - L$ line, but the new measurement brings it closer to the current best fit scaling relationship. Various avenues are explored by Denney et al. (2009) to explain the difference in the $R_{\rm BLR}$ measurements, but no conclusive reason is found. I suggest that it is possible that the difference is due to varying contributions of the contaminating emission from large radii to the two measurements. Since the contaminating emission is probably associated with the torus, whose emission depends on the variable central source luminosity, its contribution is expected to change throughout the light curve.

6.3 Future work

6.3.1 Refining the apparent relationship between correlation strength and disc temperature

An obvious first step would be to increase the number of sources on the correlation strength vs. temperature plot (Figure 5.8), in order to confirm the suggested trend. The current sample provides only moderate evidence of a relationship between these parameters. Other members of our research group are working on NGC 4395 (Cameron et al., in preparation), MCG-06-30-15 and NGC 7213 (Arévalo et al., in preparation), so their results will be added as soon as they are available.

Further monitoring would also be possible with the *Swift* Gamma-ray Burst Mission. This multiwavelength space-based observatory is equipped with an X-ray telescope (XRT) and a UV/optical monitor (UVOT), among other detectors, and would be ideal for simultaneous X-ray and optical monitoring of AGN on medium– to long time-scales.

6.3.2 Constraining the optical power spectra

The current data only weakly constrain the shape of the optical power spectra. I have shown in Section 5.3 that all the objects in the sample investigated here are consistent with an unbroken power law model, in which the optical variability power continues to increase towards the longest time-scales probed.

The slopes of the best-fit unbroken power law models are steep ($\alpha > 1.5$) — certainly much steeper than the X-ray power spectra are at similar frequencies ($\alpha \sim 1$). The steep spectra suggests a closer correspondence to the X-ray power spectra above the break frequency. To test this, I also fitted the optical power spectra with a bending power law model, as is found to provide the best description of AGN X-ray PSDs (Markowitz et al., 2003; M^{c}Hardy et al., 2004; Summons, 2008). As the optical data are too poor to constrain all the parameters of the fit, I fixed the high frequency slope to the value measured from the X-ray PSD. This also allows for direct comparison between the X-ray and optical PSDs. The acceptance probabilities of such a bending power law is high in five out of the seven Seyferts in this sample, suggesting that the optical PSDs could be similar in shape to the X-rays. A similarity in the PSDs would be highly suggestive of a common, or closely related, mechanism underlying the X-ray and optical variations. Although the acceptance probabilities are formally high, the bend frequency cannot be constrained by the current data. The best fit places the break frequency towards the longest time-scales sampled, suggesting, firstly, that the current data have a definite preference for a simple unbroken model, and secondly, that if there is a break, it is at lower frequencies than the X-ray break. Further long time-scale monitoring would be required to test this hypothesis.

An instructive next step would be to investigate whether optical fluctuations generated in the way suggested by Lyubarskii (1997) (discussed in Section 5.3.3) can produce the steep slopes seen in optical power spectra. The model of Churazov et al. (2001) lends support to a viscous origin of the bend frequency, and given that the viscous time-scale is much longer at the optically emitting part of the disc, a lower frequency break may be expected if the X-ray and optical power spectra have a common or related origin. Composite models combining the effects of reprocessing and inward propagating long time-scale fluctuations could now be compared to the observed PSDs. An additional advantage is that these models can be studied over longer time-scales than the current observations, so that predictions may be made or estimates of the length of the additional monitoring required to show the predicted PSD features (such as a break).

The targets are all relatively bright and this is a project which can be carried out with great success on small telescopes. The large field of view that smaller telescopes often have will also aid in getting more suitable PSF stars into the field for more accurate image subtraction (Section 2.2.4).

6.3.3 The disc contribution to the NIR emission

Since the discovery of a 400 day delay between the UV and infrared variations in the Seyfert 1 galaxy Fairall 9 (Clavel et al., 1989), consistent with dust reverberation models (Barvainis, 1987), the general consensus has been that the NIR emission in AGN was due to dust reprocessing of short wavelength emission from the central source.

Models interpret the long delay as the light travel time from the centre of the system to the inner 'edge' of the dust torus, which is determined by the ionising luminosity and the sublimation temperature of the dust (1500–2000K). Observations show reasonable agreement with with this model (Oknyanskij and Horne, 2001; Glass, 2004; Suganuma et al., 2006), with the NIR emission following the optical on time-scales of months.

However, it follows directly from the radial temperature profile of the disc

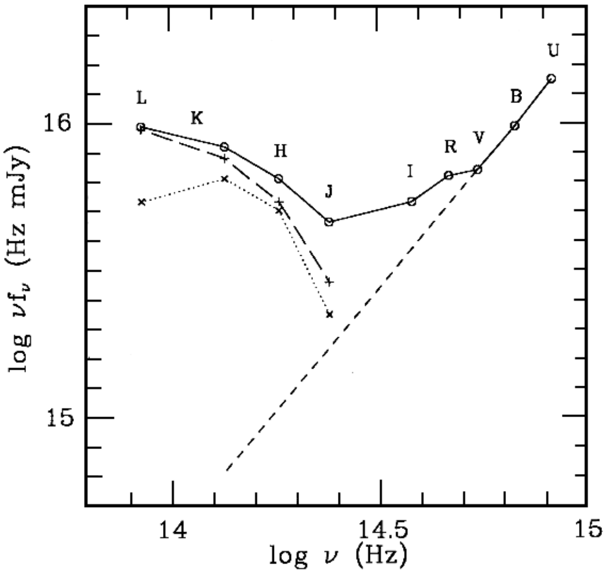

Figure 6.1: Average optical to NIR spectral energy distribution of NGC 3783. The short-dashed line is the extrapolation of the *UBV* power law to estimate its contribution to the NIR bands. The long-dashed lined represents the shape of the NIR component after subtracting the power law contribution. The dotted line represents a 1500 K blackbody. From Glass (1992).

(Eqn. 1.3), that the outer disc may contribute to the NIR emission as well, especially in those systems with a very massive black hole or low accretion rate.

This possibility has been noted before by Glass (1992). Figure 6.1 shows the SED of NGC 3783 from that paper. By extrapolating the *UBV* power law, its contribution to each of the NIR bands can be estimated and subtracted. There is only a small disc contribution to the *K* band in this source, but the contribution to the *J* band is considerable. After subtracting the disc contribution, the NIR component shows much closer agreement with a 1500 K blackbody, used as an approximate model for the torus emission. Tomita et al. (2006) reaches a similar conclusion for MCG-08-11-011.

Our initial monitoring of NGC 3783 with the SMARTS telescope in Chile, supports this conclusion: the *J* band light curve shows short time-scale variations similar to what is seen in the *B* band (which is thought to originate entirely in the disc), but the *K* band light curve is smooth and delayed with respect to the *B* band, indicating that most of this emission originates from the dust (Lira et al., in preparation).

In Section 5.5 I have shown that there is some evidence for a temperature dependence of the strength of the X-ray/optical correlation. We can now extend this to the infrared and investigate how the strength of the disc NIR contribution depends on the mass of the central black hole.

6.3.4 Temperature variation of the dust

The exact composition of AGN dust is uncertain, but it is thought to consist mostly of graphite and silicate grains, with sublimation temperatures ranging between 1500 – 2000 K (Draine and Lee, 1984). The sublimation radius, where this temperature is reached, scales as $L^{0.5}$ (Barvainis, 1987; Nenkova et al., 2008a), so the lag $\Delta\tau$ between the continuum and IR variations is also expected to scale as $L^{0.5}$.

The recombination of dust particles occurs over a much longer time-scale (∼year, Koshida et al., 2009) than the sublimation, so the inner radius of the torus is determined by the most recent large flare of the X-ray/UV emission.

Consider dust at the inner radius of the torus, close to, but below the sublimation temperature. The temperature of this dust may be estimated from the observed infrared colour. Now suppose the temperature is raised a little further, e.g. by a UV flare reaching the torus. The dust will be destroyed effectively instantaneously, increasing the size of the dust-free zone and revealing the cooler dust behind it. (AGN are observed to have a steep temperature gradient in the near- to far-infrared. This is one of the main arguments for the torus to be consist of clumps of optically thick dust, rather than a smooth distribution. The clumps can shield each other from direct irradiation by the central source, creating a steep temperature gradient in the torus.)

In principle, this should be observable as a sudden change in colour temperature of the dust. If this change is large enough, it should show a direct relationship with the largest X-ray/UV flares and perhaps also a recovery time-scale for the dust to heat up to the sublimation temperature again. This will also enable us to put tighter constraints on the dust composition if certain types/sizes of particles can be ruled out based on the maximum temperature it can sustain before being destroyed by the continuum radiation.

6.4 A final remark

It is clear from this study that variations in AGN occur on a broad range of time-scales. The observed variability is cumulative result of distinct processes, and insufficient temporal coverage may easily lead to misinterpretation of the physical processes at work. The array of apparently contradicting results reported in literature testifies to this fact. A clear picture is only starting to emerge because of the availability of long (several years), well sampled light curves. AGN time-scales, especially in the optical emitting region, are long, and this study underlines the importance of long term monitoring to understand not only origin of the variations and the relationship between different emission regions, but to gain a complete understanding of the working of active galaxies.

APPENDICES

A Cross-correlation functions

A.1 Basic theory

The cross-correlation function is a standard statistical technique used to quantify the degree of linear correspondence between two time series, as they are shifted in time with respect to each other.

If the X-ray and optical emission from active galaxies are related through a physical process, one may expect the variations in the light curves to be correlated. For example, if the optical variations in Seyfert galaxies are the result of reprocessing of the highly variable X-ray emission, we expect the variations in the optical band to follow the X-ray variations with a short delay. The delay in this case corresponds to the light travel time from the X-ray source to the optical emitting region of the disc. If instead the optical variations are mainly due to variations intrinsic to the disc, such as accretion rate fluctuations, the optical will be observed to lead the variations in the X-ray light curve. Such variations will propagate inward through the disc on the viscous time-scale, first reaching the optical emitting regions and later the X-ray emitting region at the innermost part of the system. Hence the delay in this case is expected to be much longer than in the reprocessing scenario, and of opposite sign. Another possibility is that disc UV/optical photons are Compton up-scattered into X-ray energies by a hot corona above the inner disc. The direct link between the UV/optical photons available to be up-scattered and the resulting X-rays, is expected to manifest as a short delay of the X-ray variations behind the UV/optical emission.

Comparing the light curves from simultaneous X-ray and optical monitoring, could therefore in principle provide a method for determining the sign of the delay and allow us to determine which the dominant process underlying the optical variability is.

A frequent application of cross-correlation analysis in astronomy is *reverberation mapping* of AGN, where the relationship between the optical continuum and BLR emission lines is used to derive the mass of the central black hole. The use of cross-correlation functions in astronomy has been discussed by many authors, e.g. Gaskell and Peterson (1987), White and Peterson (1994), Welsh (1999), Zhang et al. (2004), Suganuma et al. (2006). The discussion presented here is based partially on the discussion by Peterson (2001).

Let the irradiating light curve (assumed to be the X-rays) be denoted $I(t)$ and the response light curve (optical) $R(t)$. The relationship between them may be written as

$$R(t) = \int \Psi(\tau) I(t-\tau)\, d\tau \tag{A1}$$

where $\Psi(\tau)$ is the transfer function at a delay τ. This transfer function contains all the information related to the physical response of the optical emitting region, including the time delay between variations in $I(t)$ and $R(t)$, as well as the smoothing of the fast variations of $I(t)$ by the geometry of the responding emission region.

The autocorrelation function (ACF) describes how well a function is related to itself at a delay τ, or equivalently, how much the value of $I(t+\tau)$ depends on $I(t)$. Similarly, the cross-correlation (CCF) describes the linear dependence of one light curve on another at a delay τ.

$$\mathrm{ACF}(\tau) = \int I(t) I(t-\tau)\, dt \tag{A2}$$

$$\mathrm{CCF}(\tau) = \int R(t) I(t-\tau)\, dt \tag{A3}$$

The ACF in Eqn. A2 is written for the irradiating light curve, but the ACF of the response light curve may of course be calculated in the same way. Using Eqn. A1, the CCF may also be written as

$$\begin{aligned} \mathrm{CCF}(\tau) &= \iint \Psi(\tau') I(t-\tau') I(t-\tau)\, d\tau'\, dt \\ &= \int \Psi(\tau') \mathrm{ACF}(\tau-\tau')\, d\tau' \end{aligned} \tag{A4}$$

so that the CCF may also be viewed as the convolution of the irradiating ACF with the transfer function Ψ.

It is instructive to rewrite Eqn. A3 as follows[1]:

$$\mathrm{CCF}(\tau) = \frac{1}{2}\int [R(t)]^2\, dt + \frac{1}{2}\int [I(t-\tau)]^2\, dt - \frac{1}{2}\int [R(t) - I(t-\tau)]^2\, dt\ . \quad \text{(A5)}$$

The first two terms are approximately constant if the integration range is much larger than the delay τ. Therefore it is the third term which determines the shape of the correlation — when there is a large difference between the light curves I and R (at a given delay τ), Eqn. A5 is a minimum. When the light curves correspond to each other closely, the value of $R(t) - I(t-\tau)$ is a minimum, and the sum in Eqn. A5 a maximum.

The correlation function is usually normalised such that $\mathrm{ACF}(0) = 1$. The value of the normalised correlation coefficient $\mathrm{CCF}(\tau)$ is then indicative of the strength of the correlation at a delay τ.

A.2 Cross-correlation of astronomical time series

The relations in the previous section are strictly only true for continuous functions and infinite limits of integration. In practice we are almost always calculating the correlation between two discretely sampled time series when dealing with observational data, so we use the discrete form of the correlation function. For example, if we denote the X-ray light curve by X and the optical by V, then their correlation function is given by

$$\mathrm{CCF}(\tau) = \frac{1}{N}\sum_{i=1}^{N} \frac{[X(t_i) - \langle X\rangle][V(t_i-\tau) - \langle V\rangle]}{\sqrt{(\sigma_X^2 - e_X^2)(\sigma_V^2 - e_V^2)}} \quad \text{(A6)}$$

where N is the number of pairs of observations in the light curves. The mean of each light curve $\langle X\rangle$ and $\langle V\rangle$ is subtracted, and the sum normalised by the product of the standard deviations of the two light curves, corrected for observational noise.

---

[1] Using the fact that $2xy = x^2 + y^2 - (x-y)^2$

The standard deviation has the standard definition,

$$\sigma_X = \sqrt{\frac{1}{N_X}\sum_{i=1}^{N_X}(X_i - \langle X\rangle)^2}, \tag{A7}$$

and the average squared error is given by

$$e_X^2 = \frac{1}{N_X}\sum_{i=1}^{N_X}(\Delta X_i)^2, \tag{A8}$$

with similar expressions for the V band light curve.

Calculating the correlation function like this requires evenly spaced data points, so that each point in one light curve may be paired with a data point in the other. This is of course nearly impossible to achieve with astronomical observations, especially over the time-scales over which AGN have to be observed to probe the wide range of variability time-scales. Apart from the obvious difficulty of carrying out the observations at regularly spaced intervals over several weeks or years, most observations are interrupted by the source going into solar conjunction. Additionally, ground based observations will always be affected by poor weather conditions from time to time, even at the best observing sites. Several methods have been developed to try and deal with this problem, so that the cross-correlation between two discretely, irregularly sampled light curves, may be calculated reliably. I will briefly discuss those methods below, as well as their strengths and weaknesses.

Interpolation Cross-Correlation Function (ICCF)

One way to achieve regular spacing of the data, especially for well-sampled light curves, is to interpolate the light curves with a piecewise linear function and then resample them with time step $\Delta\tau$ to obtain equally spaced data points. This method is one interpretation of what is known as the interpolation cross-correlation function. In what follows, I will refer to this method as the "equally sampled" (EQ) method. Alternatively, one may interpolate only one of the light curves to obtain the fluxes at times $t-\tau$, i.e. calculate the flux pairs $(X(t), V(t-\tau))$ or $(X(t-\tau), V(t))$. This is the is the version of the ICCF originally used by Gaskell and Sparke (1986) (but see also Gaskell and Peterson, 1987, for caveats). In general, the correlation is calculated by interpolating each light curve in turn and then averaging the resulting CCFs. The method was adapted by White and Peterson (1994), who pointed out that points outside the time series (i.e. $t_i - \tau <$

t_{start} or $t_i + \tau > t_{\text{end}}$ should be omitted from the calculation, rather than taken to be equal to t_{start} or t_{end}, as was done in the original implementation. I will follow Suganuma et al. (2006) and call this the "bi-directionally interpolated" (BI) method.

The obvious disadvantage of the interpolation method is that gaps in the light curve are interpolated over in a linear fashion, which is generally not a good description of the real behaviour of the light curve and may produce misleading results. An interesting alternative approach, suggested by Suganuma et al. (2006), is to realise a distribution of simulated flux variations in the gaps, based upon the structure function[2] of the light curves. From this distribution, an error on the lag may be calculated by comparing it to the CCF of the observed light curves.

The bi-directionally interpolated method sometimes produce noisy peaks, especially when the variations in the light curve(s) are undersampled. The equally sampled method removes this problem, but is more prone to inaccuracies, as it relies entirely on interpolated data points. The observed data is effectively given more weight than the interpolated data when using the BI method, so it is the preferred implementation.

In cases where there is reason to prefer one direction of interpolation above the other, e.g. when one light curve is much better sampled than the other, one may choose to interpolate only one of the light curves. I will refer to this case as the "single interpolation" (SI) method. The greatest criticism of the SI method is that it is likely to produce an asymmetric ACF, due to the irregular sampling. However, in some cases it might be the more accurate way of calculating the correlation. An example is the X-ray and optical light curves used here. Not only are most of the X-ray light curves better sampled than the optical light curves, but the variations of the optical light curves are generally smoother than that of the X-rays, so interpolating over small gaps in the optical light curves is much closer to the true behaviour of the light curve than it is for the X-rays. It is therefore more appropriate to interpolate just the optical light curve to the times $t_i - \tau$ required by the correlation calculation, rather than interpolating both and averaging the CCFs.

---

[2] The structure function is similar to the PSD in the sense that it shows the variability power in a light curve as a function of time-scale. However, unlike the PSD, it is calculated entirely in the time domain.

Discrete Correlation Function (DCF)

Linear interpolation over long gaps in the light curve is rarely an acceptable description of the actual variability behaviour of the light curve, and hence may produce spurious results in the CCF. To avoid such interpolations, Edelson and Krolik (1988) developed a method which only uses the real data points for calculating the correlation. They achieve this by calculating a set of "unbinned discrete correlation coefficients" for each pair of fluxes $(X(t_i), V(t_j))$, with associated time separation $\Delta t_{ij} = t_i - t_j$,

$$\mathrm{UDCF}_{ij} = \frac{[X(t_i) - \langle X\rangle]\,[V(t_j) - \langle V\rangle]}{\sigma_X \sigma_V} \tag{A9}$$

The correlation coefficients UDCF_{ij} are then binned in bins of equal time width $\Delta\tau$ and the points contributing to that bin averaged, such that

$$\mathrm{DCF}(\tau) = \frac{1}{n}\,\mathrm{UDCF}_{ij} \tag{A10}$$

where n is the number of points in the lag bin $\tau - \frac{\Delta\tau}{2} < \Delta t_{ij} < \tau + \frac{\Delta\tau}{2}$.

The bin size $\Delta\tau$ is a compromise between having enough points in a bin so that the average is an accurate representation of $\mathrm{DCF}(\tau)$, and choosing the bin size small enough to maintain a high enough time resolution of the correlation function.

In the limit of good sampling, the ICCF and DCF perform equally well (Edelson and Krolik, 1988; White and Peterson, 1994; Zhang et al., 2004), but for light curves with large gaps in the data, the DCF is probably the superior choice. Note that because of the binning of the correlation function, the DCF does however require more data points than the ICCF to uncover a correlation. The results from the ICCF in this case are still correct and valid as long as the interpolation is a reasonable approximation of the real behaviour of the light curve.

A variation on this method was presented by Alexander (1997), called the z-transformed discrete correlation function, or zDCF. This method bins the correlation function in bins with an equal number of points per bin, rather than in bins of equal time width. It then applies the statistical Fisher's z-transform to the points in the bin to make an improved estimate of the error on the correlation. The zDCF is claimed to be 2–3 times more efficient at finding a correlation in sparsely sampled light curves, compared to the original DCF algorithm (Alexander, 1997).

My approach in this thesis

Which CCF to use? is an often-asked question, but it does not have a straightforward answer. It is probably best decided by considering the sampling and variability properties of the data as well as the expected outcome (e.g. the size of the lag) of the cross-correlation analysis.
My main considerations for the cross-correlation analysis in this thesis were:

- I needed to make a reliable estimate of the delay between the variations in different bands, often in the presence of uncorrelated long time-scale variations.
- The sampling of the light curves are similar to the expected delays.
- The sampling of both the X-ray and optical light curves are irregular.
- The light curves are sampled at different times and with different frequencies of observation.
- The X-ray and optical light curves have very different variability properties — there is much more variability on short time-scales in the X-ray light curves than in the optical. Some optical light curves have considerable power on long time-scales, which is not present in the X-rays.
- I wanted to use the real data as far as possible, rather than resampling the light curves or making assuptions about the variability behaviour.
- I needed to understand which features, if any, in the CCFs were artefacts of the sampling pattern(s), rather than due to the real variability of the light curves.
- All light curves (X-ray and optical) have gaps of several weeks to months on an ∼annual time-scale, due to solar conjunction, plus some smaller gaps due to bad weather or instrumentation problems.

At first the DCF seems to be the most attractive method, for its advantage of using only the real data. Unfortunately, in order to obtain a reliable peak in the DCF (i.e. enough signal-to-noise in each DCF bin), the bin size had to be large (∼4–6 days), so all time resolution on time-scales shorter than this was lost. Since the expected lag is only ∼1–2 days, the delay between the two bands could not be measured precisely using this method. The same holds for the zDCF.

I therefore selected the SI method (or in some cases the BI method, depending on the sampling of the light curves and the measurement errors) to calculate the correlation functions. The DCF and zDCF are however useful as a check — large differences in the DCF and ICCF over the time-scales of interest, probably indicate that too much emphasis is placed on interpolated data or that the interpolated data are not an acceptable representation of the light curve. In all cases I found the two methods to give consistent results.

Selecting the ICCF to calculate the correlations of course then introduces the problems associated with long gaps in the light curves. In order to take account of this, I broke the light curves into shorter segments, defined by these gaps. I then calculate the ICCF for each optical segment with its corresponding X-ray segment and average the resulting CCFs together. To ensure that e.g. one strong peak in a short segment of data does not artificially dominate the correlation, I weight each component CCF by the length (in time) of the light curve segments from which it was calculated.

Breaking the light curves into segments like this effectively removes variability power on time-scales longer than the segments (here generally $\sim$1–2 yr). This narrows the peak of the CCF and allows one to make an improved estimate of the short time-scale lag. For the same reason, Welsh (1999) suggests removing a linear function from the light curve to remove the long time-scale power — a technique known as “pre-whitening”. However, I prefer the method of segmenting the light curves, as this also removes the problem of gaps in the light curve.

Finally, I calculate the statistical significance of the peak using Monte Carlo simulations (described in Section 3.3, 4.4.1 and 5.4.1). The error on the lag is calculated using the bootstrap method of Peterson et al. (1998a).

Throughout this thesis I use a positive value on the lag axis to indicate a lag of the longer wavelength emission behind the shorter wavelength emission.

B Symbols and abbreviations

B.1 List of constants and symbols used

c – speed of light, 299 792 458 m s^{-1}
c_s – sound speed
D – distance to source in mks units
G – universal gravitational constant, 6.673×10^{-11} m^3 $\mathrm{kg}^{-1}\mathrm{s}^{-2}$
h – Planck's constant, 6.626×10^{-34} $\mathrm{m}^2\mathrm{kg\,s}^{-1}$
h_X – height of the X-ray source above the accretion disc, in units of R_g
k – Boltzmann's constant, 1.381×10^{-23} $\mathrm{m}^2\mathrm{kg\,s}^{-2}\mathrm{K}^{-1}$
kpc – kiloparsec, 3.085×10^{19} m
i – inclination angle to the observer
L_{bol} – bolometric luminosity
L_{Edd} – Eddington luminosity
L_{ion} – ionising luminosity, $\sim$13.6 eV – 13.6 keV
L_{X} – X-ray luminosity
$\dot{m}$ – disc accretion rate as a fraction of the Eddington rate
$\dot{M}$ – disc accretion rate in mks units
m – black hole mass in units of solar mass $M_\odot$
M – black hole mass in mks units
Mpc – megaparsec, 3.085×10^{22} m
r – radius, in mks units
R – radius, in units of R_g
R_{in} – disc inner radius, in units of R_g
$M_\odot$ – solar mass, 1.989×10^{30} kg
$\dot{m}$ – accretion rate as a fraction of the Eddington accretion rate
m_p – proton mass, $1.67262158 \times 10^{-27}$ kg

$\dot{M}_{\rm Edd}$ – Eddington accretion rate
R_g – gravitational radius
T – total irradiated disc temperature, $T = (T_d^4 + T_x^4)^{1/4}$
T_d – accretion disc temperature
T_x – temperature associated with the X-ray irradiation of the disc
z – redshift
α – power law index of the variability power density spectrum
$\alpha_{\rm disc}$ – disc viscosity parameter
λ – wavelength of the radiation
ν – frequency of the radiation
σ – Stefan-Boltzmann constant, 5.6704×10^{-8} W m^{-2}K^{-4}
σ_T – Thomson cross-section, 6.65×10^{-25} cm^2
τ_K – Kendall tau rank correlation coefficient
ζ – viscosity

B.2 Abbreviations

A&A – Astronomy & Astrophysics (journal)
ACF – Auto-Correlation Function
ACS – Advanced Camera for Surveys, on board HST
ADAF – Advection Dominated Accretion Flow
AGN – Active Galactic Nucleus/Nuclei
AJ – Astronomy Journal
ApJ – Astrophysical Journal
ASCA – Advanced Satellite for Cosmology and Astrophysics
ASP – Astronomical Society of the Pacific
BI – Bi-directionally interpolated method of calculating the ICCF
BLR – Broad Line Region
CCF – Cross-Correlation Function
CrAO – Crimean Astrophysical Observatory
DCF – Discrete Correlation Function
DFT – Discrete Fourier Transform
EQ – Equally sampled method of calculating the ICCF
Eqn. – Equation
EUV – Extreme Ultraviolet
Fig. – Figure
FIR – Far-infrared, $\lambda \sim 30 - 300\ \mu$m
FRRSS – Flux Randomization/Random Subset Selection method for calculating the error on the CCF lag
FT – Faulkes Telescope
FWHM – Full Width (of radial flux profile) at Half Maximum (of the intensity)

HEASARC	–	NASA's High Energy Astrophysics Science Archive Research Centre
HST	–	Hubble Space Telescope
ICCF	–	Interpolation Cross-Correlation Function
IR	–	Infrared
IUE	–	International Ultraviolet Explorer
LINER	–	Low Ionization Nuclear Emission Region
LT	–	Liverpool Telescope
MAGNUM	–	Multicolour Active Galactic NUclei Monitoring project
MAST	–	Multi-mission Archive at the Space Telescope Science Institute
MNRAS	–	Monthly Notices of the Royal Astronomical Society
MJD	–	Modified Julian Date, i.e. Julian Date–2400000.5
Mrk	–	The Markarian Catalogue of galaxies
NASA	–	The American National Aeronautical and Space Administration
NGC	–	The New General Catalogue of galaxies
NIR	–	Near-infrared, $\lambda \sim 1 - 5\ \mu$m
NLR	–	Narrow Line Region
NLS1	–	Narrow-line Seyfert 1 galaxy
PASP	–	Publications of the Astronomical Society of the Pacific
PSD	–	Power Spectral Density
PSF	–	Point Spread Function
PCA	–	Proportional Counter Array on board *RXTE*
PCU	–	A Proportional Counter Unit, part of the PCA detector on *RXTE*
QSO	–	Quasi-stellar object
rms	–	Root-mean-squared
RXTE	–	Rossi X-ray Timing Explorer
SED	–	Spectral Energy Distribution
SDSS	–	Sloan Digital Sky Survey
SMBH	–	Supermassive Black Hole, M$\sim 10^5 - 10^9 M_\odot$
SI	–	Single interpolation method of calculating the ICCF
UV	–	Ultraviolet
zDCF	–	z-transformed Discrete Correlation Function

Bibliography

Akritas, M. G. and Siebert, J.: 1996, *MNRAS* **278**, 919

Alard, C.: 2000, *A&AS* **144**, 363

Alard, C. and Lupton, R. H.: 1998, *ApJ* **503**, 325

Alexander, T.: 1997, in D. Maoz, A. Sternberg, and E. M. Leibowitz (eds.), *Astronomical Time Series*, Vol. 218 of *Astrophysics and Space Science Library*, p. 163

Antonucci, R. R. J. and Miller, J. S.: 1985, *ApJ* **297**, 621

Arévalo, P. and Uttley, P.: 2006, *MNRAS* **367**, 801

Arévalo, P., Uttley, P., Kaspi, S., Breedt, E., Lira, P., and M^{c}Hardy, I. M.: 2008, *MNRAS* **389**, 1479

Arévalo, P., Uttley, P., Lira, P., Breedt, E., M^{c}Hardy, I. M., and Churazov, E.: 2009, *MNRAS* **397**, 2004

Balbus, S. A. and Hawley, J. F.: 1991, *ApJ* **376**, 214

Barvainis, R.: 1987, *ApJ* **320**, 537

Bentz, M. C., Denney, K. D., Cackett, E. M., Dietrich, M., Fogel, J. K. J., Ghosh, H., Horne, K. D., Kuehn, C., Minezaki, T., Onken, C. A., Peterson, B. M., Pogge, R. W., Pronik, V. I., Richstone, D. O., Sergeev, S. G., Vestergaard, M., Walker, M. G., and Yoshii, Y.: 2007, *ApJ* **662**, 205

Bentz, M. C., Peterson, B. M., Netzer, H., Pogge, R. W., and Vestergaard, M.: 2009, *ApJ* **697**, 160

Bentz, M. C., Peterson, B. M., Pogge, R. W., Vestergaard, M., and Onken, C. A.: 2006, *ApJ* **644**, 133

Berkley, A. J., Kazanas, D., and Ozik, J.: 2000, *ApJ* **535**, 712

Bica, E.: 1988, *A&A* **195**, 76

Blandford, R. D. and McKee, C. F.: 1982, *ApJ* **255**, 419

Breedt, E., Arévalo, P., M^{c}Hardy, I. M., Uttley, P., Sergeev, S. G., Minezaki, T., Yoshii, Y., Gaskell, C. M., Cackett, E. M., Horne, K., and Koshida, S.: 2009, *MNRAS* **394**, 427

Cackett, E. M., Horne, K., and Winkler, H.: 2007, *MNRAS* **380**, 669

Churazov, E., Gilfanov, M., and Revnivtsev, M.: 2001, *MNRAS* **321**, 759

Clavel, J., Nandra, K., Makino, F., Pounds, K. A., Reichert, G. A., Urry, C. M., Wamsteker, W., Peracaula-Bosch, M., Stewart, G. C., and Otani, C.: 1992, *ApJ* **393**, 113

Clavel, J., Wamsteker, W., and Glass, I. S.: 1989, *ApJ* **337**, 236

Cohen, M. H. and Martel, A. R.: 2002, in D. M. Crenshaw, S. B. Kraemer, and I. M. George (eds.), *Mass Outflow in Active Galactic Nuclei: New Perspectives*, Vol. 255 of *ASP Conference Series*, p. 255

Collier, S., Horne, K., Wanders, I., and Peterson, B. M.: 1999, *MNRAS* **302**, L24

Collier, S. and Peterson, B. M.: 2001, *ApJ* **555**, 775

Collier, S. J., Horne, K., Kaspi, S., Netzer, H., Peterson, B. M., Wanders, I., Alexander, T., Bertram, R., Comastri, A., Gaskell, C. M., Malkov, Y. F., Maoz, D., Mignoli, M., Pogge, R. W., Pronik, V. I., and et al: 1998, *ApJ* **500**, 162

Collin-Souffrin, S.: 1991, *A&A* **249**, 344

Czerny, B., Schwarzenberg-Czerny, A., and Loska, Z.: 1999, *MNRAS* **303**, 148

Darnley, M. J., Kerins, E., Newsam, A., Duke, J. P., Gould, A., Han, C., Ibrahimov, M. A., Im, M., Jeon, Y.-B., Karimov, R. G., Lee, C.-U., and Park, B.-G.: 2007, *ApJ* **661**, L45

Davies, R. I., Tacconi, L. J., and Genzel, R.: 2004, *ApJ* **602**, 148

De Rosa, A., Piro, L., Fiore, F., Grandi, P., Maraschi, L., Matt, G., Nicastro, F., and Petrucci, P. O.: 2002, *A&A* **387**, 838

Denney, K. D., Bentz, M. C., Peterson, B. M., Pogge, R. W., Cackett, E. M., Dietrich, M., Fogel, J. K. J., Ghosh, H., Horne, K. D., Kuehn, C., Minezaki, T., Onken, C. A., Pronik, V. I., Richstone, D. O., Sergeev, S. G., Vestergaard, M., Walker, M. G., and Yoshii, Y.: 2006, *ApJ* **653**, 152

Denney, K. D., Watson, L. C., Peterson, B. M., Pogge, R. W., Atlee, D. W., Bentz, M. C., Bird, J. C., Brokofsky, D. J., Comins, M. L., Dietrich, M., Doroshenko, V. T., Eastman, J. D., Efimov, Y. S., Gaskell, C. M., Hedrick, C. H., Klimanov, S. A., Klimek, E. S., Kruse, A. K., Lamb, J. B., Leighly, K., Minezaki, T., Nazarov, S. V., Petersen, E. A., Peterson, P., Poindexter, S., Schlesinger, Y., Sakata, K. J., Sergeev, S. G., Tobin, J. J., Unterborn, C., Vestergaard, M., Watkins, A. E., and Yoshii, Y.: 2009, *ApJ* **702**, 1353

di Matteo, T.: 1998, *MNRAS* **299**, L15

Done, C., Ward, M. J., Fabian, A. C., Kunieda, H., Tsuruta, S., Lawrence, A., Smith, M. G., and Wamsteker, W.: 1990, *MNRAS* **243**, 713

Doroshenko, V. T., Sergeev, S. G., Merkulova, N. I., Sergeeva, E. A., Golubinsky, Y. V., Pronik, V. I., and Okhmat, N. N.: 2005a, *Astrophysics* **48**, 156

Doroshenko, V. T., Sergeev, S. G., Merkulova, N. I., Sergeeva, E. A., Golubinsky, Y. V., Pronik, V. I., and Okhmat, N. N.: 2005b, *Astrophysics* **48**, 304

Draine, B. T.: 2003, *ApJ* **598**, 1017

Draine, B. T. and Lee, H. M.: 1984, *ApJ* **285**, 89

Edelson, R., Koratkar, A., Nandra, K., Goad, M., Peterson, B. M., Collier, S., Krolik, J., Malkan, M., Maoz, D., O'Brien, P., Shull, J. M., Vaughan, S., and Warwick, R.: 2000, *ApJ* **534**, 180

Edelson, R. A., Alexander, T., Crenshaw, D. M., Kaspi, S., Malkan, M. A., Peterson, B. M., Warwick, R. S., Clavel, J., Filippenko, A. V., Horne, K., Korista, K. T., and 81 co-authors part of the AGN Watch consortium.: 1996, *ApJ* **470**, 364

Edelson, R. A. and Krolik, J. H.: 1988, *ApJ* **333**, 646

Fanaroff, B. L. and Riley, J. M.: 1974, *MNRAS* **167**, 31P

Frank, J., King, A., and Raine, D. J.: 2002, *Accretion Power in Astrophysics: Third Edition*, Cambridge University Press, February 2002.

Gaskell, C. M.: 2006, in C. M. Gaskell, I. M. M^{c}Hardy, B. M. Peterson, and S. G. Sergeev (eds.), *Astronomical Society of the Pacific Conference Series*, Vol. 360, p. 111

Gaskell, C. M.: 2007, in L. C. Ho and J.-W. Wang (eds.), *The Central Engine of Active Galactic Nuclei*, Vol. 373 of *ASP Conference Series*, p. 596

Gaskell, C. M.: 2008, in *Revista Mexicana de Astronomia y Astrofisica Conference Series*, Vol. 32, pp 1–11

Gaskell, C. M. and Peterson, B. M.: 1987, *ApJS* **65**, 1

Gaskell, C. M. and Sparke, L. S.: 1986, *ApJ* **305**, 175

George, I. M. and Fabian, A. C.: 1991, *MNRAS* **249**, 352

Glass, I. S.: 1992, *MNRAS* **256**, 23P

Glass, I. S.: 2004, *MNRAS* **350**, 1049

Goosmann, R. W. and Gaskell, C. M.: 2007, *A&A* **465**, 129

Haardt, F. and Maraschi, L.: 1991, *ApJ* **380**, L51

Halpern, J. P.: 1984, *ApJ* **281**, 90

Ho, L. C., Filippenko, A. V., and Sargent, W. L. W.: 1997, *ApJ* **487**, 568

Howell, S. B.: 2006, *Handbook of CCD astronomy*, Cambridge University Press, 2006 ISBN 0521852153

Jahoda, K., Markwardt, C. B., Radeva, Y., Rots, A. H., Stark, M. J., Swank, J. H., Strohmayer, T. E., and Zhang, W.: 2006, *ApJS* **163**, 401

Kaspi, S., Maoz, D., Netzer, H., Peterson, B. M., Vestergaard, M., and Jannuzi, B. T.: 2005, *ApJ* **629**, 61

Kaspi, S., Smith, P. S., Netzer, H., Maoz, D., Jannuzi, B. T., and Giveon, U.: 2000, *ApJ* **533**, 631

Kazanas, D. and Nayakshin, S.: 2001, *ApJ* **550**, 655

Kendall, M. G.: 1970, *Rank Correlation Methods*, Griffin, London, ISBN 0852641990

Kishimoto, M., Antonucci, R., Blaes, O., Lawrence, A., Boisson, C., Albrecht, M., and Leipski, C.: 2008, *Nature* **454**, 492

Klimek, E. S., Gaskell, C. M., and Hedrick, C. H.: 2004, *ApJ* **609**, 69

Kollatschny, W.: 2003, *A&A* **407**, 461

Koratkar, A. and Blaes, O.: 1999, *PASP* **111**, 1

Korista, K. and Ferland, G.: 1998, *ApJ* **495**, 672

Korista, K. T. and Goad, M. R.: 2001, *ApJ* **553**, 695

Koshida, S., Yoshii, Y., Kobayashi, Y., Minezaki, T., Sakata, Y., Sugawara, S., Enya, K., Suganuma, M., Tomita, H., Aoki, T., and Peterson, B. A.: 2009, *ApJ* **700**, L109

Krolik, J. H., Horne, K., Kallman, T. R., Malkan, M. A., Edelson, R. A., and Kriss, G. A.: 1991, *ApJ* **371**, 541

Lamer, G., Uttley, P., and M^{c}Hardy, I. M.: 2000, *MNRAS* **319**, 949

Lu, Y. and Wang, T.: 2000, *ApJ* **537**, L103

Lyubarskii, Y. E.: 1997, *MNRAS* **292**, 679

Maoz, D., Edelson, R., and Nandra, K.: 2000, *AJ* **119**, 119

Maoz, D., Markowitz, A., Edelson, R., and Nandra, K.: 2002, *AJ* **124**, 1988

Markowitz, A., Edelson, R., Vaughan, S., Uttley, P., George, I. M., Griffiths, R. E., Kaspi, S., Lawrence, A., M^{c}Hardy, I., Nandra, K., Pounds, K., Reeves, J., Schurch, N., and Warwick, R.: 2003, *ApJ* **593**, 96

Markowitz, A., Reeves, J. N., George, I. M., Braito, V., Smith, R., Vaughan, S., Arévalo, P., and Tombesi, F.: 2009, *ApJ* **691**, 922

Mason, K. O., M^{c}Hardy, I. M., Page, M. J., Uttley, P., Córdova, F. A., Maraschi, L., Priedhorsky, W. C., Puchnarewicz, E. M., and Sasseen, T.: 2002, *ApJ* **580**, L117

Mihov, B. M. and Slavcheva-Mihova, L. S.: 2008, *Astronomische Nachrichten* **329**, 418

Miller, C. J., Nichol, R. C., Gómez, P. L., Hopkins, A. M., and Bernardi, M.: 2003, *ApJ* **597**, 142

Minezaki, T., Yoshii, Y., Kobayashi, Y., Enya, K., Suganuma, M., Tomita, H., Aoki, T., and Peterson, B. A.: 2004, *ApJ* **600**, L35

Moffat, A. F. J.: 1969, *A&A* **3**, 455

Moran, E. C., Kay, L. E., Davis, M., Filippenko, A. V., and Barth, A. J.: 2001, *ApJ* **556**, L75

M^{c}Hardy, I. M., Koerding, E., Knigge, C., Uttley, P., and Fender, R. P.: 2006, *Nature* **444**, 730

M^{c}Hardy, I. M., Papadakis, I. E., and Uttley, P.: 1998, in L. Scarsi, H. Bradt, P. Giommi, & F. Fiore (ed.), *The Active X-ray Sky: Results from BeppoSAX and RXTE*, pp 509–+

M^{c}Hardy, I. M., Papadakis, I. E., Uttley, P., Page, M. J., and Mason, K. O.: 2004, *MNRAS* **348**, 783

Nandra, K.: 2001, in B. M. Peterson, R. W. Pogge, and R. S. Polidan (eds.), *Probing the Physics of Active Galactic Nuclei*, Vol. 224 of *ASP Conference Series*, p. 167

Nandra, K., Clavel, J., Edelson, R. A., George, I. M., Malkan, M. A., Mushotzky, R. F., Peterson, B. M., and Turner, T. J.: 1998, *ApJ* **505**, 594

Nandra, K., Le, T., George, I. M., Edelson, R. A., Mushotzky, R. F., Peterson, B. M., and Turner, T. J.: 2000, *ApJ* **544**, 734

Nandra, K., O'Neill, P. M., George, I. M., and Reeves, J. N.: 2007, *MNRAS* **382**, 194

Narayan, R. and Yi, I.: 1995, *ApJ* **452**, 710

Nenkova, M., Sirocky, M. M., Ivezić, Ž., and Elitzur, M.: 2008a, *ApJ* **685**, 147

Nenkova, M., Sirocky, M. M., Nikutta, R., Ivezić, Ž., and Elitzur, M.: 2008b, *ApJ* **685**, 160

Nowak, M.: 2005, *Ap&SS* **300**, 159

O'Brien, P. T. and Leighly, K. M.: 1998, *Advances in Space Research* **21**, 67

Ogle, P. M., Mason, K. O., Page, M. J., Salvi, N. J., Cordova, F. A., M^{c}Hardy, I. M., and Priedhorsky, W. C.: 2004, *ApJ* **606**, 151

Oknyanskij, V. L. and Horne, K.: 2001, in B. M. Peterson, R. W. Pogge, and R. S. Polidan (eds.), *Probing the Physics of Active Galactic Nuclei*, Vol. 224 of *ASP Conference Series*, p. 149

Oknyanskij, V. L., Horne, K., Lyuty, V. M., Sadakane, K., Honda, S., and Tanabe, S.: 2003, in S. Collin, F. Combes, and I. Shlosman (eds.), *Active Galactic Nuclei: From Central Engine to Host Galaxy*, Vol. 290 of *ASP Conference Series*, p. 119

Osterbrock, D. E. and Parker, R. A. R.: 1965, *ApJ* **141**, 892

Papadakis, I. E., Petrucci, P. O., Maraschi, L., M^{c}Hardy, I. M., Uttley, P., and Haardt, F.: 2002, *ApJ* **573**, 92

Peng, C. Y., Ho, L. C., Impey, C. D., and Rix, H.-W.: 2002, *AJ* **124**, 266

Peterson, B. M., M^{c}Hardy, I. M., Wilkes, B. J., Berlind, P., Bertram, R., Calkins, M., Collier, S. J., Huchra, J. P., Mathur, S., Papadakis, I., Peters, J., Pogge, R. W., Romano, P., Tokarz, S., Uttley, P., Vestergaard, M., and Wagner, R. M.: 2000, *ApJ* **542**, 161

Peterson, B. M.: 1997, *An Introduction to Active Galactic Nuclei*, Cambridge University Press, New York, ISBN 0521473489

Peterson, B. M.: 1999, in C. M. Gaskell, W. N. Brandt, M. Dietrich, D. Dultzin-Hacyan, and M. Eracleous (eds.), *Structure and Kinematics of Quasar Broad Line Regions*, Vol. 175 of *ASP Conference Series*, p. 49

Peterson, B. M.: 2001, in I. Aretxaga, D. Kunth, and R. Mújica (eds.), *Advanced Lectures on the Starburst-AGN*, p. 3

Peterson, B. M.: 2006, in D. Alloin (ed.), *Physics of Active Galactic Nuclei at all Scales*, Vol. 693 of *Lecture Notes in Physics, Berlin Springer Verlag*, p. 77

Peterson, B. M., Ferrarese, L., Gilbert, K. M., Kaspi, S., Malkan, M. A., Maoz, D., Merritt, D., Netzer, H., Onken, C. A., Pogge, R. W., Vestergaard, M., and Wandel, A.: 2004, *ApJ* **613**, 682

Peterson, B. M. and Wandel, A.: 2000, *ApJ* **540**, L13

Peterson, B. M., Wanders, I., Bertram, R., Hunley, J. F., Pogge, R. W., and Wagner, R. M.: 1998a, *ApJ* **501**, 82

Peterson, B. M., Wanders, I., Horne, K., Collier, S., Alexander, T., Kaspi, S., and Maoz, D.: 1998b, *PASP* **110**, 660

Petrucci, P. O., Haardt, F., Maraschi, L., Grandi, P., Matt, G., Nicastro, F., Piro, L., Perola, G. C., and De Rosa, A.: 2000, *ApJ* **540**, 131

Petrucci, P. O., Maraschi, L., Haardt, F., and Nandra, K.: 2004, *A&A* **413**, 477

Press, W. H.: 2002, *Numerical recipes in C++ : the art of scientific computing*, Cambridge University Press

Robson, I.: 1996, *Active galactic nuclei*, NY: Wiley, Chichester: Praxis Publishing

Salvati, M., Hunt, L. K., Calamai, G., Del Zanna, G., Giannuzzo, E., Kidger, M., Mannucci, F., Stanga, R. M., and Wamsteker, W.: 1993, *A&A* **274**, 174

Santos, J. F. C. J., Alloin, D., Bica, E., and Bonatto, C.: 2002, in D. P. Geisler, E. K. Grebel, and D. Minniti (eds.), *Extragalactic Star Clusters*, Vol. 207 of *IAU Symposium*, p. 1

Schmidt, M.: 1963, *Nature* **197**, 1040

Sergeev, S. G., Doroshenko, V. T., Golubinskiy, Y. V., Merkulova, N. I., and Sergeeva, E. A.: 2005, *ApJ* **622**, 129

Seyfert, C. K.: 1943, *ApJ* **97**, 28

Shakura, N. I. and Sunyaev, R. A.: 1973, *A&A* **24**, 337

Shemmer, O., Uttley, P., Netzer, H., and M^{c}Hardy, I. M.: 2003, *MNRAS* **343**, 1341

Smith, H. J. and Hoffleit, D.: 1963, *AJ* **68**, 292

Smith, J. E., Robinson, A., Alexander, D. M., Young, S., Axon, D. J., and Corbett, E. A.: 2004, *MNRAS* **350**, 140

Smith, J. E., Young, S., Robinson, A., Corbett, E. A., Giannuzzo, M. E., Axon, D. J., and Hough, J. H.: 2002, *MNRAS* **335**, 773

Smith, R. and Vaughan, S.: 2007, *MNRAS* **375**, 1479

Sobolewska, M. A. and Papadakis, I. E.: 2009, *MNRAS* **399**, 1597

Steele, I. A., Smith, R. J., Rees, P. C., Baker, I. P., Bates, S., Bode, M., and et al.: 2004, *Ground-based Telescopes. Edited by Oschmann, Jacobus M., Jr. Proceedings of the SPIE* **5489**, 679

Suganuma, M., Yoshii, Y., Kobayashi, Y., Minezaki, T., Enya, K., Tomita, H., Aoki, T., Koshida, S., and Peterson, B. A.: 2006, *ApJ* **639**, 46

Summons, D.: 2008, *Ph.D. Thesis, University of Southampton*

Sunyaev, R. A. and Titarchuk, L. G.: 1980, *A&A* **86**, 121

Tanaka, Y., Nandra, K., Fabian, A. C., Inoue, H., Otani, C., Dotani, T., Hayashida, K., Iwasawa, K., Kii, T., Kunieda, H., Makino, F., and Matsuoka, M.: 1995, *Nature* **375**, 659

Taylor, R. D., Uttley, P., and McHardy, I. M.: 2003, *MNRAS* **342**, L31

Timmer, J. and Koenig, M.: 1995, *A&A* **300**, 707

Tomita, H., Yoshii, Y., Kobayashi, Y., Minezaki, T., Enya, K., Suganuma, M., Aoki, T., Koshida, S., and Yamauchi, M.: 2006, *ApJ* **652**, L13

Urry, C. M. and Padovani, P.: 1995, *PASP* **107**, 803

Uttley, P. and M^{c}Hardy, I. M.: 2001, *MNRAS* **323**, L26

Uttley, P., M^{c}Hardy, I. M., and Papadakis, I. E.: 2002, *MNRAS* **332**, 231

Uttley, P., M^{c}Hardy, I. M., Papadakis, I. E., Cagnoni, I., and Fruscione, A.: 2000, *MNRAS* **312**, 880

Uttley, P.: 2006, in C. M. Gaskell, I. M. M^{c}Hardy, B. M. Peterson, and S. G. Sergeev (eds.), *ASP Conference Series*, Vol. 360, p. 101

Uttley, P., Edelson, R., M^{c}Hardy, I. M., Peterson, B. M., and Markowitz, A.: 2003, *ApJ* **584**, L53

van der Klis, M.: 1989, in H. Ögelman and E. P. J. van den Heuvel (eds.), *Timing Neutron Stars*, p. 27

van der Klis, M.: 1994, *ApJS* **92**, 511

Vanden Berk, D. E., Richards, G. T., Bauer, A., Strauss, M. A., Schneider, D. P., Heckman, T. M., York, D. G., Hall, P. B., Fan, X., Knapp, G. R., and 52 co-authors: 2001, *AJ* **122**, 549

Vaughan, S., Edelson, R., Warwick, R. S., and Uttley, P.: 2003, *MNRAS* **345**, 1271

Wanders, I., Peterson, B. M., Alloin, D., Ayres, T. R., Clavel, J., Crenshaw, D. M., Horne, K., Kriss, G. A., and Krolik, J. H.: 1997, *ApJS* **113**, 69

Webb, W. and Malkan, M.: 2000, *ApJ* **540**, 652

Welsh, W. F.: 1999, *PASP* **111**, 1347

White, R. J. and Peterson, B. M.: 1994, *PASP* **106**, 879

Wickramasinghe, N. C., Lukes, T., and Dempsey, M. J.: 1974, *Ap&SS* **30**, 315

Wilson, A. S. and Colbert, E. J. M.: 1995, *ApJ* **438**, 62

Woo, J.-H. and Urry, C. M.: 2002, *ApJ* **579**, 530

Woźniak, P. R., Alard, C., Udalski, A., Szymański, M., Kubiak, M., Pietrzyński, G., and Zebruń, K.: 2000, *ApJ* **529**, 88

Yang, F., Hu, C., Chen, Y., and Wang, J.: 2007, *Chinese Journal of Astronomy and Astrophysics* **7**, 353

Yoshii, Y., Kobayashi, Y., and Minezaki, T.: 2003, in *Bulletin of the American Astronomical Society*, Vol. 35, p. 752

Zdziarski, A. A., Lubiński, P., Gilfanov, M., and Revnivtsev, M.: 2003, *MNRAS* **342**, 355

Zhang, Y. H., Cagnoni, I., Treves, A., Celotti, A., and Maraschi, L.: 2004, *ApJ* **605**, 98